Photoelectron spectra of the one-electron atomic system in the stabilization regime by the Siegert state expansion method

by

Koudai Toyota

Submitted in Partial Fulfillment of

the Requirements for the Degree of

Doctor of Philosophy

at

The University of Electro-Communications

MARCH 2010

Photoelectron spectra of the one-electron atomic system in the stabilization regime by the Siegert state expansion method

APPROVED BY SUPERVISORY COMMITTEE:

CHAIRPERSON: Prof. Shinichi Watanabe

MEMBER: Prof. Kozo Hakuta

MEMBER: Prof. Mitsuo Takeda

MEMBER: Prof. Yasushi Ohfuti

MEMBER: Prof. Nobuyuki Nakamura

MEMBER: Prof. Hiroki Saito

This thesis was also reviewed by

Prof. Oleg I. Tolstikhin at Russian Research Center "Kurchatov Institute", Russia

Prof. Robin Santra at Argonne National Laboratory, USA

Prof. Joachim Burgdörfer at Vienna University of Technology, Austria

Prof. Kiyohiko Someda at Tokyo University, Japan

Prof. Chii-Dong Lin at Kansas State University, USA

論文の和文概要

論文題目	Photoelectron spectra of the one-electron atomic system in the stabilization regime by the Siegert state expansion method
氏　　名	豊田　広大

本論文ではstabilization領域における一電子原子系の光電子スペクトルをSiegert状態展開法を用いて高精度に計算し、結果を考察した。stabilizationとは、光子エネルギーが電子の結合エネルギーよりも十分高い“高周波レーザー”中において、レーザー強度がある閾値を超えるとイオン化レートが減る現象である。本論文では二種類の新奇な物理現象を見出した。(i) 多光子吸収ピーク中に振動構造が現れた。高周波Floquet理論[1]による解析によって、これが光電子波束対の干渉縞であることを示した[2]。また、干渉縞の形成にはstabilizationが重要な役割を果たすことを明らかにした。(ii)超低速電子を示すピークが現れた。その生成メカニズムは多光子吸収、トンネル効果といったよく知られたイオン化メカニズムでは説明できない。本論文ではその起源が、電子の有効ポテンシャルが時間の関数としてゆっくり変形している状況下における非断熱遷移であることを示した[3]。

[1] M. Gavrila and J. Z. Kaminski, Phys. Rev. Lett. **52**, 613 (1984).
[2] K. Toyota, O. I. Tolstikhin, T. Morishita, and S. Watanabe, Phys. Rev. A **76**. 043418 (2007), Phys. Rev. A **78**, 033432 (2008).
[3] K. Toyota, O. I. Tolstikhin, T. Morishita, and S. Watanabe Phys. Rev. Lett. **103**, 153003 (2009).

論 文 の 英 文 要 旨

TITLE	Photoelectron spectra of the one-electron atomic system in the stabilization regime by the Siegert state expansion method
NAME	Koudai Toyota

This thesis studies the photoelectron spectrum of the one-electron atomic system in the stabilization regime by the Siegert state expansion method.

When a high-frequency laser pulse is applied to an atom, the ionization rate decreases as the intensity exceeds a certain critical value. This is called the stabilization [1]. The term *high-frequency* here means that the photon energy of the laser is much higher than the binding energy of the electron. In the stabilization regime, the suppression of the ionization rate has been the main subject. This is, of course, important, but describing only one aspect of the dynamics. To obtain deeper insight of the dynamics in the stabilization regime, it is indispensable to consider the photoelectron spectra. To this end, we developed the Siegert state (SS) expansion method in the Kramers-Henneberger (KH) frame. In the KH frame, the effect of the laser field is correctly brought into the time-dependent Schrödinger equation. Unphysical reflections from the boundary of the box can be removed by the Siegert state method. Thus the combination of these two methods enable us to obtain accurate photoelectron spectra. The main objective of this thesis is to clarify the general features of the ionization dynamics in the stabilization regime via the analysis of the photoelectron spectra.

This thesis is thus constructed as follows. Chapter 1 introduces the stabilization regime and its historical developments. Chapter 2 studies the atomic stabilization which plays a key role when we analyze the photoelectron spectrum in Chapters 5 and 6. Chapter 3 summarizes some properties of the Siegert states (SSs) required to implement the SS expansion of a wave packet. In Chapter 4, the SS expansion in the KH frame is formulated. In Chapters 5 and 6, photoelectron spectra of the negative ion in the stabilization regime are analyzed as an example. Chapter 5 analyzes oscillating substructures in multiphoton absorption peaks [2]. The analysis in terms of the high-frequency Floquet theory [3] shows that this comes from the interference of a pair of photoelectron wave packets produced at different moments in time, and the stabilization plays a key role. Chapter 6 discusses generation of a low energy electron [4]. Its emergence seems to contradict our intuition since the photon energy is much higher then the binding energy. Its origin cannot be explained by the well-known ionization mechanisms: multiphoton and tunneling processes. We show that this comes from the non-adiabatic transition to the continuum caused by slow deformation of the effective potential of the electron. Chapter 7 concludes the thesis.

[1] M. Pont and M. Gavrila, Phys. Rev. Let. **65**, 2362 (1990).

[2] K. Toyota, O. I. Tolstikhin, T. Morishita, and S. Watanabe, Phys. Rev. A **76**. 043418 (2007), Phys. Rev. A **78**, 033432 (2008).

[3] M. Gavrila and J. Z. Kaminski, Phys. Rev. Lett. **52**, 613 (1984).

[4] K. Toyota, O. I. Tolstikhin, T. Morishita, and S. Watanabe, Phys. Rev. Lett. **103**, 153003 (2009).

Acknowledgements

When you travel to foreign countries, your trip becomes much more fruitful if you are accompanied by knowledgeable local people. When I tripped to Taiwan in September of 2009, I could fully enjoy touring Taiwan despite the shortness of my stay thanks to the great guide provided to me by Prof. Chien-Nan Liu and his students at Fu-Jen Catholic University, and their friends. The local people know local affairs to great depth: transportation systems, exquisite culinary arts, spots of marvelous scenic beauty, and so on. The same seems to apply to the research. Collaborating with other people is the best way to make better achievements despite limited time available. Therefore, I definitely could not have been as successful with my PhD research without the following experts, colleagues, and their supports.

Prof. Shinichi Watanabe at University of Electro-Communications (UEC) has strongly encouraged me with my research since I joined his group in 2001. He always has taken the helm for all people in the laboratory to correctly move all the things forward. I was also really taken into caring hands of him and people around. He introduced to me the Siegert pseudostate (SPS). I consider that his far-seeing wisdom lead me to the rich world of the SPS. Dr. Seiichi Tanabe, a former master's student in my group, frequently visited our laboratory, and helped me in the initial stage of the undergraduate works although he had been already working at private company. However, I could produce almost nothing for one year since I began my research. In these difficult days, my old colleagues Masaki Mutou, Takeshi Sasajima, Masatoshi Hananoe, and Hiroshi Ishimura, were very helpful with discussions on physics and instructions with computers. Masashi Matono readily helped me with keeping touch with UEC when I was working at a private company. Gopi Krishna, Fumiki Muroyama and his delightful colleagues created a relaxed atmosphere in the laboratory. This greatly helped me fit in the laboratory

again after coming back to UEC as a PhD student. I respect Masatoshi Umetsu and Masataka Ohmi for their artisan spirit and passions for the research. Shinnosuke Aizawa and Ayumi Kobayashi taught me pleasures and difficulties of teaching other people. I am very happy in that we still keep in touch.

Prof. Toru Morishita helped me with calculations many times. It was kind of him to allow me to use his computer codes. These programs were exploited for the study of three-body Coulomb systems in my master's course. He also helped me with some calculations for the paper published in 2005. We developed the computer codes independently and solved the same problem in parallel to illustrate our common theory of the SPS, and Prof. Morishita obtained a better convergence with his codes. Therefore we adopted his numerical results. And he encouraged me to visit Prof. Chii-Dong Lin's laboratory at Kansas State University (KSU) once on the Center of Excellence Program (COE) in 2007 and on the JSPS Bilateral joint program between US and Japan in 2008 on another occasion. During that visit Prof. Chii-Dong Lin was kindly giving me chances to show our results in their group meeting. Discussions with highly capable researchers in Prof. Lin's laboratory were very fruitful. Dr. Hiroki Mashiko at Prof. Zenghu Chang's laboratory at KSU gave me precious opportunities to see the experimental group of the highest standard in the world.

Prof. Kozo Hakuta, the core leader of the COE program at UEC, was instrumental in giving me a challenging stage as a COE student. Thanks to the strong and continuous supports from the COE program, I could fully concentrate on the research for four years.

Prof. Oleg I. Tolstikhin took me to the noble world of physics far beyond my talents. I really thank my fortunes for which I could study with him in my PhD research. He has a rich talent for both pedagogy and research. His instruction is always clear and concrete. I could obtain valuable results using his accurate computer codes and theory against my short time available. I feel that I could read just a few pages of his encyclopedic knowledge of physics and mathematics, or I may be likened to a child playing in his vast garden of orderly knowledge.

My work was also supported by research funds. I thank greatly to the 21st century Center Of Excellence program (COE) at UEC, Research fellowships form Japan Society

for the Promotion of Science (JSPS), and JSPS Bilateral joint program between US and Japan.

Contents

Figures

Figure

Chapter 1

Introduction

This thesis studies photoelectron spectra of the one-electron atomic system in the stabilization regime by the Siegert state expansion method. *The stabilization*, first discovered theoretically by Pont *et al.* [1], is a phenomenon in which the ionization rate of an atom decreases for the laser intensity larger than a certain critical value in *a high-frequency laser field*. Here the term "high-frequency" means that the photon energy ω of the laser field is much higher than the binding energy of the electron I_p, *i.e.*,

$$\omega \gg I_p. \tag{1.1}$$

Here and hereafter the atomic units are used so that $\hbar = 1, e = 1, m_e = 1$. This *high-frequency condition* indicates that the optical cycle of the laser field is much faster than the characteristic time scale of the electron motion. Then the rapid oscillations of the laser field can be averaged out in time; the electron can be regarded as being bound in the time-averaged static potential well. The stabilization can be understood with the help of the excursion amplitude α of a fictitious free-electron in the laser field; For monochromatic laser fields, α is given by $\alpha = F/\omega^2$, where F is the amplitude of the laser field. In the high-frequency laser field, the electron decouples from the nucleus for the excursion amplitude larger than a certain critical value α_c, *i.e.*

$$\alpha = F/\omega^2 > \alpha_c. \tag{1.2}$$

Then the photon absorption is suppressed, and the stabilization emerges. Thus, the stabilization regime can be defined by the parameter space formed by the laser frequency ω and field amplitude F satisfying the conditions Eq. (1.1) and (1.2). In this thesis, let us call the laser field satisfying the condition Eq. (1.2), *a high-intensity laser field*; if the

laser field satisfies both the conditions Eq. (1.1) and (1.2), let us call it *a high-frequency and high-intensity laser field*. In this thesis, we treat theoretically a few noteworthy effects caused by the stabilization. The stabilization is intensively studied by many researchers; see, for example, [2, 3] and also review articles [4, 5]. In these theoretical calculations, the typical laser parameters considered are such that the photon energy is about tens of eV and the intensity is $I \approx 10^{16}$ W/cm^2. This parameter regime is still difficult to attain even in the latest laser technologies. However, Vos [6] and Pont [7] pointed out later that the use of the Rydberg Ne atom $(2p)^5$ 5g (m=4) relaxes these difficulties; here m is the magnetic quantum number. Its ionization potential is $I_p = 0.544$ eV, the high-frequency condition Eq. (1.1) can be satisfied using the laser in the visible range. Thus the intensity required for the stabilization Eq. (1.2) is also relaxed. Based on this idea, de Boer *et al.* [8, 9] and van Druten *et al.* [10] implemented an experiment by employing the Rydberg state of Ne atom $(2p)^5$ 5g (m=4) with the laser wave length and intensity 620 nm and $\approx 10^{14}$ W/cm^2, respectively. The Rydberg state is prepared by an pump pulse ultraviolet (UV) laser pump pulse of wave length 286 nm. They observed the stabilization in the sense of decrease in ionization yield as a function of laser intensity. Later, Piraux *et al.* qualitatively reproduced the experimental results, and attributed the decrease in ionization yield to the stabilization [11].

However, as far as we know, studies in this regime, theoretical or experimental, usually concentrate on the ionization rate or total ionization probability (see, *e.g.*, [12]; see also review articles [13, 5] and references therein). Such gross characteristics are important, but describe only one aspect of the dynamics. To gain insight into further details, it is essential to consider the photoelectron spectrum which may bear various signatures of the dynamics not revealed by the total ionization probability alone. However, this is not straightforward. Widely used approach with absorbing boundary conditions in a large box solves the time-dependent Schrödinger equation (TDSE) in the laboratory frame, see e.g. [14, 15, 16, 17]. However, this scheme substantially bears the following problems. First, the laboratory frame modifies the dynamics since the laser field must be eventually cut off beyond the finite box considered in the calculations. Second, the dynamics is disturbed also by the absorbing potential, whose effect is difficult to control and disentangle. Under the circumstances, Reed and Burnett [18] suggested to use the

Kramers-Henneberger (KH) frame [19, 20] instead of the laboratory frame. In the KH frame, the interaction with the laser field is represented by the atomic potential whose center follows the quivering trajectory of a classical electron. Hence it is localized in a finite region of space where the atomic potential is effective. The electron moves freely once it leaves this interaction region. As was demonstrated in [18], this fact enables one to increase (approximately double) the length of a laser pulse that can be treated, because the calculations can be extended up to the moment when the electron returns to the interaction region after its reflection from the boundary of the box. Alternatively, one can reduce (approximately halve) the size of the box. In any case, a gain in the computational efficiency is achieved. The advantage of the KH frame is well recognized [13, 5]. As regards the boundary reflections in [18], zero boundary conditions were used. In this case, the box size must exceed the interaction region to calculate the spectrum substantially, the finiteness of the box obviously limits the high-energy extent of the spectrum obtained as well as its resolution. The gain from the use of the KH frame would be much more essential if one could reduce the size of the box to that of the interaction region. The absorbing boundary conditions may help to reach this goal, but if only the total ionization probability is needed. In this thesis, we present a method in which only the interaction region needs to be considered and, at the same time, which is capable of calculating the spectra up to any desired energy and without any practical limitations.

The idea consists of applying the recently developed Siegert-state expansion approach [21, 22, 24] to solving the TDSE in the KH frame [23]. Siegert states (SSs) are the solutions to the stationary Schrödinger equation satisfying outgoing-wave boundary conditions. The corresponding eigenvalue problem was first considered by Siegert [25] for s-wave scattering in a finite range potential. SSs remained a mere formal object in scattering theory until Tolstikhin *et al.* [26, 27, 28] developed an algebraic formulation known as the theory of Siegert pseudostates (SPSs) which became a powerful tool in practical calculations. Recently, this formulation was supplemented by its application to the SPS perturbation theory [29]. More recently, it has been generalized to nonzero values of the angular momentum [30]. In the stationary framework, SPSs have been employed, for example, for the calculation of resonances in three-body Coulomb systems

[31, 32, 33]. Yoshida *et al.* [34] and Tanabe *et al.* [35] pioneered applications of SPSs as a basis to treat time propagation of wave packets. An advantage of such a basis is that it does not produce unphysical reflections at the boundary of the box because the outgoing-wave boundary conditions are exactly satisfied. Subsequently, Santra *et al.* [36] following an earlier work [37] developed a rigorous formalism of the wave packet expansion in terms of SPSs for the case of a stationary Hamiltonian. Finally, Tolstikhin [21, 22, 23, 24] has extended the method to time-dependent Hamiltonians, which made its applications to many nonstationary problems such as laser-atom interaction possible. The SS expansion approach [21, 22] enables us to solve the TDSE, avoiding unphysical reflections from the boundary of the box. The use of the KH frame guarantees that the interaction with the laser field is fully taken into account so long as the box is large enough to cover the interaction region. When these two elements are combined, the method is free from approximations despite the use of a very restricted box size. But the main advantage of the method is its ability to produce highly resolved accurate spectra.

There are two goals in this thesis. A first goal is developing the Siegert state expansion approach in the Kramers-Henneberger frame to accurately calculate the photoelectron spectrum. The other goal is providing a look at general features of the dynamics of ionization by laser pulses in the stabilization regime via analysis of the photoelectron spectra.

Thus this thesis is organized as follows. In Chapter 2, an overview of the stabilization regime is provided. The most prominent physical phenomenon is the stabilization. We introduce the high-frequency Floquet theory [38] to clarify the dynamics of the stabilization by introducing some important concepts and terminologies. These are indispensable for extracting the ionization dynamics recorded onto the photoelectron spectrum. In Chapter 3, the basic results of the Siegert states both for the 1D [22] and 3D cases [30] are summarized. The aim of this Chapter is to understand how to expand a wave packet in terms of the SSs. This is not trivial since the SSs have nonstandard orthogonality and completeness relations. In Chapter 4, the Siegert state expansion approach in the Kramers-Henneberger frame for both the 1D [39] and 3D [40] cases are summarized. In Chapters 5 and 6, we study two prominent features in the photoelec-

tron spectrum in the stabilization regime for both the 1D and 3D cases. In Chapter 5, we observe that oscillating substructures are formed in the multiphoton peaks at high intensity. We develop an adiabatic version of the high-frequency Floquet theory, which can handle the finiteness of the pulse duration, and they facilitates physical interpretation of the phenomenon. We then show that the oscillating substructures are nothing but interference fringes of the photoelectron wave packets produced at the different moments in time [39, 40]. Interference fringes in photoelectron spectra have been seen in a different context in X-ray range. Interference fringes appear when the field is intense enough to drive Rabi oscillations between a bound and autoionizing state [41]; see also [42, 43, 44]. In Chapter 6, we analyze the slow electron peak. Although the photon energy is much higher than the binding energy, the electron having almost zero energies are produced. This counterintuitive effect cannot be explained by the well-known ionization mechanisms, namely, multiphoton and tunneling processes. Using a recently developed theoretical method by Tolstikhin [24], we clarify that this is due to the nonadiabatic transitions caused by the slowly deforming dressed potential [45]. In Chapters 5 and 6, for the the sake of theoretical convenience and clarity we consider a negative ion for the target system, and employ the high-intensity laser pulse of wavelength in X-ray range. Then on account of the high photon energy, we do not need to consider additional technical difficulties such as preparing the electron in a Rydberg state to satisfy the high-frequency condition Eq. (1.1). However, the coherent light sources in X-ray range are rapidly being developed by the high-harmonic generation [46, 47, 48, 49, 50, 51, 52] and the free-electron laser technologies [53]. These promising light sources have already clarified many unprecedented aspects of the atoms and molecules in both theoretical and experimental studies; see for instance, [41, 54, 55, 56, 57, 58, 59, 60, 61, 62, 63, 64, 65, 66]. Thus in Chapter 7, we conclude the thesis by pointing out some possibilities for experimental observation of the physical effects found in Chapters 5 and 6, and express a belief that experimentalists further develop the high-intensity laser to study the stabilization regime in EUV to X-ray range, and our results are to be verified in future.

Chapter 2

The stabilization regime

2.1 Introduction

This Chapter aims to study the atomic stabilization [67, 1]. This is one of the most striking manifestations of high-frequency and high-intensity phenomena, and plays an essential role in the ionization dynamics in the stabilization regime. For its experimental status, refer to Appendix A.

To obtain an overview of the stabilization, let us consider the one-electron system interacting with a laser field. For brevity, we model the one-electron system by the Eckart potential

$$V(x) = -\frac{15/8}{\cosh^2 x}. \tag{2.1}$$

This potential supports two bound states. The ground and excited state energy levels are $E_0 = -1.125$ and $E_1 = -0.125$, respectively. Let ω be the frequency of the monochromatic laser field such that ω satisfies the high-frequency condition $\omega \gg |E_0|$ in the stabilization regime. The one-photon ionization rate Γ of the ground state is shown by the red line in Fig. 2.1. The procedures for calculating the ionization rate are described in Sec. 2.3. The parameter α represents the maximum amplitude of the classical trajectory given by $\alpha = F/\omega^2$, where F is the field amplitude. Here let us assume that the value of ω being fixed. In this case the ionization rate Γ can be regarded as a function of F. One can see that Γ first increases as F grows, but begins to decrease when F exceeds the critical value at $\alpha \approx 0.8$. This phenomenon is called the stabilization first discovered by Pont *et al.* [67, 1]. However, the function Γ does not decay monotonically despite further increase in F [73, 75].

To understand this counterintuitive phenomenon, let us recall that the stabi-

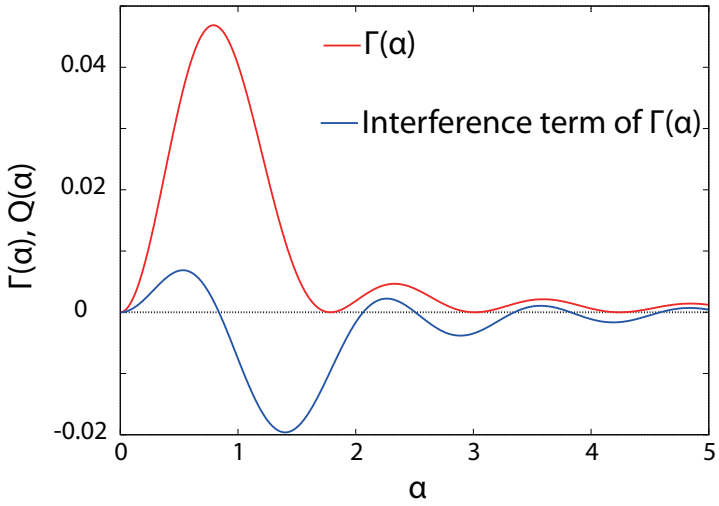

Figure 2.1: One-photon ionization rate $\Gamma(\alpha)$ (red) and its interference term $Q(\alpha)$ (blue) defined by Eq. (2.16) and Eq. (2.17), respectively. The classical electron tends to stay near the turning point $x = \pm\alpha$. Thus two photoelectron wave packets are produced near the left ($x = -\alpha$) and right ($x = \alpha$) turning points. One of them catches the other and interference occurs with the phase difference determined by the distance between two turning points. The function $Q(\alpha)$ is the interference term in the ionization rate $\Gamma(\alpha)$ extracted from this interference picture. The emergence of the stabilization at $\alpha \approx 0.8$ is connected to the destructive interference between the two photoelectron wave packets, *i.e.* $Q(\alpha) < 0$.

lization occurs under the conditions Eq. (1.1) and Eq. (1.2). The condition Eq. (1.2) pertains to the value of α. Thus it is expected that rewriting the time-dependent Schrödinger equation (TDSE) in terms of the classical trajectory facilitates the analyses for extracting the mechanism of the stabilization. This can be implemented by the Kramers-Henneberger (KH) transformation [19, 20]. After this transformation, the classical trajectory is combined into the atomic potential. This transformed potential is called the KH potential. The center of the KH potential quivers along the classical trajectory with the frequency ω. However, under the high-frequency condition Eq. (1.1), the period of the quivering motion of the KH potential is much shorter than the time scale of the electronic motion. Thus the quivering motion of the KH potential can be averaged out with respect to time. The resulting potential is called the dressed potential which is the effective potential of the electron under the high-frequency condition. The

dressed potential is not only a function of the electronic coordinate but also of α. The electron tends to stay near the classical turning points $x = \pm\alpha$ where the velocity of the classical electron is zero. It is thus expected that the two photoelectron wave packets are launched most efficiently from these turning points when photo absorption occurs. One of them catches up with the other, and then interference takes place with the phase difference determined by the distance of the turning points, *i.e.* 2α. When α is small, the interference is constructive since the phase difference is negligible. However, the phase difference increases as α grows, the interference eventually becomes destructive for the value of α satisfying the condition Eq. (1.2). This triggers the decrease of the ionization rate. This is the origin of the stabilization [75].

In what follows, we concentrate on the 1D case for brevity. The extension to the 3D case is straightforward as will beshown in Chapters 5 and 6.

2.2 Kramers-Henneberger frame

First, we introduce the Kramers-Henneberger frame into the TDSE taking the condition Eq. (1.2) into account. The time-dependent Schrödinger equation in the laboratory frame (L) in the length gauge reads,

$$i\frac{\partial\psi_{\rm L}(x_{\rm L},t)}{\partial t} = \left[-\frac{1}{2}\frac{\partial^2}{\partial x_{\rm L}^2} + V(x_{\rm L}) + F(t)x_{\rm L}\right]\psi_{\rm L}(x_{\rm L},t), \tag{2.2}$$

where $V(x_{\rm L})$ and $F(t)$ represent the atomic potential and the laser electric field. Here the atomic potential $V(x_{\rm L})$ has a finite range, hence it can be cut off at $x = x_\pm$, *i.e.*,

$$V(x_{\rm L})|_{x_{\rm L}<x_-} = V(x_{\rm L})|_{x_{\rm L}>x_+} = 0. \tag{2.3}$$

Let $x(t)$ and $v(t) = dx(t)/dt$ be the position and velocity of the classical trajectory of a free electron in the laser field,

$$\frac{d^2x(t)}{dt^2} = -F(t), \tag{2.4a}$$

$$x(t \le 0) = v(t \le 0) = 0, \tag{2.4b}$$

where they satisfy

$$v(t) = -\int_0^t F(t')dt', \quad x(t) = \int_0^t v(t')dt'. \tag{2.5}$$

The KH transformation [19, 20] is defined by

$$x_{\mathrm{L}} = x_{\mathrm{KH}} + x(t), \tag{2.6a}$$

$$\psi_{\mathrm{L}}(x_{\mathrm{L}}, t) = \exp\left[iv(t)x_{\mathrm{L}} - \frac{i}{2}\int_0^t v^2(t')\,dt'\right]\psi_{\mathrm{KH}}(x_{\mathrm{KH}}, t). \tag{2.6b}$$

After the transformation, one obtains the time-dependent Schrödinger equation (TDSE) in the KH frame,

$$i\,\frac{\partial\psi_{\mathrm{KH}}(x_{\mathrm{KH}}, t)}{\partial t} = \left[-\frac{1}{2}\,\frac{\partial^2}{\partial x_{\mathrm{KH}}^2} + V(x_{\mathrm{KH}} + x(t))\right]\psi_{\mathrm{KH}}(x_{\mathrm{KH}}, t). \tag{2.7}$$

In the following, the subscript “KH" is omitted for brevity. The effect of the laser pulse is now combined into the atomic potential $V(x)$ via the classical trajectory $x(t)$. This is the KH potential mentioned in the previous section. The idea of the KH frame is introduced by Kramers [19], and applied to the laser atom interaction in 1968 [20]. In [20], Henneberger pointed out that large discrepancies in the ionization cross section between experiment and theory are due to the fact that the perturbative approach is employed in theory beyond its validity which ignores the strong distortion of the initial state of the atom. So, he considered the KH frame in which the atomic potential and the laser field can be treated on equal footing.

In the KH frame, the effect of the laser field is represented by the quiver motion of the KH potential along the classical trajectory $x(t)$, the amplitude of the oscillation is given by $\alpha = F/\omega^2$ for a monochromatic laser field. Therefore, it is expected that the perturbation theory in the KH frame is valid even with very high intensity if the frequency is high enough. This is actually the case as can be seen when we study the photoelectron spectrum in Chapters 5 and 6, where the typical value of α is several atomic units. This value is smaller than the range of the atomic potential considered there so that the first-order perturbation theory qualitatively reproduces the spectrum.

2.3 High-frequency Floquet theory

The high-frequency aspect of the laser field, Eq. (1.1), is incorporated by the high-frequency Floquet theory (HFFT). For a monochromatic laser field, the KH potential is periodic with respect to time. Hence, it can be expanded into Fourier series,

$$V(x + \alpha\cos\omega t) = \sum_{n=-\infty}^{\infty} V_n(x;\alpha)e^{-in\omega t}, \tag{2.8}$$

where

$$V_n(x;\alpha) = \frac{1}{T}\int_0^T V(x+\alpha\cos\omega t)e^{in\omega t}dt. \tag{2.9}$$

In the stabilization regime, the laser frequency is much higher than the binding energy of the electron *i.e.* $\omega \gg |E_0|$. This means that the period of the laser field is much shorter than the time scale of the electronic motion. Therefore, in the leading order approximation, we only take the $n = 0$ term in Eq. (2.9). Thus the TDSE reduces to

$$[H(\alpha) - E(\alpha)]\phi(x;\alpha) = 0, \tag{2.10a}$$

$$H(\alpha) = -\frac{1}{2}\frac{d^2}{dx^2} + V_0(x;\alpha), \tag{2.10b}$$

where $H(\alpha)$ is the effective Hamiltonian in the stabilization regime. This Hamiltonian is called *the dressed Hamiltonian* since the atomic potential *wears* the laser field in the sense of Eq. (2.9). The important thing is that the time dependency is washed out in the TDSE, and the electron is bound in the static potential. Thus tunneling ionization plays no role. In the stabilization regime, the various high-intensity and high-frequency phenomena including the atomic stabilization can be explained in terms of the dressed potential $V_0(x;\alpha)$. Thus Eqs. (2.10) is the basic equation to extract the physics out of the photoelectron spectrum in Chapters 5 and 6. The dressed Hamiltonian was obtained in [20], and its eigenenergies was analyzed in [71]. The eigenstates supported by the dressed potential $V_0(x;\alpha)$ are called the dressed states. The function $V_n(x;\alpha)$ $(n \neq 0)$ represents the $|n|$-photon decay channels. The one-photon ionization rate $\Gamma(\alpha)$ for the dressed ground state is given by

$$\Gamma(\alpha) = \frac{\Gamma_-(\alpha) + \Gamma_+(\alpha)}{2\pi k(\alpha)}. \tag{2.11}$$

where $\Gamma_\pm(\alpha)$ represents the ionization rate of electron receding from the potential region to the right $(+)$ and left $(-)$ direction, respectively. The function $\Gamma_\pm(\alpha)$ are written as

$$\Gamma_\pm(\alpha) = 2\pi\left|\int_{x_-}^{x_+} \varphi_\pm^*(x, k(\alpha);\alpha)V_1(x;\alpha)\phi_0(x;\alpha)\,dx\right|^2, \tag{2.12}$$

where $\phi_0(x;\alpha)$ represents the dressed ground state with energy $E_0(\alpha)$, and $\varphi_\pm^*(x;k(\alpha);\alpha)$ the scattering state of momenta $k = \sqrt{2(E_0(\alpha)+\omega)}$ of the dressed Hamiltonian Eq. (2.10b). The dressed scattering state is constructed in terms of the Siegert pseudostates, see Eq. (3.20). The behavior of the function $\Gamma(\alpha)$ is shown in Fig. 2.1. Now we are ready

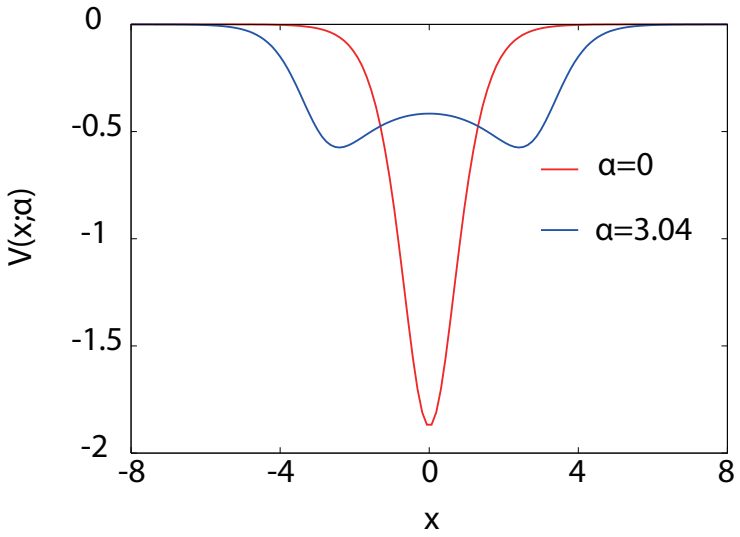

Figure 2.2: The dressed potential, $n = 0$ term in Eq. (2.9), for two different values of α.

to clarify the mechanism of the atomic stabilization, namely the asymptotic decline of the ionization rate $\Gamma(\alpha)$ shown in Fig. 2.1.

2.4 Atomic stabilization

As discussed in the previous section, the dressed potential $V_0(x;\alpha)$ plays the key role in the stabilization regime. So, let us start with visualising $V_0(x;\alpha)$. Fig. 2.2 shows the dressed potential $V_0(x;\alpha)$ for two different values of α. The red line represents the field free atomic potential ($\alpha = 0$); the blue line shows the dressed potential for $\alpha = 3.04$, which is above the critical value of the stabilization $\alpha \approx 0.8$. The velocity of the classical electron is zero at the turning points $x = \pm\alpha$. Therefore, as α grows, the electron spends more time in the outer region of the dressed potential rather than near the core at origin. This emerges as the double-well structure in the dressed potential shown by the blue line in Fig. 2.2. The ground state wave function $\phi_0(x;\alpha)$ for $\alpha = 3.04$ thus has localized amplitudes at the turning points $x = \pm\alpha$, *i.e.*,

$$\phi_0(x;\alpha) = \frac{1}{\sqrt{2}}\left[\phi_{\rm L}(x;\alpha) + \phi_{\rm R}(x;\alpha)\right], \tag{2.13}$$

where the function $\phi_{\rm L}(x;\alpha)$ and $\phi_{\rm R}(x;\alpha)$ have localized amplitude near the left ($x=-\alpha$) and right ($x=\alpha$) turning points, respectively. They can be written by the linear combination of the ground ($\phi_0(x;\alpha)$) and the first excited state wave function ($\phi_1(x;\alpha)$),

$$\phi_{\rm L}(x;\alpha)=\frac{1}{\sqrt{2}}\left[\phi_0(x;\alpha)+\phi_1(x;\alpha)\right],\phi_{\rm R}(x;\alpha)=\frac{1}{\sqrt{2}}\left[\phi_0(x;\alpha)-\phi_1(x;\alpha)\right]. \tag{2.14}$$

From Fig. 2.2, it can be expected that the two photoelectron wave packets are produced from the left and right well for $\alpha=3.04$ when photon absorption takes place. Substituting the expression Eq. (2.13) into Eq. (2.12), the ionization rate $\Gamma_{\pm}(\alpha)$ in Eq. (2.11) can be recast into

$$\Gamma_{\pm}(\alpha)=2\pi\left|\Gamma^{\rm L}_{\pm}(\alpha)+\Gamma^{\rm R}_{\pm}(\alpha)\right|^2, \tag{2.15}$$

Here $\Gamma^{\rm L}_{\pm}(\alpha)$ and $\Gamma^{\rm R}_{\pm}(\alpha)$ are given by

$$\Gamma^{\rm L}_{\pm}(\alpha)=\int_{x_-}^{x_+}\varphi^*_{\pm}(x,k(\alpha);\alpha)V_1(x;\alpha)\frac{1}{\sqrt{2}}\phi_{\rm L}(x;\alpha)dx, \tag{2.16a}$$

$$\Gamma^{\rm R}_{\pm}(\alpha)=\int_{x_-}^{x_+}\varphi^*_{\pm}(x,k(\alpha);\alpha)V_1(x;\alpha)\frac{1}{\sqrt{2}}\phi_{\rm R}(x;\alpha)dx. \tag{2.16b}$$

They represent the transition matrix elements for the electron being ionized from the left (L) and right (R) well, and leaving to the left ($-$) and right ($+$) direction, respectively. After the two photoelectron wave packets are launched, one of them catches up with the other and interference occurs with the phase difference determined by the distance between the two wells, *i.e.*, 2α. Substituting Eq. (2.15) into Eq. (2.11), the interference term in the ionization rate $\Gamma(\alpha)$ can be extracted as

$$Q(\alpha)=\frac{2}{k(\alpha)}\sum_{i=+,-}|\Gamma^{\rm L}_i||\Gamma^{\rm R}_i|{\rm Re}\frac{\Gamma^{\rm R}_i}{\Gamma^{\rm L}_i} \tag{2.17}$$

In Fig. 2.1, the interference term $Q(\alpha)$ is shown by blue line. For the small value of α, the interference is constructive since the phase difference is negligible. However, the phase difference increases as α grows, the picture of the interference turns into destructive when the function $Q(\alpha)$ becomes negative for $\alpha>\alpha_c$. This causes the stabilization [75]. However, the decay of the ionization rate is not monotonic after the stabilization. One can clearly see oscillating structures in Fig. 2.1 since constructive and destructive interference emerges alternately as α grows.

2.5 Theoretical and experimental challenges in the stabilization regime

The suppression of the ionization rate as well as total ionization probability has been the main subject in the stabilization regime both theoretically [67, 1] and experimentally [8, 9, 10]. In the experiments [8, 9, 10], one of the difficulties was placing atoms sufficiently rapidly into a field of high intensity. It may be considered that the ground state depletes before the laser intensity reaches its maximum. To overcome this difficulty, they employed the Rydberg states of Ne atom whose lifetime is of the order of a few hundreds of femtoseconds for high-frequency laser pulses applied to observe the stabilization. Thus the pulse duration of 90 fs was short enough to prevent the depletion of the ground state. Other experimental difficulty is the volume effect of the laser pulse. That is, an ensemble of atoms subjected to an inhomogeneity in intensity due to the spatial distribution of the laser intensity. Thus it may be expected that the volume integration of the experimental results washes out the physical effect of interests. To prevent this, they applied loosely focused laser pulse to atoms. See Appendix A for these discussions.

The suppression of the ionization rate as well as total ionization probability is important but represents only one aspect of the dynamics in this regime. To obtain deeper insights in this regime, it is essential to consider the photoelectron spectrum which may contain various signatures of the dynamics not revealed by the suppression of the total ionization probability or ionization rate. In the next two Chapters, we aim to develop the Siegert state expansion in the Kramers-Henneberger frame which leads us to accurately calculate the photoelectron spectrum.

Chapter 3

Siegert states

3.1 Introduction

This Chapter studies the Siegert states (SSs) [25]. The SSs are the solutions to the stationary Schrödinger equation satisfying the outgoing wave boundary condition. We summarize some basic properties of the SSs which are required to implement the SS expansion of a wave packet in the following Chapters. Before moving into detailed discussions, let us provide an overview on the SS by solving a simple problem.

Let us consider a square well potential,

$$V(x) = \begin{cases} -V_0 & (-a < x < a) \\ 0 & (x < -a, x > a) \end{cases}, \tag{3.1}$$

where V_0 and a represent the depth and width of the potential. The Siegert states (SSs) [25] are defined by the outgoing wave boundary conditions,

$$\left(\frac{d}{dx} \mp ik_n \right) \phi_n(x) \Big|_{x=\pm a} = 0. \tag{3.2}$$

This boundary condition destroys the hermiticity of the Hamiltonian H, the eigenenergies E_n becomes generally complex valued. The wave function in the inner region $-a < x < a$ is,

$$\phi(x) = A \sin \kappa x + B \cos \kappa x, \tag{3.3a}$$

$$\kappa = \sqrt{k^2 + 2V_0}, \tag{3.3b}$$

$$k = \sqrt{2E}. \tag{3.3c}$$

The atomic potential is symmetric with respect to the origin so that the solutions are classified into even or odd parity. The transcendental equation is readily obtained from

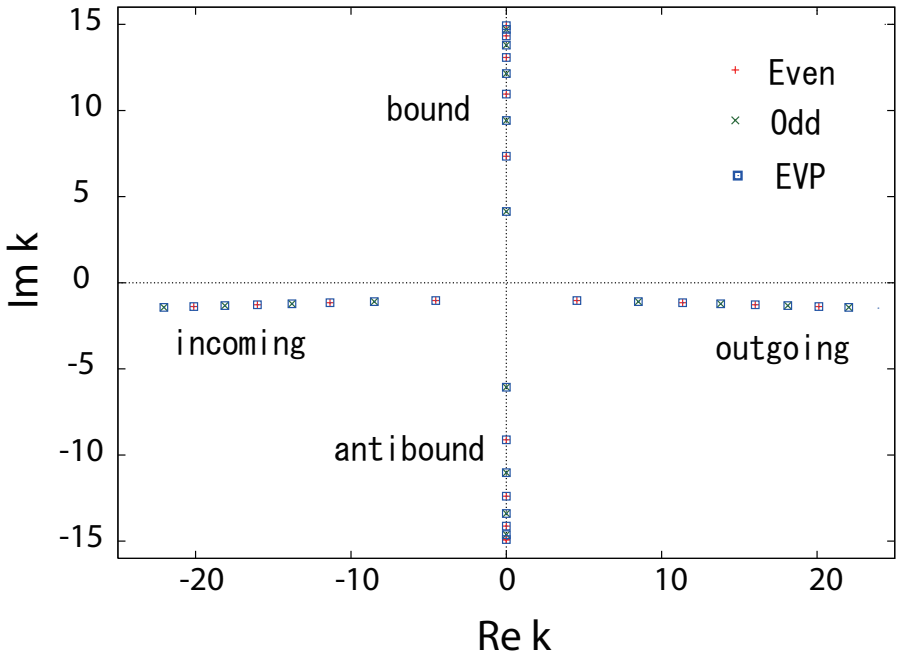

Figure 3.1: Complex energy plane of the Siegert eigenvalue problem for the square well potential Eq. (3.1). In this figure, even and odd parity solutions are indicated by “Even" (red +) and “Odd" (green x), respectively. The eigenvalues are separated into four hierarchies: bound states on positive imaginary axis, antibound states on negative imaginary axis, outgoing states on forth quadrant, and incoming states on third quadrant. In this figure, the solutions “EVP" are obtained from the Siegert pseudostate eigenvalue problem, Eq. (3.28), which is the numerical implementation of the SS.

the matching condition Eq. (3.2),

$$\kappa_n = \frac{n\pi}{2a} - \frac{i}{2a}\log\frac{\kappa_n + k_n}{\kappa_n - k_n} \ (n = 0, 1, 2, \ldots), \tag{3.4}$$

where even (odd) n corresponds to even (odd) parity. For concreteness sake, let us set $V_0 = 112.5$ and $a = 1$, and solve the above equation iteratively. In Fig. 3.1, the eigenvalue distribution obtained from the transcendental equation Eq. (3.4) and the eigenvalue problem Eq. (3.28) are shown. The set of Siegert eigenvalues are split into four classes: bound states (Re $k_n = 0$, Im $k_n > 0$), anti bound states (Re $k_n = 0$, Im $k_n < 0$), outgoing states (Re $k_n > 0$, Im $k_n < 0$), and incoming states (Re $k_n < 0$, Im $k_n < 0$).

There are several important advantages in the SS expansion. First, the SS expansion enables us to remove unphysical reflection which destroys the dynamics when the part of the wave packet returns to the potential region from the boundary

[34, 35, 36, 21, 22, 23]. Second, the scattering state of an arbitrary value of momentum k can be expanded in terms of the SSs [26, 27]. The photoelectron spectrum can be then obtained by projecting the wave function at the end of the pulse onto the scattering state of a certain momentum value k. Thus once dependably evaluated SSs become available, the photoelectron spectrum can be calculated with desired resolutions. However, the SS has some nonstandard properties. First, the eigenvalue problem to be solved turns out to be quadratic with respect to the eigen momentum on account of the outgoing wave boundary condition (see Eq. (3.11)). So, we need to introduce an ingenious idea proposed by Tolstikhin [26, 27] to recast this into a linear one for practical calculations. Second, the orthogonality and completeness relations are nonstandard; it is not trivial to see how to obtain unique expansion coefficients of the wave packet in terms of the SSs. These are the price for incorporating the outgoing wave boundary condition into the Schrödinger equation. Nonetheless, there are more advantages for exploiting from the SSs by overcoming the difficulties.

In this chapter, the theory of the SS are summarized for the whole axis problem in the 1D case [22] and 3D case [30] with non-zero values of the angular momentum. The SSs are numerically implemented by the Siegert pseudostates (SPSs) first proposed by Tolstikhin *et al.* [26, 27], which is the finite basis representation of the SSs.

The historical developments of the SSs are summarized in Appendix B.

3.2 One dimensional case

3.2.1 Siegert states for the whole axis problem

The stationary Schrödinger equation for the whole axis problem in the one dimensional case reads,

$$(H - E)\phi_n(x) = 0, \tag{3.5}$$

where the atomic Hamiltonian H is

$$H = -\frac{1}{2}\frac{d^2}{dx^2} + V(x). \tag{3.6}$$

It is assumed that the atomic potential $V(x)$ has a finite range,

$$V(x)|_{x<x_-} = V(x)|_{x>x_+} = 0. \tag{3.7}$$

The outgoing wave boundary conditions are

$$\left(\frac{d}{dx} \mp ik_n\right)\phi_n(x)\Big|_{x=x_\pm} = 0. \tag{3.8}$$

Let us introduce the operators

$$\mathcal{F}(x;x_0) = \delta(x-x_0),\ \mathcal{D}(x;x_0) = \delta(x-x_0)\frac{d}{dx}. \tag{3.9}$$

Using the operator $D(x;x_0)$, the hermitized Hamiltonian is defined by

$$\tilde{H} = H + \frac{1}{2}\left[\mathcal{D}(x;x_+) - \mathcal{D}(x;x_-)\right]. \tag{3.10}$$

Then Siegert eigenvalue problem, Eq. (3.5) and (3.8), becomes

$$\left(\tilde{H} - \frac{ik}{2}\mathcal{F} - \frac{k^2}{2}\right)\phi(x) = 0, \tag{3.11}$$

where

$$\mathcal{F} = \mathcal{F}(x;x_-) + \mathcal{F}(x;x_+). \tag{3.12}$$

This quadratic eigenvalue problem with respect to k can be converted into a linear one [26, 27] by introducing a new vector

$$\begin{pmatrix} \phi_n(x) \\ \tilde{\phi}_n(x) \end{pmatrix}, \tag{3.13}$$

where

$$\tilde{\phi}(x) = ik\phi(x). \tag{3.14}$$

Then one obtains,

$$\left[\begin{pmatrix} 0 & 1 \\ -2\tilde{H} & \mathcal{F} \end{pmatrix} - ik_n\right]\begin{pmatrix} \phi_n(x) \\ \tilde{\phi}_n(x) \end{pmatrix} = 0. \tag{3.15}$$

Multiplying the matrix

$$\begin{pmatrix} -\mathcal{F} & 1 \\ 1 & 0 \end{pmatrix} \tag{3.16}$$

from the left side, we have a symmetrized form,

$$\left[\begin{pmatrix} -2\tilde{H} & 0 \\ 0 & 1 \end{pmatrix} - ik_n\begin{pmatrix} -\mathcal{F} & 1 \\ 1 & 0 \end{pmatrix}\right]\begin{pmatrix} \phi_n(x) \\ \tilde{\phi}_n(x) \end{pmatrix} = 0. \tag{3.17}$$

Therefore the eigenvector $(\phi_n(x)\ \tilde{\phi}_n(x))^T$ is subject to the orthonormal relationship

$$\int_{x_-}^{x_+} \left(\phi_n(x)\ \tilde{\phi}_n(x)\right) \begin{pmatrix} -\mathcal{F} & 1 \\ 1 & 0 \end{pmatrix} \begin{pmatrix} \phi_m(x) \\ \tilde{\phi}_m(x) \end{pmatrix} dx = 2ik_n\delta_{nm}. \tag{3.18}$$

This is equivalent to

$$\int_{x_-}^{x_+} \phi_n(x)\phi_m(x)dx + i\frac{\phi_n(x_-)\phi_m(x_-) + \phi_n(x_+)\phi_m(x_+)}{k_n + k_m} = \delta_{nm}. \tag{3.19}$$

The SS expansion of the scattering state for the momentum k is given by,

$$\varphi_{\pm}^{\text{in}}(x,k) = ike^{\mp ikx_\pm} \sum_n \frac{\phi_n(x)\phi_n(x_\pm)}{k_n(k-k_n)},\ x_- \le x \le x_+. \tag{3.20}$$

The wave packet formed by the superposition of $\varphi(x,k)$ for a narrow interval of k represents the *in* state, which it approaches the interaction region $x_- < x < x_+$ in the remote past from the left and right, respectively. See Appendix D.1.1 for its derivation and details. The completeness of the set of the eigenvectors $(\phi_n(r)\tilde{\phi}_n(r))^T$ is given by

$$\sum_n \frac{1}{2ik_n} \begin{pmatrix} \phi_n(x) \\ \tilde{\phi}_n(x) \end{pmatrix} (\phi_n(x)\ \tilde{\phi}_n(x)) = \delta(x-x') \begin{pmatrix} 0 & 1 \\ 1 & \mathcal{F} \end{pmatrix}. \tag{3.21}$$

Comparing both sides of the above equation, we find,

$$\sum_n \frac{1}{k_n}\phi_n(x)\phi_n(x') = 0, \tag{3.22a}$$

$$\sum_n \phi_n(x)\phi_n(x') = 2\delta(x-x'), \tag{3.22b}$$

$$\sum_n ik_n\phi_n(x)\phi_n(x') = 2\delta(x-x')\left[\delta(x'-x_-) + \delta(x-x_+)\right]. \tag{3.22c}$$

The SSs form an overcomplete set in the original Hilbert space $\mathbb{H}$, Eq. (3.22b), while the vectors in $\mathbb{H}^2 = \mathbb{H}\otimes\mathbb{H}$, *i.e.* Eq. (3.13), satisfy the normal completeness relationships Eq. (3.21).

3.2.2 Siegert state expansion of an arbitrary function

For a given function $\psi(x) \in \mathbb{H}$, it is important to consider how to expand it in terms of SSs. To uniquely define the expansion coefficients, we introduce a new component $\tilde{\psi}(x)$, and consider a vector $(\psi(x)\ \tilde{\psi}(x))^T$ of $\mathbb{H}^2$. This vector is expanded in terms of SSs,

$$\begin{pmatrix} \psi(x) \\ \tilde{\psi}(x) \end{pmatrix} = \sum_n a_n \begin{pmatrix} \phi_n(x) \\ \tilde{\phi}_n(x) \end{pmatrix}. \tag{3.23}$$

Using the orthogonal relationship Eq. (3.18), we obtain the expansion coefficients

$$a_n = \frac{1}{2ik_n}\left[ik_n\int_{x_-}^{x_+}\phi_n(x)\psi(x)dx - \phi_n(x_-)\psi(x_-) - \phi_n(x_+)\psi(x_+) + \int_{x_-}^{x_+}\phi_n(x)\tilde{\psi}(x)dx\right]. \tag{3.24}$$

Substituting this expression into Eq. (3.23) and using Eq. (3.22a), (3.22b) and (3.22c), the function $\psi(x)$ is reconstructed.

Thus we adopt the set of vectors Eq. (3.13) for expanding a wave packet.

3.2.3 Numerical implementation: Siegert pseudostates for the whole axis problem

In the numerical calculations, the SS formulation mentioned above is implemented in terms of the Siegert pseudostates (SPSs) [26, 27], which is the finite basis representation of the SSs. Let $\{\pi_i(x)\}$ be a complete orthonormal basis set

$$\int_{x_-}^{x_+}\pi_i(x)\pi_j(x)dx = \delta_{ij}, \tag{3.25}$$

$$\sum_{n}^{\infty}\pi_n(x)\pi_n(x') = \delta(x-x'). \tag{3.26}$$

Substituting the finite basis expansion of a wave function

$$\phi_n(x) = \sum_{i=1}^{N} c_i^{(n)}\pi_i(x) \tag{3.27}$$

into Eq. (3.5), and using the boundary condition Eq. (3.8), we obtain

$$\left[\begin{pmatrix} \mathbf{0} & \mathbf{I} \\ -2\tilde{\mathbf{H}} & \mathbf{F} \end{pmatrix} - ik_n\right]\begin{pmatrix} \mathbf{c}^{(n)} \\ \tilde{\mathbf{c}}^{(n)} \end{pmatrix} = 0, \tag{3.28}$$

where

$$\begin{aligned}\tilde{H}_{ij} &= \int_{x_-}^{x_+}\pi_i(x)\tilde{H}\pi_j(x)dx \\ &= \frac{1}{2}\int_{x_-}^{x_+}\frac{d\pi_i(x)}{dx}\frac{d\pi_j(x)}{dx}dx + \int_{x_-}^{x_+}\pi_i(x)V(x)\pi_j(x)dx, \end{aligned}\tag{3.29}$$

$$F_{ij} = \int_{x_-}^{x_+}\pi_i(x)\mathcal{F}\pi_j(x)dx = \pi_i(x_-)\pi_j(x_-) + \pi_i(x_+)\pi_j(x_+). \tag{3.30}$$

The set of $2N$ solutions for the above equation are called Siegert pseudostates (SPSs) which is a finite basis representation of a SSs. In the SPS formulation, the summation runs over all the SPSs. For instance, the summation in Eq. (3.20) and Eq. (3.23) runs over $2N$ SPSs, although some of them might give a false impression of being numerically useless. Let us note that even removing just one of them leads to the wrong result.

3.3 Three dimensional case

3.3.1 Siegert states for the non-zero value of the angular momentum

The theory of the SS can be further extended to the three-dimensional (3D) case. The 3D Siegert eigenvalue problem with nonzero value of the angular momentum is defined by

$$(H_l - E)\phi(r) = 0, \tag{3.31a}$$

$$H_l = -\frac{1}{2}\frac{d^2}{dr^2} + \frac{l(l+1)}{2r^2} + V(r), \tag{3.31b}$$

$$V(r)|_{r\geq a} = 0, \tag{3.31c}$$

$$\phi(0) = 0, \tag{3.31d}$$

$$\left(\frac{d}{dr} - ik + \frac{1}{a}\sum_{p=1}^{l}\frac{z_{lp}}{ika + z_{lp}}\right)\phi(r)\bigg|_{r=a} = 0. \tag{3.31e}$$

Here, a is the cut-off radius for the atomic potential $V(r)$ and z_{lp} $(p = 1, \ldots, l)$ are the zeros of the reverse Bessel polynomial [77]. The additional term in the outgoing wave boundary condition stems from the centrifugal potential. See Appendix C for the outgoing wave boundary condition in the 3D case. Solutions are denoted by k_{ln}, $E_{ln} = k_{ln}^2/2$ and $\phi_{ln}(r)$. Using the operator $\mathcal{D}(r;a)$ introduced by Eq. (3.9), the hermitized Hamiltonian $\tilde{H}_l$ is defined by

$$\tilde{H}_l = H_l + \frac{1}{2}\mathcal{D}(r;a). \tag{3.32}$$

Then the eigenvalue problem Eq. (3.31) becomes

$$\left[\tilde{H}_l - \frac{1}{2}\left(ik - \frac{1}{a}\sum_{p=1}^{l}\frac{z_{lp}}{ika + z_{lp}}\right)\mathcal{F}(r;a) - \frac{1}{2}k^2\right]\phi(r) = 0. \tag{3.33}$$

The eigenvalue problem becomes non-linear with respect to k. Introducing new notations

$$\tilde{\phi}_{ln}(r) = ik_{ln}\phi_{ln}(r), \tag{3.34a}$$

$$\phi_{lnp} = -\frac{z_{lp}}{ik_{ln}a + z_{lp}}\phi_{ln}(a) \ (p = 1, \ldots, l), \tag{3.34b}$$

let us define the new augmented vector

$$\boldsymbol{\phi}_{ln}(r) = \begin{pmatrix} \phi_{ln}(r) \\ \tilde{\phi}_{ln}(r) \\ \phi_{ln1} \\ \vdots \\ \phi_{lnl} \end{pmatrix}. \tag{3.35}$$

Then the eigenvalue problem becomes,

$$[\Lambda_l - ik_{ln}]\boldsymbol{\phi}_{ln}(r) = 0, \tag{3.36}$$

where

$$\Lambda_l = \begin{pmatrix} 0 & 1 & 0 & 0 & \cdots & 0 \\ -2\tilde{H}_l & \mathcal{F}(r;a) & \mathcal{F}(r;a)/a & \mathcal{F}(r;a)/a & \cdots & \mathcal{F}(r;a)/a \\ -z_{l1}\mathcal{F}^T(r;a)/a & 0 & -z_{l1}/a & 0 & \cdots & 0 \\ -z_{l2}\mathcal{F}^T(r;a)/a & 0 & 0 & -z_{l2}/a & \cdots & 0 \\ \vdots & \vdots & \vdots & \vdots & \ddots & \vdots \\ -z_{ll}\mathcal{F}^T(r;a)/a & 0 & 0 & 0 & \cdots & -z_{ll}/a \end{pmatrix}. \tag{3.37}$$

The operator $\mathcal{F}^T(r;a)$ acts on an arbitrary function $u(r)$ according to

$$\mathcal{F}^T(r;a)u(r) = u(a). \tag{3.38}$$

Multiplying the weight matrix

$$\boldsymbol{W}_l = \begin{pmatrix} -\mathcal{F}(r;a) & 1 & 0 & \cdots & 0 \\ 1 & 0 & 0 & \cdots & 0 \\ 0 & 0 & & & \\ \vdots & \vdots & \boxed{-1/z_{lp}} & & \\ 0 & 0 & & & \end{pmatrix}, \tag{3.39}$$

from the left side of Eq. (3.36), we obtain the symmetrized form

$$\left[\begin{pmatrix} -2\tilde{H}_l & 0 & \mathcal{F}(r;a)/a & \cdots & \mathcal{F}(r;a)/a \\ 0 & 1 & 0 & \cdots & 0 \\ \mathcal{F}^{\mathcal{T}}(r;a)/a & 0 & & & \\ \mathcal{F}^{\mathcal{T}}(r;a)/a & 0 & & \boxed{1/a} & \\ \vdots & \vdots & & & \\ \mathcal{F}^{\mathcal{T}}(r;a)/a & 0 & & & \end{pmatrix} - ik_{ln}\boldsymbol{W}_l\right] \begin{pmatrix} \phi_{ln}(r) \\ \tilde{\phi}_{ln}(r) \\ \phi_{ln1} \\ \phi_{ln2} \\ \vdots \\ \phi_{lnl} \end{pmatrix} = 0. \tag{3.40}$$

The object $\boxed{z_{lp}}$ and $\boxed{1/a}$ are the diagonal matrix of dimension l whose pth ($p = 1, \ldots, l$) diagonal element is given by z_{lp} and $1/a$, respectively. Therefore the eigenvectors satisfy the orthonormal relationship,

$$\int_0^a \begin{pmatrix} \phi_{ln}(r) & \tilde{\phi}_{ln}(r) & \phi_{ln1} & \phi_{ln2} & \cdots & \phi_{lnl} \end{pmatrix} \boldsymbol{W}_l \begin{pmatrix} \phi_{ln'}(r) \\ \tilde{\phi}_{ln'}(r) \\ \phi_{ln'1} \\ \phi_{ln'2} \\ \vdots \\ \phi_{ln'l} \end{pmatrix} dr = 2ik_{ln}\delta_{nn'}. \quad (3.41)$$

The Siegert state expansion of the scattering state is given by

$$\varphi_l(r,k) = -ike^{-ika}\frac{(-ika)^l}{\theta_l(-ika)}\sum_n \frac{\phi_{ln}(r)\phi_{ln}(a)}{k_{ln}(k_{ln}-k)},\ 0 \le r \le a. \quad (3.42)$$

See Appendix D.2.1 for its derivation.

From the orthonormal relationship Eq. (3.41), SSs satisfy the following completeness relationship

$$\sum_n \frac{1}{2ik_{ln}}\boldsymbol{\phi}_{ln}(r)\boldsymbol{\phi}_{ln}^T(r') = \delta(r-r')\boldsymbol{W}_l^{-1}. \quad (3.43)$$

Comparing both sides of this equation, we obtain

$$\sum_n \phi_{ln}(r)\phi_{ln}(r') = 2\delta(r-r'), \quad (3.44a)$$

$$\sum_n \frac{1}{k_{ln}}\phi_{ln}(r)\phi_{ln}(r') = 0. \quad (3.44b)$$

As discussed in the 1D case, the SSs form an overcomplete set in the original Hilbert space $\mathbb{H}$, while they have the usual completeness in $\mathbb{H}_2^{(l)} = \mathbb{H} \otimes \mathbb{H} \otimes \mathbb{C}^l$. Here $\mathbb{C}^l$ is the vector space formed by the vectors $(\phi_{ln1}, \ldots, \phi_{lnl})$ in Eq. (3.35). To obtain unique expansion coefficients for a given function $\psi(r)$ in terms of the SSs, we consider another auxiliary function $\tilde{\psi}(r)$ and l additional components ψ_p ($p = 1, \ldots, l$), and introduce the vector

$$\begin{pmatrix} \psi(r) \\ \tilde{\psi}(r) \\ \psi_1 \\ \vdots \\ \psi_l \end{pmatrix}. \quad (3.45)$$

This vector can be expanded by the set of vectors Eq. (3.35) with unique expansion coefficients. Thus we employ the set of vectors Eq. (3.35) as basis functions for expanding a wave packet.

3.3.2 Numerical implementation: Siegert pseudostates for the non-zero values of the angular momentum

In numerical calculations, the SSs are implemented by the Siegert pseudostates (SPS), which is the finite basis representation of the SS. Let $\{\pi_i(r)\}$ $i = 1, 2, \ldots$ be a complete orthonormal basis set. Then,

$$\int_0^a \pi_i(r)\pi_j(r) = \delta_{ij}, \tag{3.46a}$$

$$\sum_i^\infty \pi_i(r)\pi_j(r') = \delta(r - r'). \tag{3.46b}$$

Substituting the finite basis representation of the wave function

$$\phi_{ln}(r) = \sum_{i=1}^{N} c_i^{(n)} \pi_i(r) \tag{3.47}$$

into Eq. (3.31a), and using boundary conditions Eq. (3.31d) and (3.31e), we obtain

$$\left[\begin{pmatrix} \boldsymbol{0} & \boldsymbol{I} & \vec{0} & \cdots & \vec{0} \\ -2\tilde{\boldsymbol{H}}_l & \boldsymbol{F} & \boldsymbol{f}/a & \cdots & \boldsymbol{f}/a \\ -z_{l1}\boldsymbol{f}^T/a & \vec{0}^T & & & \\ \vdots & \vdots & & \boxed{-z_{lp}/a} & \\ -z_{ll}\boldsymbol{f}^T/a & \vec{0}^T & & & \end{pmatrix} - ik_{ln} \right] \begin{pmatrix} \boldsymbol{c}^{(n)} \\ \tilde{\boldsymbol{c}}^{(n)} \\ \phi_{ln1} \\ \vdots \\ \phi_{lnl} \end{pmatrix} = 0, \tag{3.48}$$

where

$$\phi_{lnp} = -\frac{z_{lp}\phi_{ln}(a)}{ika + z_{lp}}, \ p = 1, \ldots, l. \tag{3.49}$$

The matrix elements are defined by

$$\begin{aligned} \tilde{H}_{l,ij} &= \int_0^a \pi_i(r)\tilde{H}_l\pi_j(r)dr \\ &= \frac{1}{2}\int_0^a \frac{d\pi_i(r)}{dr}\frac{d\pi_j(r)}{dr}dr + \int_0^a \pi_i(r)\left[\frac{l(l+1)}{2r^2} + V(r)\right]\pi_j(r)dr, \end{aligned} \tag{3.50}$$

and

$$F_{ij} = \int_0^a \pi_i(r)\mathcal{F}(r;a)\pi_j(r)dr = \pi_i(a)\pi_j(a), \tag{3.51a}$$

$$f_i = \pi_i(a). \tag{3.51b}$$

Here $\vec{0}$ denotes the null vector of which all the elements are 0. The dimension of the original Hilbert space is N, but it is extended to $2N+l$ to incorporate the outgoing wave boundary condition into the Schrödinger equation. As discussed in the 1D case, all the solutions participate in the SPS expansion of the physical quantities. For instance, the scattering state Eq. (3.42) involves $2N + l$ SPSs.

In this thesis, we employ the discrete variable representation (DVR) method [70] to solve the SPS eigenvalue problem Eq. (3.28) and Eq. (3.48) for the 1D and 3D case, respectively. The numerical approach for calculating the SPSs are the same as [27], the Legendre polynomials and the associated Gaussian quadrature are employed. The reason for the use of the Legendre polynomial is that the basis functions having the finite amplitude at the boundary are required to implement the outgoing wave boundary condition.

Chapter 4

Siegert state expansion of a wave packet in the Kramers-Henneberger frame: Accurate numerical method to calculate photoelectron spectra

4.1 Introduction

From the theoretical point of view, how to implement the numerical scheme to study a laser-atom interaction is a fundamental issue. Solving the time-dependent Schrödinger equation (TDSE) in the laboratory frame in the length gauge with absorbing boundary conditions in a large box is a widely used approach, see *e.g.* [14, 15, 16, 17]. However, this scheme substantially bears the following problems. First, the laboratory frame in the length gauge modifies the dynamics since the laser field must be eventually cut off beyond a finite box considered in the calculations. Second, the dynamics is disturbed also by the absorbing potential, whose effect is difficult to control and disentangle. Under the circumstances, Reed and Burnett [18] suggested to use the Kramers-Henneberger (KH) frame [19, 20] instead of the laboratory frame. In the KH frame, the interaction with the laser field is represented by a quiver motion of the center of the atomic potential along a trajectory that the *classical* electron would follow. Hence it is localized in a finite region of space so that the dynamics are not modified for the cut-off radius larger than the range of the quivering potential being effective. The electron moves freely once it leaves this interaction region. As was demonstrated in [18], this fact enables one to increase (approximately double) the length of a laser pulse that can be treated, because the calculations can be extended up to the moment when the electron returns to the interaction region after its reflection from the boundary of the box. Alternatively, one can reduce (approximately halve) the size of the box. In any case, a gain in the computational efficiency is achieved. The advantage of the KH frame

is well recognized [13, 5]. In [18], zero boundary conditions were used, that is, the wave function vanishes at the boundary. In this case, to calculate the spectrum the box must contain the entire interaction region substantially, the finiteness of the box obviously limits the high-energy extent of the spectrum obtained as well as its resolution. The gain from the use of the KH frame would be much more essential if one could reduce the size of the box down to that of the interaction region. Imposing absorbing boundary condition may help to reach this goal, but if only the total ionization probability is needed. The branching ratios are the beyond its scope. The true solution lies in correctly incorporating the *outgoing-wave* boundary condition into the time-dependent Schödinger equation, and it can be implemented in terms of the Siegert state of the previous Chapter.

In this chapter, we summarize the formulation of the Siegert state expansion in the KH frame for both the 1D [39] and 3D [23] cases, its application is implemented in the next Chapter to calculate and study photoelectron spectra. Yoshida *et al.* [34] and Tanabe *et al.* [35] pioneered the applications of SPSs as a basis to treat the time propagation of wave packets. Subsequently, Santra *et al.* [36] following an earlier work [37] developed a rigorous formalism of the expansion in terms of SPSs for the case of a stationary Hamiltonian. Finally, Tolstikhin [21, 22] has extended the method to time-dependent Hamiltonians, which made its applications to many nonstationary problems such as the laser-atom interaction possible. It is shown in [21, 22] that The most important task is to rewrite the outgoing wave boundary condition in the time domain to incorporate it into the TDSE. As shown in later, this is implemented by introducing the new operator $\hat{\lambda}_t$, which is proportionate to the square root of the time differentiation or $\sqrt{\frac{\partial}{\partial t}}$ symbolically. Then the TDSE is recast into a new form in terms of $\hat{\lambda}_t$ by doubling the dimension of the Hilbert space originally considered for the TDSE. The wave packet is expended by the SS basis functions, the resulting close coupling equations for the expansion coefficients of the wave packet are of the Volterra equation of the second kind, which is non-local with respect to time. This is the price for incorporating the outgoing wave boundary condition into the TDSE, but the numerical procedure to solve it is well established [78]. The primary goal of this Chapter is to express the photoelectron spectrum in terms of these expansion coefficients in Sec. 4.2.6 and 4.3.6.

4.2 One dimensional case

4.2.1 The Kramers-Henneberger frame

We consider a one-electron system in one dimension interacting with laser pulses. The time-dependent Schrödinger equation in the laboratory frame (L) in the length gauge reads,

$$i\,\frac{\partial\psi_{\rm L}(x_{\rm L},t)}{\partial t} = \left[-\frac{1}{2}\,\frac{\partial^2}{\partial x_{\rm L}^2} + V(x_{\rm L}) + F(t)x_{\rm L}\right]\psi_{\rm L}(x_{\rm L},t). \tag{4.1}$$

In this thesis, we adopt the dipole approximation for describing the interactions between the electron and laser fields. The dipole approximation is expected to be valid in this thesis since the wavelengths of the laser fields being considered are much larger than the size of systems. However, this approximation fails for the wavelength in hard X-ray range when Compton scattering dominates the ionization processes. It is assumed that the atomic potential $V(x)$ vanishes beyond the interval $-X < x_{\rm L} < X$,

$$V(|x_{\rm L}| > X) = 0. \tag{4.2}$$

The laser electric field has a finite duration T,

$$F(t < 0) = F(t > T) = 0. \tag{4.3}$$

Let $x(t)$ and $v(t) = dx(t)/dt$ be classical trajectories of the free electron in the laser field defined by Eqs. (2.4) and (2.5). Using them, we implement the Kramers-Henneberger (KH) transformation defined by Eq. (2.6). Then we obtain the TDSE in the KH frame,

$$i\,\frac{\partial\psi(x,t)}{\partial t} = \left[-\frac{1}{2}\,\frac{\partial^2}{\partial x^2} + V(x + x(t))\right]\psi(x,t). \tag{4.4}$$

Note that the subscript “KH" in Eq. (2.7) is omitted for brevity. The advantage of the KH potential is that it is localized in a finite interval $x_- < x_{\rm KH} < x_+$,

$$x_- = -X + \min[x(t)], \quad x_+ = X + \max[x(t)]. \tag{4.5}$$

Therefore, the effect of the laser field can be fully taken into account once the box size is large enough to cover the range of this oscillation. Let us rewrite Eq. (4.4) as follows,

$$i\frac{\partial\psi(x,t)}{\partial t} = \mathcal{H}(t)\psi(x,t), \tag{4.6}$$

where

$$\mathcal{H}(t) = H + U(x,t). \tag{4.7}$$

Here H and $U(x,t)$ represent the atomic Hamiltonian and laser-atom interaction,

$$H = -\frac{1}{2}\frac{\partial^2}{\partial x^2} + V(x), \tag{4.8}$$

and

$$U(x,t) = V(x + x(t)) - V(x). \tag{4.9}$$

The wave function in the laboratory frame when the pulse is over can be obtained using Eqs. (2.6b). The observables are calculated by projecting this wave function onto the bound and scattering states of the atomic Hamiltonian Eq. (4.8). Thus the observables depend on the classical trajectories. In this thesis, we assume that the classical trajectories satisfy

$$x(T) = v(T) = 0. \tag{4.10}$$

In this case, the wave functions in the laboratory and KH frame coincides for $t > T$, and hence the observables in both frames also coincide. These conditions are not satisfied unless the value of the carrier envelope phase (CEP) is zero. In this case, the photoelectron spectra in both frames do not coincide due to the phase factor in (4.6b). However, the influence of this additional phase factor on photoelectron spectra may be negligible for high-frequency laser pulses being employed in the following chapters; the electron follows the envelope of the pulse in the high-frequency regime.

4.2.2 The Green's function

We rewrite the solution for Eq. (4.6) using the Green's function to discuss the outgoing wave boundary condition in time domain in the next subsection. Let us start with the stationary outgoing Green's function defined by

$$(E - H)G(x, x'; k) = \delta(x - x') \tag{4.11}$$

with the boundary conditions

$$\left(\frac{d}{dx} \pm ik\right) G(x, x'; k)\Big|_{x=x_\mp} = 0. \tag{4.12}$$

The retarded Green's function for the atomic Hamiltonian H is defined by

$$\left(i\frac{\partial}{\partial t} - H\right)\mathcal{G}(x,x';t) = \delta(t)\delta(x-x'), \tag{4.13a}$$

$$\mathcal{G}(x,x';t)\big|_{t<0} = 0. \tag{4.13b}$$

They are related by the Fourier transform,

$$\mathcal{G}(x,x';t) = \int_{-\infty}^{\infty} G(x,x';k)e^{-iEt}\frac{dE}{2\pi}. \tag{4.14}$$

The retarded Green's function for the full-Hamiltonian $\mathcal{H}(t)$ is given by,

$$\left[i\frac{\partial}{\partial t} - \mathcal{H}(t)\right]\mathscr{G}(x,x';t,t') = \delta(t-t')\delta(x-x'), \tag{4.15a}$$

$$\mathscr{G}(x,x';t,t')\big|_{t<t'} = 0. \tag{4.15b}$$

Using Eq. (4.13), we have another form of this function,

$$\mathscr{G}(x,x';t,t') = \mathcal{G}(x,x';t-t') + \int_{-\infty}^{\infty} dt'' \int_{x_-}^{x_+} dx'' \mathcal{G}(x,x'';t-t'')U(x'',t'')\mathscr{G}(x'',x';t'',t'). \tag{4.16}$$

We assume that the initial state of the electron,

$$\psi(x,t)\big|_{t\to-\infty} = e^{-iE_0t}\phi_0(x), \tag{4.17}$$

where E_0 and ϕ_0 represent the ground state of the atomic Hamiltonian,

$$(H - E_0)\phi_0(x) = 0. \tag{4.18}$$

Then the solution for Eq. (4.6) can be written using Eq. (4.13) as follows,

$$\psi(x,t) = e^{-iE_0t}\phi_0(x) + \int_{-\infty}^{\infty} dt' \int_{x_-}^{x_+} dx' \mathcal{G}(x,x';t-t')U(x',t')\psi(x',t'). \tag{4.19}$$

4.2.3 Outgoing wave boundary condition in time domain

Here we work toward expressing the outgoing wave boundary condition in the time domain using the fractional time derivative approach. Let $\mathcal{F}$ and $\mathcal{D}$ be the operators

$$\mathcal{F}(x;x_0) = \delta(x-x_0), \quad \mathcal{D}(x;x_0) = \delta(x-x_0)\frac{d}{dx}. \tag{4.20}$$

We introduce the hermitized Hamiltonian

$$\tilde{\mathcal{H}}(t) = \mathcal{H}(t) + \frac{1}{2}\left[\mathcal{D}(x;x_+) - \mathcal{D}(x;x_-)\right]. \tag{4.21}$$

Let us introduce the operator $\hat{\lambda}_t$ whose action on $f(t)$ is defined in terms of the Fourier transform as follows,

$$f(t) = \int_{-\infty}^{\infty} f(E) e^{-iEt} \frac{dE}{2\pi}, \tag{4.22}$$

and

$$\hat{\lambda}_t f(t) = \int_{-\infty}^{\infty} ikf(E) e^{-iEt} \frac{dE}{2\pi}. \tag{4.23}$$

Then we have the relationship between $\hat{\lambda}_t$ and time-derivative

$$i\frac{\partial}{\partial t} = -\frac{\hat{\lambda}_t{}^2}{2}, \quad -i\hat{\lambda}_t = \sqrt{2i\frac{\partial}{\partial t}}. \tag{4.24}$$

Now let us seek to express the outgoing wave boundary condition in time domain. Using the operators Eq. (4.20), we rewrite the boundary condition Eq. (4.12) as,

$$\mathcal{D}(x; x_-)G(x, x'; k) = -ik\mathcal{F}(x; x_-)G(x, x'; k), \ x' > x_-, \tag{4.25a}$$

$$\mathcal{D}(x; x_+)G(x, x'; k) = +ik\mathcal{F}(x; x_+)G(x, x'; k), \ x' < x_+. \tag{4.25b}$$

Using Eqs. (4.25) and (4.14), we have

$$\mathcal{D}(x; x_-)\mathcal{G}(x, x'; t) = -\mathcal{F}(x; x_-)\hat{\lambda}_t\mathcal{G}(x, x'; t), \ x' > x_-, \tag{4.26a}$$

$$\mathcal{D}(x; x_+)\mathcal{G}(x, x'; t) = +\mathcal{F}(x; x_+)\hat{\lambda}_t\mathcal{G}(x, x'; t), \ x' < x_+. \tag{4.26b}$$

Using Eqs. (4.26) and (4.16), we obtain

$$\mathcal{D}(x; x_-)\mathscr{G}(x, x'; t, t') = -\mathcal{F}(x; x_-)\hat{\lambda}_t\mathscr{G}(x, x'; t, t'), \ x' > x_-, \tag{4.27a}$$

$$\mathcal{D}(x; x_+)\mathscr{G}(x, x'; t, t') = +\mathcal{F}(x; x_+)\hat{\lambda}_t\mathscr{G}(x, x'; t, t'), \ x' < x_+. \tag{4.27b}$$

Using Eqs. (4.26), (4.19) and identity (see Appendix E.1)

$$(\hat{\lambda}_t - ik)e^{-iEt} = 0, \tag{4.28}$$

we find

$$\mathcal{D}(x; x_\pm)\psi(x, t) = \pm\mathcal{F}(x; x_\pm)\hat{\lambda}_t\psi(x, t). \tag{4.29}$$

We find that this equation amounts to the boundary conditions

$$\left(\frac{\partial}{\partial x} \mp \hat{\lambda}_t\right)\psi(x, t)\Big|_{x=x_\pm} = 0. \tag{4.30}$$

This is the outgoing wave boundary condition in the time domain for the wave function $\psi(x, t)$ as it should be from a naive guess using the Fourier transform of $\psi(x, t)$. It is rigorously proved here to be the general characterization of the operator $\hat{\lambda}_t$.

4.2.4 Matrix form of the time-dependent Schrödinger equation

It has been shown that the outgoing wave boundary condition in the time domain is closely related to the operator $\hat{\lambda}_t$. Therefore, one needs to derive the TDSE involving $\hat{\lambda}_t$ to incorporate the outgoing wave boundary condition. To this end, we introduce the new vector

$$\begin{pmatrix} \psi(x,t) \\ \tilde{\psi}(x,t) \end{pmatrix}, \tag{4.31}$$

where

$$\tilde{\psi}(x,t) = \hat{\lambda}_t \psi(x,t). \tag{4.32}$$

Then the TDSE can be rewritten in terms of the operator $\hat{\lambda}_t$,

$$\left[\hat{\lambda}_t - \begin{pmatrix} 0 & 1 \\ -2\tilde{\mathcal{H}}(t) & \mathcal{F} \end{pmatrix} \right] \begin{pmatrix} \psi(x,t) \\ \tilde{\psi}(x,t) \end{pmatrix} = 0, \tag{4.33}$$

where

$$\mathcal{F} = \mathcal{F}(x; x_-) + \mathcal{F}(x; x_+). \tag{4.34}$$

4.2.5 Siegert state expansion: coupled Volterra equations for inner region

Here we seek the solution to Eq. (4.33) in terms of the stationary Siegert states (SSs). As discussed in Chapter 3, we adopt the set of the two-component vector Eq. (3.13) as the basis functions to uniquely define the expansion coefficients of the wave packet in terms of the SSs. Hence, we seek the solution to Eq. (4.33) for inner region $x_- < x < x_+$ in the form

$$\begin{pmatrix} \psi(x,t) \\ \tilde{\psi}(x,t) \end{pmatrix} = \sum_n a_n(t) \begin{pmatrix} \phi_n(x) \\ ik_n\phi_n(x) \end{pmatrix}. \tag{4.35}$$

Substituting this expansion into Eq. (4.33), multiplying the factor

$$(\phi_n(x)\ \tilde{\phi}_n(x)) \begin{pmatrix} -\mathcal{F} & 1 \\ 1 & 0 \end{pmatrix} \tag{4.36}$$

form the left, integrating over $[x_-, x_+]$, and using the orthonormal relationship Eq. (3.18), one obtains

$$ik_n(\hat{\lambda}_t - ik_n)a_n(t) + \sum_m U_{nm}(t)a_m(t) = 0, \tag{4.37a}$$

$$a_n(t)|_{t\to-\infty} = \delta_{n0}e^{-iE_0t} \tag{4.37b}$$

where

$$U_{nm}(t) = \int_{x_-}^{x_+} \phi_n(x)U(x,t)\phi_m(x)\,dx. \tag{4.38}$$

Using the retarded Green's function $g(t;k)$ for the operator $\hat{\lambda}_t - ik_n$, see Appendix E.2, we have an integral form of this equation,

$$a_n(t) = \delta_{n0}e^{-iE_0t} + \frac{i}{k_n}\sum_m \int_{-\infty}^{t} g(t-t';k_n)U_{nm}(t')a_m(t')\,dt'. \tag{4.39}$$

These are the coupled Volterra equations of the second kind. The equation Eq. (4.39) indicates that all the past information of $a_m(t)$ is required to calculate the value of $a_n(t)$ for a given time. This originate from the non-local property of the operator $\hat{\lambda}_t$ Eq. (4.24), see Appendix E.1, in the outgoing wave boundary condition Eq. (4.30).

Outgoing wave boundary condition in time domain has been intensively studied in literatures; for instance, see [79, 80, 81, 82] and references therein. In [80, 81, 82], outgoing wave boundary conditions for the Crank-Nicolson finite difference scheme were derived in 1D and 2D cases. The resulting boundary conditions are equivalent to Eq. (4.30). In these literatures, it was pointed out that these are non-local with respect to time since the pseudodifferential operator Eq. (4.24) is incorporated. Recently, Tolstikhin developed the Siegert state approach to implement outgoing wave boundary conditions in time domain [21, 22, 23]. The SS formulation gave us new perspectives, in particular, for physics of laser-atom interaction because photoelectron spectra can be exactly described by the expansion coefficients of a wave packet $a_n(t)$, Eq. (4.35), for one-electron systems being bound in short range potentials.

4.2.6 Photoelectron spectra

To define the photoelectron spectrum, we need to expand the wave function in terms of the *out* states. The out states are the scattering states of which the wave packets formed by them recede from the interaction region in remote future to the left

and right, respectively; see Appendix D.1.2 for the detailed discussions. Using the out states, the wave function can be expanded as

$$\begin{aligned}\psi(x,t) &= \sum_{n\in\{b\}} C_n(t)\phi_n(x) + \int_0^\infty [C_-(k,t)\varphi_-^{\text{out}}(x,k) \\ &\quad + C_+(k,t)\varphi_+^{\text{out}}(x,k)]\,\frac{dk}{2\pi},\end{aligned} \tag{4.40}$$

where $n \in \{b\}$ indicates the summation over the bound states of the atomic Hamiltonian H Eq. (4.8). For $t \to \infty$ coefficients $C_n(t)$ and $C_\pm(k,t)$ are

$$C_n(t)|_{t\to\infty} = C_n e^{-iE_n t}, \tag{4.41a}$$

$$C_\pm(k,t)|_{t\to\infty} = C_\pm(k)e^{-iEt} \tag{4.41b}$$

where

$$C_n = \delta_{n0} - i\sum_m \int_{-\infty}^\infty e^{iE_n t}U_{nm}(t)a_m(t)dt, \tag{4.42a}$$

$$C_\pm(k) = ke^{\mp ikx_\pm}\int_{-\infty}^\infty \psi(x_\pm,t)e^{iEt}dt. \tag{4.42b}$$

The probability amplitude P_n and $P_\pm(k)$ for the electron being found in the bound states n and ionized with momenta k are

$$P_n = |C_n|^2 = |\delta_{n0} - iA_n(E_n)|^2, \tag{4.43a}$$

$$P_\pm(k) = |C_\pm(k)|^2 = k^2\left|\sum_n \frac{A_n(E)}{k_n(k-k_n)}\phi_n(x_\pm)\right|^2, \tag{4.43b}$$

where $P_\pm(k)$ represent the probability amplitude of the ionized electron leaving from the interaction region to the left $(-)$ and right $(+)$ direction, respectively, and

$$A_n(E) = \sum_m \int_0^T e^{iEt}U_{nm}(t)a_m(t)\,dt. \tag{4.44}$$

See [22] for the detailed derivations. The energy distributions $P(E)$ and total ionization probabilities P_{ion} are

$$P(E) = \frac{P_-(k)+P_+(k)}{2\pi k}, \quad P_{\text{ion}} = \int_0^\infty P(E)\,dE. \tag{4.45}$$

The unitarity condition reads,

$$\sum_{n\in\{b\}} P_n + \int_0^\infty [P_-(k)+P_+(k)]\,\frac{dk}{2\pi} = 1. \tag{4.46}$$

4.2.7 Numerical implementations

4.2.7.1 The Siegert pseudostate expansion

The formulation presented in Sec. 4.2.5 and 4.2.6 is numerically implemented with the Siegert pseudostates (SPSs). We solve the SPS eigenvalue problem Eq. (3.28). Let N be the number of the basis functions for expanding the wave functions Eq. (3.27), we obtain the set of $2N$ solutions of Eq. (3.28). The wave packet is expanded using all of them in the same manner as Eq. (4.35). So, the summations in Eq. (4.39), Eq. (4.43b), and Eq. (4.44) run over $2N$ SPSs.

4.2.7.2 Numerical solutions for the coupled Volterra equations

To solve the coupled Volterra equation Eq. (4.39), we employ the simple trapezoidal formula. The time interval $0 \leq t \leq T$ is divided into equally spaced time steps $t_i = ih$, where $i = 0, \ldots, M$ and $h = T/M$. At time t_i, we use the following quadrature to evaluate the integral in Eq. (4.39),

$$\int_0^{t_i} \frac{f(t')}{(t_i - t')^{1/2}} dt' \approx \sqrt{h} \sum_{j=0}^{i} \omega_j^{(i)} f(t_j), \tag{4.47}$$

where

$$\omega_0^{(i)} = \sqrt{i} - \sqrt{i-1}, \tag{4.48a}$$

$$\omega_j^{(i)} = \sqrt{i-j+1} - \sqrt{i-j-1}, \ j = 1, \ldots, i-1, \tag{4.48b}$$

$$\omega_i^{(i)} = 1 \tag{4.48c}$$

Note that the integration variable is changed to $\tau = \sqrt{t_i - t'}$ from t' to eliminate the singularity of the integral at $t = t_i$ in Eq. (4.47)

After the integration with respect to time, we obtain $2N$ linear simultaneous equations for $a_n(t_i)(n = 1, \ldots, 2N)$. This can be solved using any standard routine in numerical calculations.

When we calculate the photoelectron spectra in Chapters 5 and 6, the time step h is chosen so that the error on the unitarity Eq. (4.46) is less than 1%.

4.3 Three dimensional case

4.3.1 The Kramers-Henneberger frame

We further extend our approach to the three-dimensional (3D) case. Most of the formulas here parallel those of the 1D case except for the inclusion of the partial waves.

The TDSE in the laboratory frame in the length gauge reads,

$$i\frac{\partial\psi_{\rm L}(\mathbf{r}_{\rm L},t)}{\partial t} = \left(-\frac{1}{2}\Delta_{\rm L} + V(r_{\rm L}) + \mathbf{r}_{\rm L}\cdot\mathbf{F}(t)\right)\psi_{\rm L}(\mathbf{r}_{\rm L},t). \tag{4.49}$$

It is assumed that the laser pulse $\mathbf{F}$ vanishes beyond the time interval $0 \le t \le T$

$$\mathbf{F}(t\le 0) = \mathbf{F}(t\ge T) = 0, \tag{4.50}$$

and an atomic potential has a finite range,

$$V(r)|_{r\ge R} = 0. \tag{4.51}$$

Let $\boldsymbol{\alpha}(t)$ be the classical trajectory of a free electron in the laser pulse,

$$\ddot{\boldsymbol{\alpha}}(t) = -\mathbf{F}(t), \tag{4.52a}$$

$$\dot{\boldsymbol{\alpha}}(0) = \boldsymbol{\alpha}(0) = \mathbf{0}, \tag{4.52b}$$

where the dot denotes the differentiation with respect to time. The Kramers-Henneberger (KH) transformations is defined by

$$\mathbf{r}_{\rm L} = \mathbf{r}_{\rm KH} + \boldsymbol{\alpha}(t), \tag{4.53a}$$

$$\psi_{\rm L}(\mathbf{r}_{\rm L},t) = \exp\left(i\dot{\boldsymbol{\alpha}}(t)\cdot\mathbf{r}_{\rm L} - \frac{i}{2}\int_0^t \dot{\boldsymbol{\alpha}}^2(t')dt'\right)\psi_{\rm KH}(\mathbf{r}_{\rm KH},t). \tag{4.53b}$$

Substituting these equations into Eq. (4.49), one obtains the TDSE in the KH frame,

$$i\frac{\partial\psi_{\rm KH}(\mathbf{r}_{\rm KH},t)}{\partial t} = \left(-\frac{1}{2}\Delta_{\rm KH} + V(|r_{\rm KH}+\boldsymbol{\alpha}(t)|)\right)\psi_{\rm KH}(\mathbf{r}_{\rm KH},t). \tag{4.54}$$

In the following, the subscript “KH" is omitted for brevity. The effect of the laser pulse can be correctly taken account into the TDSE for the box size

$$a > R + \max[\boldsymbol{\alpha}(t)]. \tag{4.55}$$

It is assumed that the laser parameters are chosen so that the electron comes back to the origin with zero velocity when the pulse is over,

$$\dot{\boldsymbol{\alpha}}(T) = \boldsymbol{\alpha}(T) = 0. \tag{4.56}$$

We expand the wave function in terms of the spherical harmonics,

$$\psi(\mathbf{r},t)=\sum_{lm}\psi_{lm}(r,t)Y_{lm}(\Omega). \tag{4.57}$$

Substituting this, we obtain coupled equations

$$\left[i\frac{\partial}{\partial t}-H_l\right]\psi_{lm}(r,t)-\sum_{l'm'}U_{lm,l'm'}(r,t)\psi_{l'm'}(r,t)=0, \tag{4.58}$$

where

$$H_l=-\frac{1}{2}\frac{d^2}{dr^2}+\frac{l(l+1)}{2r^2}+V(r), \tag{4.59a}$$

$$U_{lm,l'm'}(r,t)=\int Y^*_{lm}(\Omega)U(\mathbf{r},t)Y_{lm}(\Omega)d\Omega, \tag{4.59b}$$

$$U(\mathbf{r},t)=V(|\mathbf{r}+\boldsymbol{\alpha}(t)|)-V(r). \tag{4.59c}$$

4.3.2 The Green's function

The stationary outgoing wave Green's function is defined by

$$(E-H_l)G_l(r,r';k)=\delta(r-r'), \tag{4.60}$$

subject to the boundary conditions

$$G_l(0,r';k)=0, \tag{4.61}$$

and

$$\left(\frac{\partial}{\partial r}-ik+\frac{1}{a}\sum_{p=1}^{l}\frac{z_{lp}}{ika+z_{lp}}\right)G_l(r,r';k)\bigg|_{r=a}=0. \tag{4.62}$$

The time-dependent retarded Green's function is defined by

$$\left(i\frac{\partial}{\partial t}-H_l\right)\mathcal{G}_l(r,r';t)=\delta(t)\delta(r-r'), \tag{4.63a}$$

$$\mathcal{G}_l(r,r';t)\big|_{t<0}=0. \tag{4.63b}$$

The relationship between the stationary and time-dependent Green's function is given by

$$\mathcal{G}_l(r,r';t)=\int_{-\infty}^{\infty}G_l(r,r';k)e^{-iEt}\frac{dE}{2\pi}. \tag{4.64}$$

The initial condition of the wave packet is

$$\psi_{lm}(r,t)|_{t\to-\infty} = \delta_{ll_0}\delta_{mm_0}\phi_{l_0n_0}(r)e^{-iE_{l_0n_0}t}, \tag{4.65}$$

where $\phi_{l_0n_0}(r)$ is the bound state of the atomic Hamiltonian

$$(H_{l_0} - E_{l_0n_0})\phi_{l_0n_0}(r) = 0. \tag{4.66}$$

Then the wave packet at some moment t can be written using the Green's function,

$$\psi_{lm}(r,t) = \delta_{ll_0}\delta_{mm_0}\phi_{l_0n_0}(r)e^{-iE_{l_0n_0}t} + \sum_{l'm'}\int_{-\infty}^{\infty}dt'\int_0^a dr'\mathcal{G}_l(r,r';t-t')U_{lm,l'm'}(r',t')\psi(r',t'). \tag{4.67}$$

4.3.3 Outgoing wave boundary condition in the time domain

Here we derive the outgoing wave boundary condition in the 3D case. Using Eq. (4.62),

$$\mathcal{D}(r;a)G_l(r,r';k) = \mathcal{F}(r;a)\left(ik - \frac{1}{a}\sum_{p=1}^{l}\frac{z_{lp}}{ika + z_{lp}}\right)G_l(r,r';k) \tag{4.68}$$

Using this, we obtain

$$\mathcal{D}(r;a)\mathcal{G}_l(r,r';t) = \mathcal{F}(r;a)\left[\hat{\lambda}_t - \frac{1}{a}\sum_{p=1}^{l}\frac{z_{lp}}{a\hat{\lambda}_t + z_{lp}}\right]\mathcal{G}_l(r,r';t). \tag{4.69}$$

Using this and Eq. (4.67), we obtain

$$\mathcal{D}(r;a)\psi_{lm}(r,t) = \mathcal{F}(r;a)\left[\hat{\lambda}_t - \frac{1}{a}\sum_{p=1}^{l}\frac{z_{lp}}{a\hat{\lambda}_t + z_{lp}}\right]\psi_{lm}(r,t) \tag{4.70}$$

We find that this equation accounts for the condition,

$$\left(\frac{d}{dr} - \hat{\lambda}_t + \frac{1}{a}\sum_{p=1}^{l}\frac{z_{lp}}{a\hat{\lambda}_t + z_{lp}}\right)\psi_{lm}(r,t)\bigg|_{r=a} = 0 \tag{4.71}$$

This is the outgoing wave boundary condition in time domain for the 3D case.

4.3.4 Matrix form of the time-dependent Schrödinger equation

We must rewrite the TDSE again in terms of $\hat{\lambda}_t$ to incorporate the outgoing wave boundary condition. To this end, let us define a new vector,

$$\boldsymbol{\psi}_{lm}(r,t) = \begin{pmatrix} \psi_{lm}(r,t) \\ \tilde{\psi}_{lm}(r,t) \\ \psi_{lm1}(t) \\ \cdots \\ \psi_{lml}(t) \end{pmatrix}, \tag{4.72}$$

where

$$\psi_{lmp}(t) = -\frac{z_{lp}}{a}(\hat{\lambda}_t + z_{lp}/a)^{-1}\psi_{lm}(a,t), \ (p = 1, \ldots, l). \tag{4.73}$$

Note that there are l additional components compared to the 1D case. We also define the matrix operator

$$\Lambda_l = \begin{pmatrix} 0 & 1 & 0 & \cdots & 0 \\ -2\tilde{H}_l & \mathcal{F}(r;a) & \mathcal{F}(r;a)/a & \cdots & \mathcal{F}(r;a)/a \\ -z_{l1}\mathcal{F}^T(r;a)/a & 0 & & & \\ \vdots & \vdots & & \boxed{-z_{lp}/a} & \\ -z_{ll}\mathcal{F}^T(r;a)/a & 0 & & & \end{pmatrix}. \tag{4.74}$$

Here the action of the operator $\mathcal{F}^T$ on the function $u(r)$ is defined by

$$\mathcal{F}^T(r;a)u(r) = u(a). \tag{4.75}$$

The boxed object represents the $l \times l$ square diagonal matrix with the elements inside the box. So, $\boxed{-z_{lp}/a}$ denotes the $l \times l$ diagonal matrix with elements $-z_{lp}/a$ $(p = 1, \ldots, l)$. Then the TDSE is recast into

$$[\hat{\lambda}_t - \boldsymbol{\Lambda}_l]\boldsymbol{\psi}_{lm}(r,t) + 2\sum_{l'm'} \boldsymbol{U}_{lm,l'm'}(t)\boldsymbol{\psi}_{l'm'}(r,t) = 0, \tag{4.76}$$

where

$$\boldsymbol{U}_{lm,l'm'} = \begin{pmatrix} 0 & 0 & \cdots & 0 \\ U_{lm,l'm'}(r,t) & 0 & \cdots & 0 \\ 0 & 0 & \cdots & 0 \\ \vdots & \vdots & \vdots & \vdots \\ 0 & 0 & \cdots & 0 \end{pmatrix}. \tag{4.77}$$

4.3.5 Siegert state expansion: coupled Volterra equations for the inner region

As demonstrated in the 1D case, we employ the set of the vectors Eq. (3.35) to uniquely define the expansion coefficients of the wave packet. We seek the solution to the Eq. (4.76) in the form,

$$\boldsymbol{\psi}_{lm}(r,t) = \sum_n a_\nu(t)\boldsymbol{\phi}_{ln}(r),\ 0 \le r \le a, \tag{4.78}$$

where a new index ν represents the enumeration of the quantum numbers

$$\nu = (l, m, n). \tag{4.79}$$

Similarly we write $\nu' = (l', m', n')$. Substituting Eq. (4.78) into Eq. (4.76), and using the orthogonality Eq. (3.41), we obtain

$$ik_{ln}(\hat{\lambda}_t - ik_{ln})a_\nu(t) + \sum_{\nu'} U_{\nu\nu'}(t)a_{\nu'(t)} = 0, \tag{4.80a}$$

$$U_{\nu\nu'}(t) = \int_0^a \phi_{ln}(r)\boldsymbol{W}_l U_{lm,l'm'}(r,t)\phi_{l'n'}(r)dr. \tag{4.80b}$$

Using the Green's function $g(t;k)$ for the operator $\hat{\lambda}_t - ik$, this equation is recast into the integral form.

$$a_\nu(t) = \delta_{\nu 0}e^{-iE_0 t} + \frac{i}{k_{ln}}\sum_{\nu'}\int_{-\infty}^{t} g(t-t';k_{ln})U_{\nu\nu'}(t')a_{\nu'}(t')dt', \tag{4.81}$$

where $\delta_{\nu 0} = \delta_{ll_0}\delta_{mm_0}$, and $E_0 = E_{l_0 n_0}$. It is worth to remark that this equation has the same form as the 1D case Eq. (4.39).

4.3.6 Photoelectron spectra

The large time asymptotic of the wave function $\psi_{lm}(r,t)$ has the form

$$\psi_{lm}(r,t)|_{t\to\infty} = \sum_{n\in\{b\}_l} C_\nu \phi_{ln}(r)e^{-iE_{ln}t} + \int_0^\infty C_{lm}(k)\varphi_l(r,k)e^{-iEt}\frac{dk}{2\pi}. \tag{4.82}$$

Let $A_\nu(E)$ be a function defined by

$$A_\nu(E) = \sum_{\nu'}\int_{-\infty}^{\infty} U_{\nu\nu'}(t)a_{\nu'}(t)e^{iEt}dt. \tag{4.83}$$

Using this the probability amplitude for the electron being found in the bound state when the laser pulse terminates is

$$P_\nu = |C_\nu|^2 = |\delta_{\nu 0} - iA_\nu(E_{ln})|^2,\ \nu \in \{b\}, \tag{4.84}$$

where the symbol $\{b\}_l$ denotes the set of the bound state of the atomic Hamiltonian H_l Eq. (4.59a), and $\{b\}$ denotes the collection of the sets $\{b\}_l$ for all the value of l.

The momentum distribution of the photoelectron in a partial wave is

$$P_{lm}(k) = |C_{lm}(k)|^2 = \left| \frac{k}{e_l(ka)} \sum_n \frac{A_\nu(E)\phi_{ln}(a)}{k_{ln}(k-k_{ln})} \right|^2. \tag{4.85}$$

The function $e_l(kr)$ is related to the spherical Hankel function of first kind; see Appendix C. The 3D momentum distribution of the photoelectron is

$$\begin{aligned} P(\boldsymbol{k}) &= \frac{1}{2\pi} \left| \sum_\nu c_{lm}(E) Y_{lm}(\Omega) \right|^2 \\ &= \frac{1}{2\pi} \left| \sum_\nu \frac{A_\nu(E)\phi_{ln}(a) Y_{lm}(\Omega)}{e_l(ka)k_{ln}(k-k_{ln})} \right|^2 \end{aligned} \tag{4.86}$$

where $\boldsymbol{k} = (k, \Omega)$, and the function $c_{lm}(E)$ is defined by

$$c_{lm}(E) = \frac{1}{e_l(ka)} \int_{-\infty}^{\infty} \psi_{lm}(a,t) e^{iEt} dt. \tag{4.87}$$

The energy distribution and the probability amplitude of transitions to the continuum in a partial wave are

$$P_{lm}(E) = \frac{P_{lm}(k)}{2\pi k},\ P_{lm}^{(c)} = \int_0^\infty P_{lm}(E) dE. \tag{4.88}$$

The total energy distribution of the photoelectron is

$$P(E) = \sum_{lm} P_{lm}(E) = k \int P(\boldsymbol{k}) d\Omega. \tag{4.89}$$

The total probability of transitions to the continuum is

$$P_c = \sum_{lm} P_{lm}^{(c)} = \int_0^\infty P(E) dE = \int P(\boldsymbol{k}) d^3\boldsymbol{k}. \tag{4.90}$$

Finally, the unitarity condition is

$$\sum_{\nu \in \{b\}} P_\nu + P_c = 1. \tag{4.91}$$

See [23] for the detailed derivations.

4.3.7 Numerical implementations

4.3.7.1 Siegert pseudostate expansion

The formulation in Sec. 4.3.5 and 4.3.6 are implemented by the Siegert pseudostates (SPSs). For each l in the partial wave expansion of the total wave function Eq. (4.57), we solve the SPS eigenvalue problem Eq. (3.48). Let N be the number of basis functions to expand the wave function Eq. (3.47), we obtain a set of $2N + l$ SPSs. Then the partial wave component $\psi_{lm}(r, t)$ in Eq. (4.57) can be expanded in terms of the $2N + l$ SPSs in the manner of Eq. (4.78). The magnetic quantum number runs from $-l$ to l with the step of 1 in Eq. (4.57), we obtain set of the $(2N + l) \times (2l + 1)$ Volterra equations in Eq. (4.81) for given l. Let $l_{\max}$ be the maximum angular momentum in the partial wave expansion Eq. (4.57). Thus we obtain $N_{\rm tot} = \sum_{l=0}^{l_{\max}} (2N + l) \times (2l + 1)$ coupled Volterra equations in Eq. (4.81). The indices ν and ν' in Eq. (4.81) runs over all the possible combination of (l, m, n) so that the total number of the elements is $N_{\rm tot}$.

4.3.7.2 Numerical solutions for the coupled Volterra equations

The numerical procedures to solve Eq. (4.81) is the same as the 1D case; see the chapter 4.2.7.2.

Chapter 5

Interference fringes of the photoelectron wave packets in the above-threshold ionization peaks

5.1 Introduction

In Chapters 5 and 6, we study photoelectron spectra of the negative ion both in 1D and 3D cases. The main goal of these Chapter is to provide general and hitherto unknown features of the ionization dynamics in the stabilization regime by analysing the photoelectron spectra more fully than earlier studies for the total ionization probabilities [12, 13, 5].

First, we study the 1D case for both the perturbation regime and stabilization regime. In the perturbation regime, the amplitude of the classical trajectory α_0 is very small compared with the range of the atomic potential. Then the perturbation theory is implemented by approximating the KH potential in the first order of α_0. We show that the result obtained from our SS expansion in the KH frame developed in the previous Chapter is consistent with that from the perturbation theory in the KH frame. Thus we confirm the validity of our numerical scheme. Next, we move to the stabilization regime, where the laser is intense enough for the stabilization to occur. In this regime, oscillating substructures are found in the above-threshold ionization (ATI) peaks [83, 39]. Since a large number of optical cycles are contained in the laser pulse, the electron is expected to follow the slowly varying pulse envelope adiabatically instead of each optical cycle. Based on this picture, we analyze the ATI spectrum on the basis of the adiabatic version of the high-frequency Floquet theory (HFFT). As far as we know, ours is its first application to the photoelectron spectrum although the idea of the adiabatic version of the HFFT appears in several literatures in fragments, see for

example [11, 76]. The adiabatic HFFT attributes the oscillating substructure in the ATI peaks to the interference fringes of the photoelectron wave packets produced at different moments in time, and show how the stabilization plays a key role. The conditions for the laser parameters are clarified to clearly observe this oscillating substructure.

Second, we extend our study to the 3D case, and show that the oscillating substructure persists in the ATI peaks for hydrogen negative ion H^- [40]. The numerical calculations with a wide range of laser parameters show that the oscillating substructures emerge with the same conditions for the laser parameters found in the 1D case. It is also shown that the dependency of their structures on the laser parameters can be explained in terms of the interference picture of the photoelectron wave packets. The interference picture thus remains to be an assumption to be indirectly verified in the 3D case. It is not trivial to show that this picture is again the decisive mechanism of the oscillating substructures in the 3D case. We verify the interference picture by a numerical experiment in which the polarization axis is made to vary its direction adiabatically in time. Because the photoelectron wave packet tends to get ejected along the polarization axis, this variation in the polarization axis prevents the photoelectron's trajectories from crossing. Accordingly the oscillating substructures are shown to get suppressed. Thus it is confirmed that the oscillating substructures originate from the interference of the photoelectron wave packets. It is shown that the oscillating substructure is again reconstructed in terms of the adiabatic version of the HFFT based on the interference picture. In the 3D calculations, we find one more prominent peak at the vicinity of zero energy in the photoelectron spectrum. We shall call it the *slow electron peak* (SEP) [45]. The generation of the SEP is counterintuitive since the photon energy is about ten times larger than the ionization potential of H^-. The discussion of its origin is postponed till the subsequent Chapter since its physics is quite different from the interference fringes we discuss here.

5.2 One dimensional case

We work on the two extreme regimes, namely, perturbative and stabilization regimes. In the perturbative regime, the maximum amplitude of the classical trajectory $\alpha_0 = \max[x(t)] \approx F_0/\omega^2$ falls within a much smaller region than the outer most range

of the potential. This regime can be thus treated by the perturbation theory with respect to α_0. The weak laser pulse is thus exploited for checking the consistency of our numerical scheme by comparing the perturbative and TDSE results.

In the stabilization regime, we treat the ultra-intense field so that the field amplitude α_0 becomes comparable to the outer most range of the atomic potential. In this regime, we find the oscillating substructures in the above-threshold ionization (ATI) peaks. This section develops toward clarifying the origin and the role of the stabilization.

In the 1D calculations to follow, we model the one-electron system by the Eckart potential,

$$V(x) = -\frac{15/8}{\cosh^2 x}. \tag{5.1}$$

This potential is employed to clearly illustrate the oscillating substructure in the ATI peaks in Sec. 5.2.2. This potential, Eq. (5.1), can be cut off for the box size $|X| > 5$ beyond which $|V(x)| \ll 1$. The bound states energies are $E_0 = -1.125$ and $E_1 = -0.125$. In the following calculations, the ground state E_0 is chosen as the initial state for the electron. The profile of the laser pulse is given by

$$F(t) = F_0 f(t) \cos \omega t, \tag{5.2}$$

where $f(t)$ is the pulse envelope

$$f(t) = \sin^2 \frac{\pi t}{T}. \tag{5.3}$$

The parameters F_0, T and ω represent the maximum field amplitude, pulse duration and frequency; we set $\omega = \pi$ and $T = 200$ so that the number of the optical cycles $n_{\rm oc} = 100$.

5.2.1 The perturbative regime

In this regime it is expected that almost all the population stays in the ground state when pulse is over. Thus, the expansion coefficients of the wave packet in Eq. (4.35) and (4.39) can be approximated as

$$a_m(t) \approx \delta_{m0} e^{-iE_0 t}. \tag{5.4}$$

The interaction terms between the electron and laser field Eq. (4.9) can be approximated by

$$U(x,t) = V(x + x(t)) - V(x) \approx \frac{dV}{dx} x(t), \tag{5.5}$$

where $x(t)$ is free electron's classical trajectory in the laser field, Eqs. (2.4), (2.5). The first order result of the perturbation theory for the spectrum is given by

$$P_{\mathrm{PT}}(E) = |x(E - E_0)|^2 \, \frac{|d_-(k)|^2 + |d_+(k)|^2}{2\pi k}, \tag{5.6}$$

where $d_\pm(k)$ is the dipole matrix element

$$d_\pm(k) = \int \varphi_\pm^{\mathrm{out}*}(x,k) \, \frac{dV(x)}{dx} \, \phi_0(x) \, dx, \tag{5.7}$$

the function $\phi_0(x)$ and $\varphi_\pm^{\mathrm{out}}$ are the ground state wave function and scattering state of momenta k Eq. (3.20) of the atomic Hamiltonian Eq. (4.8). The function $x(E)$ is the Fourier transformation of the classical trajectory (see Appendix G for its explicit expression).

For a numerical examination, we adopt $F_0 = 0.1$; thus $\alpha_0 = F_0/\omega^2 \approx 0.01$ is sufficiently smaller than the maximum range of the atomic potential $[-5, 5]$. The photoelectron spectrum for the present model is shown in Fig. 5.1. The black line represents the TDSE results; one can clearly see a series of ATI peaks separated by the photon energy $\omega = \pi$. The excitation probability in this calculation is about 1.96×10^{-12}. The height of the one-photon absorption peak is about 3.1×10^{-2}, hence the one-photon peak from the excited state can be estimated as $(1.96 \times 10^{-12}) \times (3.1 \times 10^{-2}) \approx 6.1 \times 10^{-14}$, which is below visibility. The red line represents the results from the first order perturbation theory. In the figure, the perturbation theory perfectly reproduced the one-photon peak, and the envelope of the spectrum obtained by dropping the rapidly oscillating factor $\sin(ET/2)$. This agreement in turn confirms the overall consistency of our numerical scheme.

5.2.2 Stabilization regime

Having tested our method, we further study the photoelectron spectrum for the laser pulse of the ultra-high intensity. We adopt $F_0 = 30$, hence $\alpha_0 \approx 3.04$; this is now comparable to the range of the atomic potential. Thus we extend the interaction

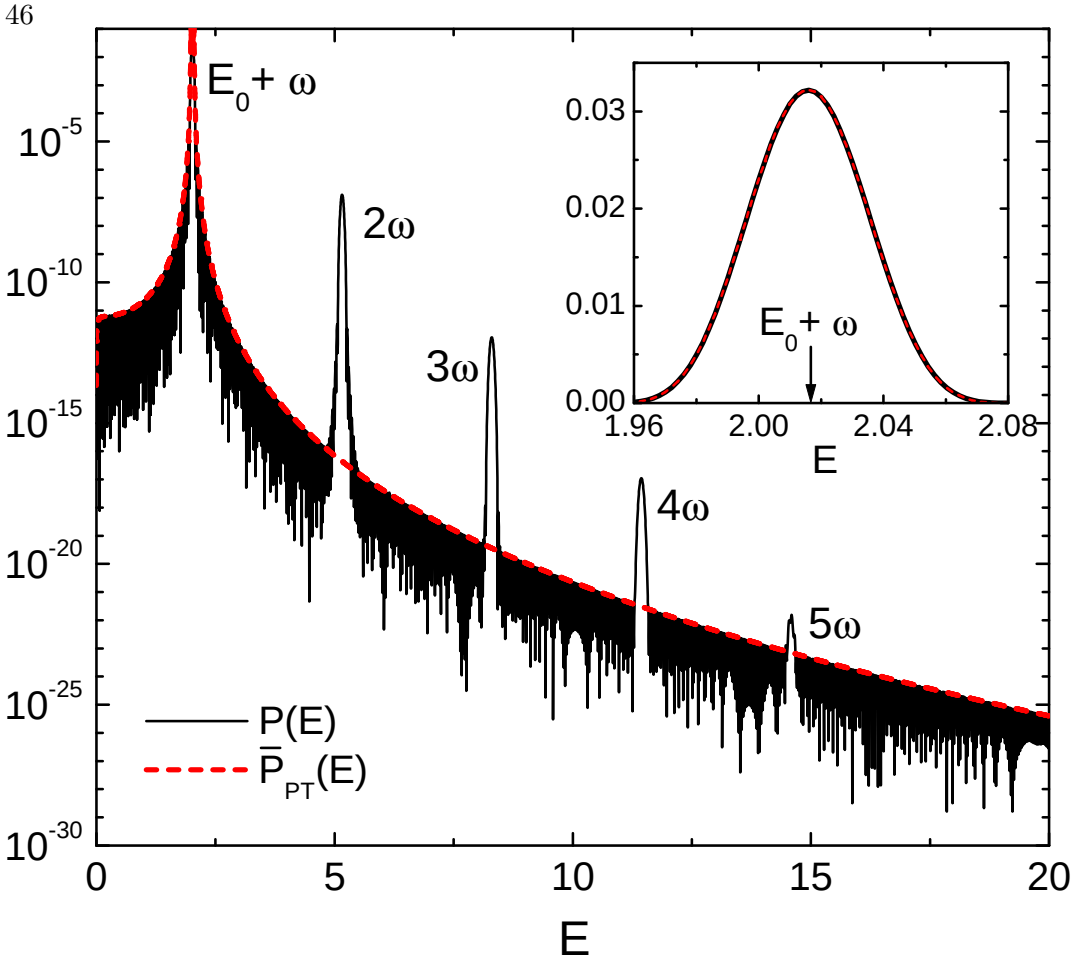

Figure 5.1: Present results for the model considered in Ref. [22], see Eqs. (5.1) and (5.2) with $F_0 = 0.1$, $T = 200$, and $\omega = \pi$. One can clearly see a number of ATI peaks in the photoelectron spectrum $P(E)$ produced by multiphoton absorption from the ground state. For comparison, the envelope $\bar{P}_{PT}(E)$ of the perturbation theory results obtained by dropping the rapidly oscillating factor $\sin^2(ET/2)$ in Eq. (5.6) is also shown. This agreement in turn confirms the general consistency of our numerical scheme.

region, Eq. (4.5), in our numerical treatment to $[x_-, x_+] = [-8, 8]$. The photoelectron spectrum is shown in Fig. 5.2a. The ATI peaks can be seen again acquiring a quite different shapes. The first peak is enlarged in the linear scale in Fig. 5.2b; one can clearly see the oscillating substructures. Let us discuss the origin of this structure.

5.2.3 Analysis in terms of the high-frequency Floquet theory

Since the photon energy corresponding to the center of the wave length of our laser pulse is much higher than the binding energy of the electron, the adequate framework

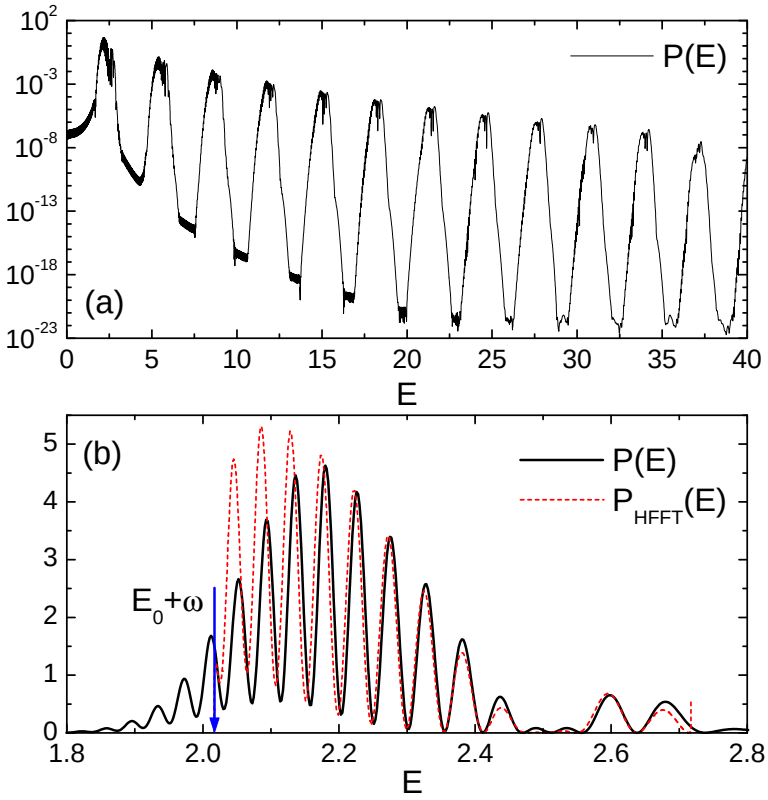

Figure 5.2: (a) Photoelectron spectrum $P(E)$ for the same model as in Fig. 5.1, but for a very strong laser pulse with $F_0 = 30$. (b) Enlarges the first ATI peak in linear scale. Two bunches of oscillations can be seen at energies around $E(\alpha = \alpha_{c1}) + \omega \approx 2.19$ and $E(\alpha = \alpha_{c2}) + \omega \approx 2.62$. Here α_{c1} and α_{c2} are the first and second threshold values of the excursion amplitude of the free electron's classical trajectory for suppression of the ionization rate shown in Fig. 5.3. $P_{\rm HFFT}(E)$ shows the results obtained from Eq. (5.12).

is the high-frequency Floquet theory (HFFT). As discussed in Sec. 2.3, The quivering motion of the KH potential along the classical trajectory $x(t)$ can be averaged out for a monochromatic high-frequency laser field; the the optical period of the laser field is much shorter than the time scale of the electronic motion. Thus the effective Hamiltonian, called the dressed Hamiltonian, can be found for the electron, Eq. (2.10b). Let $E_0(\alpha)$ and $\phi_0(x;\alpha)$ be the ground state energy and wave function of the dressed Hamiltonian. The function $E_0(\alpha)$ added by the photon energy ω and one-photon ionization rate $\Gamma(\alpha)$, defined by Eq. (2.11), (2.12) and (2.9), are shown in Fig. 5.3a. In the figure, $E(\alpha)$ goes up as the dressed potential $V_0(x;\alpha)$ becomes shallower; the electron is loosely bound as the excursion amplitude grows. $\Gamma(\alpha)$ initially increases but it begins to decrease after

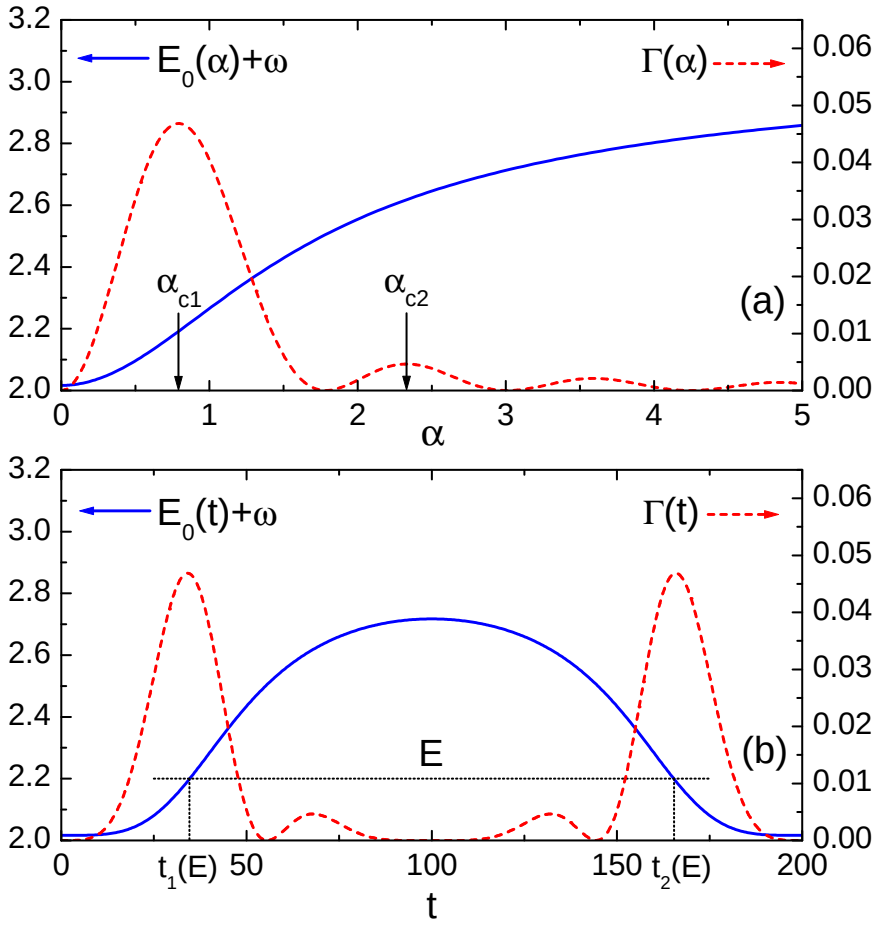

Figure 5.3: The energy and width of the initial atomic state "dressed" by the high-frequency laser field as functions of the amplitude α of classical trajectory and time t related to each other by Eq. (5.8) with $F_0/\omega^2 \approx 3$.

the critical value α_{c1}. This is the stabilization we studied in Chapter 2. However, the decay of $\Gamma(\alpha)$ accompanies oscillations.

Our laser pulse is not monochromatic but its envelope varies slowly as function of time; it contains $n_{oc} = 100$ periods of optical cycles. So, it is expected that the electron adiabatically follows the momentary Hamiltonian $H(\alpha)$, while the photoionization is taking place at each α according to Eq. (2.11). In the rising part of the pulse, $0 < t < T/2$, the function $E_0(\alpha) + \omega$ and $\Gamma(\alpha)$ start at $\alpha = 0$ and adiabatically evolves on the blue and red curves, respectively, until they reach $\alpha = 3.04$, corresponding to the maximum field amplitude of the laser field at $t = T/2$. In the falling part of the pulse, $T/2 < t < T$, this evolution is inversely repeated; They start at $\alpha = 3.04$, and traces

back to $\alpha = 0$ along the curves $E_0(\alpha) + \omega$ and $\Gamma(\alpha)$. Therefore, it is expected that the function $E_0(t) + \omega$ becomes bell-shaped, and $\Gamma(t)$ has four clearly separated humps since it exceeds the second critical value α_{c2} for the ionization suppression. According to this picture, the adiabatic approximation is implemented by substituting,

$$\alpha \quad \rightarrow \quad \alpha(t) = \frac{F_0}{\omega^2} f(t), \tag{5.8}$$

where the function $f(t)$ is the pulse envelope defined by Eq. (5.3). After this substitution, the functions $E_0(t) + \omega$ and $\Gamma(t)$ behave as shown in Fig. 5.3b. So, it is expected that the photoelectron wave packet of the same energy can be produced in the rising and falling part of the pulse, and their interference causes the oscillating substructures in the ATI peaks. Now we estimate interference fringes qualitatively in the same approximation. The probability for the electron to be found in the ground state at time t is

$$P_0(t) \approx \exp\left[-\int_0^t \Gamma(t')\, dt'\right]. \tag{5.9}$$

Let E be the energy of the photoelectron ionized at time t, then

$$E = E_0(t) + \omega. \tag{5.10}$$

The ionization yield from t to $t + dt$ is given by $P_0(t)\Gamma(t)dt$. This is equivalent to the photoelectron yield from E to $E + dE$, namely $C^2(E)|dE|$ where $C(E)$ is the amplitude of the photoelectron. Then we obtain

$$C(E) = \sqrt{P_0(t)\Gamma(t)\left|\frac{dt}{dE}\right|}\Bigg|_{t=t(E)}. \tag{5.11}$$

For the present pulse, the inverse function $t = t(E)$ is double valued. The photoelectron wave packet of the same energy is produced at $t_1(E) \in [0, T/2]$ and $t_2(E) \in [T/2, T]$, corresponding to the rising and falling part of the pulse, see Fig. 5.3b. In the rising part of the pulse, the first wave packet is produced at $t_1(E)$ and evolves until $t_2(E)$; the second wave packet is produced at $t_2(E)$ with an additional phase accumulated between $t_1(E)$ and $t_2(E)$ in the dressed potential. Let $\Phi(E)$ be the phase difference of these wave packets, the photoelectron spectrum can be written

$$P_{\mathrm{HFFT}}(E) = \left|C_1(E) + C_2(E)e^{i\Phi(E)}\right|^2, \tag{5.12}$$

where the phase difference $\Phi(E)$ is given by

$$\Phi(E) = E \times [t_2(E) - t_1(E)] - \int_{t_1(E)}^{t_2(E)} [E_0(t) + \omega]\, dt. \tag{5.13}$$

Here the first term in $\Phi(E)$ represents the phase of the photoelectron wave packet produced at $t = t_1(E)$. The second terms represents the phase of the photoelectron wave packet produced at $t = t_2(E)$. This adiabatic version of the HFFT nicely reproduces the TDSE calculation as shown in Fig. 5.2b. The larger bunch of the oscillating structure around $E = E_0(\alpha_{c1}) + \omega$ is due to the pair of the bigger humps of $\Gamma(t)$, meanwhile the smaller pair is responsible for the additional oscillating structure around $E = E_0(\alpha_{c2}) + \omega$. Some disagreement in the lower energy part is explained by the fact that the HFFT is valid for $\omega \gg |E_0|$ and $\alpha^2(t)\omega \gg 1$ [38]; the second condition is not satisfied in the beginning and ending part of the pulse. The sharp increase of the HFFT result at the vicinity of $\max[E_0(t)] + \omega$ is due to the divergence of dt/dE in Eq. (5.11). On the basis of the above discussions, the conditions for observing the oscillating substructure are

$$\omega \gg |E_0|, \tag{5.14a}$$

$$F_0/\omega^2 > \alpha_{c1}, \tag{5.14b}$$

$$\omega T \gg 1, \tag{5.14c}$$

and

$$\text{a reasonable value of } T. \tag{5.14d}$$

The conditions Eq. (5.14a) and (5.14b) are required to reach the stabilization regime where the pair of the photoelectron wave packets are produced. The condition Eq. (5.14c) is required for the validity of the adiabatic version of the HFFT. The last condition is required for obtaining a number of fringes with good contrast. Suppose T is too large, then most of the population gets lost during the first ionization event in the rising part of the pulse, hence being proportional to the surviving ground state amplitude, the photoelectron wave packet produced in the falling part of the pulse becomes very small. If T is too small, then the phase difference between the pair of the photoelectron wave packets becomes very small, and it results in few oscillations.

To summarize, it is shown that the oscillating substructure in the ATI peaks is the interference fringes of the photoelectron wave packets at the same energy produced in the rising and falling part of the pulse.

5.3 Three dimensional case

We extend our study to the 3D case. The 3D calculations give us two significant pieces of insight which cannot be obtained in the 1D calculations. First, we can clarify how the structures of the ATI peaks depend on the partial wave components and laser polarizations. Second, therefore it is not obvious whether the oscillating substructures emerges in the same way. Separate treatment of the 3D photoelectron spectrum is thus unavoidable for theoretical completeness. Indeed, the oscillating substructures do appear also in the 3D case, but it is not trivial to see whether the HFFT approximation with the simple interference picture of the pair of photoelectron wave packets can reconstruct the oscillating substructures and whether their structures have similar dependencies on the laser parameters. In the 3D calculations, we employ the one-electron model of the hydrogen negative ion modeled by

$$V(r) = -V_0 \exp(-r^2/r_0^2), \tag{5.15}$$

where $V_0 = 0.3831087$ and $r_0 = 2.5026$ [23]. This potential supports only one bound state with energy $E_0 = -0.0277510$. The components of the laser electric field $0 < t < T$ are represented by

$$F_x(t) = \varepsilon F_0 f(t) \sin \omega t, \tag{5.16a}$$

$$F_z(t) = F_0 f(t) \cos \omega t, \tag{5.16b}$$

where ε, F_0, ω, and T are the ellipticity, amplitude, frequency and the durations of the laser pulse. We employ the laser envelope modeled as

$$f(t) = \left(1 - \frac{n_{\rm oc}^2 - 4}{n_{\rm oc}^2 - 1} \cos^2 \frac{\pi t}{T}\right) \sin^2 \frac{\pi t}{T}, \tag{5.17}$$

where $n_{\rm oc} = \omega T/2\pi$ is the number of optical cycles in the pulse. Note that this has a different form than what we employed in the 1D case. The second term in the brackets is needed so that the classical trajectories satisfy the initial conditions, Eq. (4.52b). Let us define the reference laser pulse $F_0 = 0.5$ (8.8×10^{15}W/cm^2), $\omega = \pi/10$ (8.55 eV), and $T = 600$ (14.4 fs); hence $n_{\rm oc} = 30$. The photoelectron spectrum for the reference pulse with ellipticity $\varepsilon = 1$ is shown in Fig. 5.4. In this figure, each of the partial wave components $l = 0, \ldots, 5$ is obtained by summing over magnetic quantum numbers, and the total

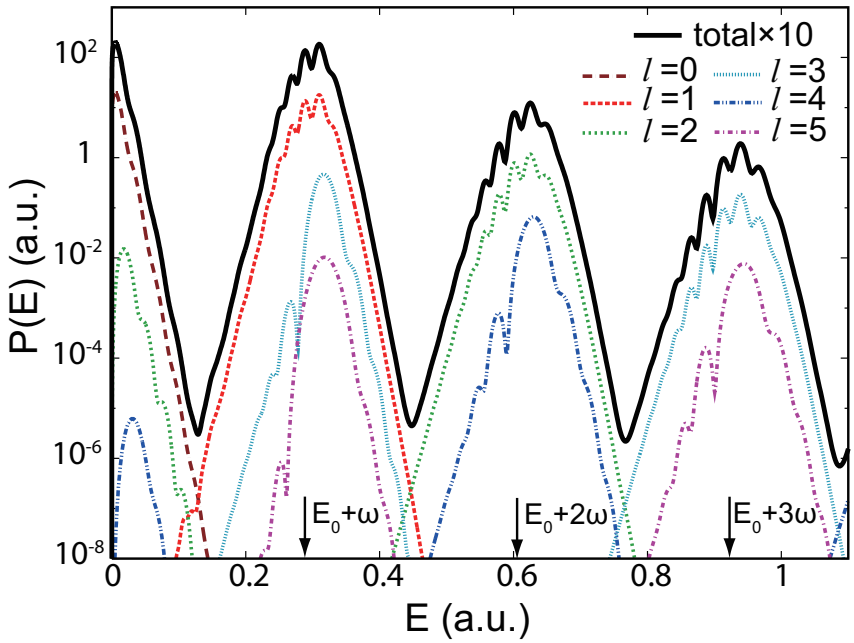

Figure 5.4: The partial wave and total photoelectron spectra for the reference laser pulse with $\varepsilon = 1$, $F_0 = 0.5$, $\omega = \pi/10$, and $T = 600$. The multiphoton absorption energies $E_0 + n\omega$ are shown by arrows. Note that the total spectrum is multiplied by 10 for the illustrative purpose.

yield is summed over the partial waves. One can clearly see a train of the ATI peaks located around the n-photon absorption energies $E_0+n\omega, n = 1, 2, \ldots$ with the dominant contribution coming from $l = n$. The peaks associated with n-photon absorption will be called the nth peak. One may consider that this is a trivial consequence of the perturbation theory. However, the total ionization rate is 0.972, so the situation is very far from the regime of the standard perturbation theory. One can also see a peak around the zero energy which is dominated by the partial wave $l = 0$; we call it the zeroth peak. The contribution of the zeroth peak to the total ionization probability is 0.263, so it represents a non-negligible feature. However, its origin stems from a quite different mechanism that which we discussed so far. Its physico-mathematical analysis is thus postponed till the next Chapter. The contributions of the higher partial waves to the total ionization probability are 0.637, 0.465×10^{-3}, 0.206×10^{-3}, 0.378×10^{-4} , and 0.378×10^{-4}, respectively for l from 1 to 5.

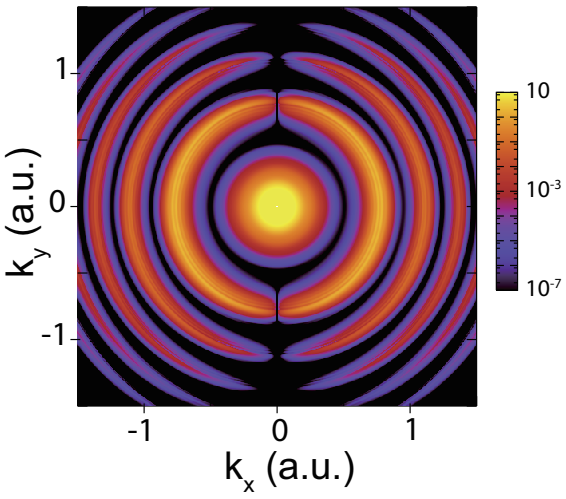

Figure 5.5: Momentum distribution of the photoelectron in the xy plane for the reference laser pulse with $\varepsilon = 1$.

5.3.1 Three dimensional momentum distribution

Fig. 5.5 shows a map of the 3D momentum distribution Eq. (4.86) of the photoelectron in the xy plane (perpendicular to the polarization plane xz) for the same pulse parameters as in Fig. 5.4. The bright disk at the center is the zeroth peak mentioned above. The series of bright rings correspond to the ATI peaks. In the present case of circular polarization, the momentum distribution looks axially symmetric about the y axis (the direction of propagation of the laser pulse), although this symmetry is not exact. In the linear polarization case, the distribution is exactly axially symmetric about the polarization axis [23]. The cut of ATI rings along the k_y axis $k_x = 0$ reflects their partial wave contents in terms of the magnetic quantum number. It is explained by the fact that the dominant contribution to the nth peak comes from the partial wave with $l = n$. This feature is in accordance with the absorption of n circularly polarized photons and again may seem to be a trivial consequence of the standard perturbation theory in the laboratory frame, although the situation is highly non-perturbative. In fact, we shall see below that the problem *can* be nevertheless treated perturbatively in the KH frame within the HFFT [38].

An oscillatory substructure in ATI peaks is clearly seen again in Fig. 5.4; it is also noticeable as circular ripples within ATI rings in Fig. 5.5. A similar oscillating

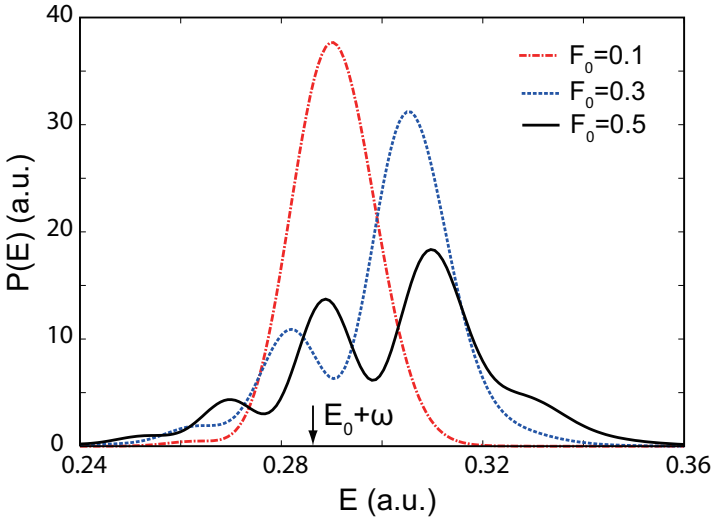

Figure 5.6: The first ATI peak for pulses with $\varepsilon = 1$, $\omega = \pi/10$, and $T = 600$ and three values of the field amplitude $F_0 = 0.1$, 0.3 and 0.5.

substructure is also found in the 3D calculations for linear polarization [23]. In the 1D case, it is clarified that the interference of the photoelectron wave packets produced at different moments in time causes the oscillating substructure. In the rest of this chapter, we discuss this substructure and clarify the underlying interference mechanism focusing on the first ATI peak in the 3D case. In doing so, we follow a train of thought similar to that in the 1D case, but deal with circular and elliptic polarizations to show that the effect is robust for any polarization and under variations of the laser parameters.

5.3.2 Dependence of the oscillating substructures on the laser parameters

We confirm that the criteria for the laser parameters found in the 1D case are similarly applicable to the 3D case for observing the oscillating substructures in the ATI peaks. To this end, we first clarify that the emergence of the oscillating substructure also requires the conditions Eq. (5.14), while there is no dependence on the polarization of the laser pulse. We then confirm by way of a numerical experiment in the next section that the origin of the oscillating substructures come from the interference of the photoelectron wave packets.

Since our laser pulses always satisfy the conditions Eq. (5.14a) and (5.14c), we

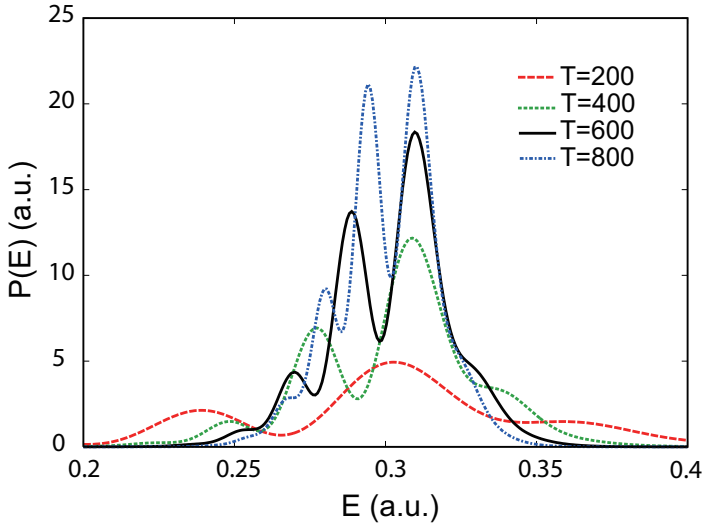

Figure 5.7: The first ATI peak for pulses with $\varepsilon = 1$, $F_0 = 0.5$, and $\omega = \pi/10$ and four values of the pulse duration $T = 200$, 400, 600 and $T = 800$.

focus on Eq. (5.14b) and (5.14d). First, we discuss the condition Eq. (5.14b). We consider circularly polarized pulses with $\omega = \pi/10$ and $T = 600$ and the different values of F_0, see Fig. 5.6. As can be seen from Fig. 5.6, for $F_0 = 0.1$ the first ATI peak has a simple bell-like shape centered near the one-photon absorption energy $E_0 + \omega$, as one would expect in the perturbation regime. For the present parameters $n_{\rm oc} = 30$, so the pulse is rather monochromatic. However, a pronounced oscillating substructure appears for larger values of F_0. The threshold value of the field amplitude for which this substructure becomes clearly visible is estimated to be $F_0 \approx 0.2$, which corresponds to $\alpha_c \approx 2$. This value is connected to the emergence of the stabilization. For $\alpha > \alpha_c$, the ionization rate has separated peaks, the oscillating substructures may be attributed to the interference of the photoelectron wave packets produced in the rising and falling part of the pulse.

Second, we discuss the condition Eq. (5.14c). We again consider circularly polarized pulses with $\omega = \pi/10$, with a fixed field amplitude $F_0 = 0.5$ and the different values of T, see Fig. 5.7. In these calculations $\alpha \approx 5.07$, which is definitely larger than α_c as estimated above. The interference substructure of the first ATI peak can be clearly seen in the figure. The frequency of the oscillations grows with T, because the phase difference is proportional to T as is shown below. However, the contrast of the fringes

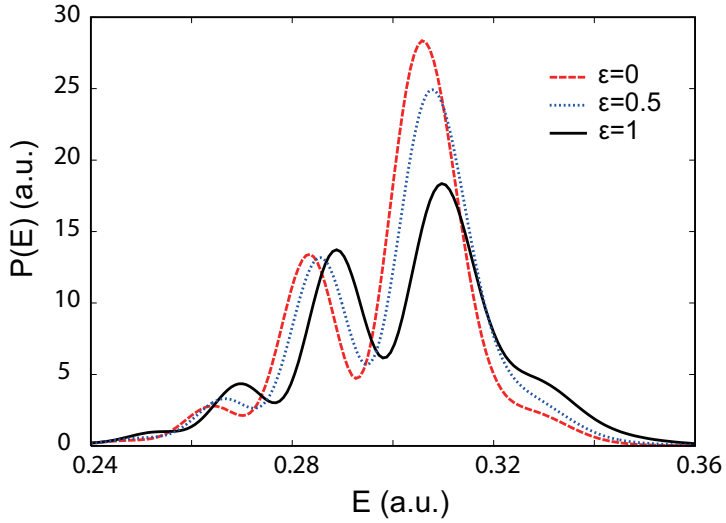

Figure 5.8: The first ATI peak for $F_0 = 0.5$, $\omega = \pi/10$, and $T = 600$ with linear ($\varepsilon = 0$), intermediate elliptic $\varepsilon = 0.5$, and circular $\varepsilon = 1$ polarizations.

deteriorates as T grows. Indeed, let $I_{\max}$ and $I_{\min}$ be the local maximum and local minimum values of $P(E)$ in one-cycle of the oscillation, and I be the contrast defined by $I = (I_{\max} - I_{\min})/(I_{\max} + I_{\min})$. Then the contrast values for $T = 200, 400, 600$, and 800 are approximately given by $I = 0.75, 0.62, 0.49$ and 0.38, respectively. This is explained as before by the fact that for a good contrast the two interfering wave packets must have comparable amplitudes. Meanwhile, if the pulses are too long, complete depletion of the initial state occurs in the rising part of the pulse, so the amplitude of the second wave packet becomes much smaller than that of the first one.

Finally, we discuss the dependence of the spectrum on the laser polarization. We consider pulses with $F_0 = 0.5$, $\omega = \pi/10$, and $T = 600$ for the polarization varying from linear $\varepsilon = 0$ to circular $\varepsilon = 1$, see Fig. 5.8. In all cases, a pronounced oscillating substructure can be clearly seen. We thus conclude that this substructure is robust for all possible polarizations. The variance of the position of the interference fringes is due to the difference of the corresponding classical trajectories.

Summarizing, we confirmed that the emergence of the oscillating substructure in the 3D case requires the conditions for the laser parameters Eq. (5.14) just as in the 1D case. The dependencies of the structures of the ATI peaks on the laser parameters are well described by the interference picture of the photoelectron wave packets.

5.3.3 Verification of the interference picture by a numerical experiment

In this section, we confirm more directly by a numerical experiment that the interference picture is responsible for the oscillating substructures in the ATI peaks.

Let us consider a laser pulse defined by [cf Eqs. (5.16)]

$$F_x(t) = \left(1 - [s(t - T/2)]^2\right) F_0 f(t) \cos \omega t, \tag{5.18a}$$

$$F_z(t) = s(t - T/2) F_0 f(t) \cos \omega t, \tag{5.18b}$$

where $f(t)$ is the envelope function (5.17) and $s(t)$ is the switching function which smoothly varies from 1 to 0 as t passes through zero in the positive direction,. The switching function $s(t)$ is given by

$$s(t) = \frac{1}{2}\left(1 - \tanh \frac{\omega}{2\pi} t\right) \tag{5.19}$$

The effect of introducing the switching function is to adiabatically rotate the polarization axis from z to x within a few laser cycles around the temporal center of the pulse $t = T/2$. The photoelectron wave packets created in the rising and falling part of the pulse in this case propagate in different directions, along the z and x axis, respectively. Hence they do not necessarily interfere and the oscillating substructure in the spectrum should be suppressed if their interference is *the* direct cause of the oscillating substructure. Fig. 5.9 compares the first ATI peak for linear polarization (LP), i.e. Eqs. (5.16) with $\varepsilon = 0$, and in the case where the polarization axis is adiabatically rotated (AR) in the manner of Eqs. (5.18). The laser parameters in these calculations are $F_0 = 0.5$, $\omega = \pi/10$, and $T = 600$. Indeed, one can see clear oscillations in the spectrum in the LP case, but none in the AR case. The AR spectrum reveals the true shape of each of the wave packets created and serves as a background for the oscillations in the LP spectrum. Thus by rotating the polarization axis at a time between the two humps of the ionization rate $\Gamma(t)$ one can control the interference substructure. Designing an ingenious experimental scheme for rotating the polarization axis within the duration of a pulse should be a challenge.

5.3.4 Analysis in terms of the high-frequency Floquet theory

Having established the fact that the observed oscillations in the spectrum result from an interference mechanism, here we reconstruct the first ATI peak using an adia-

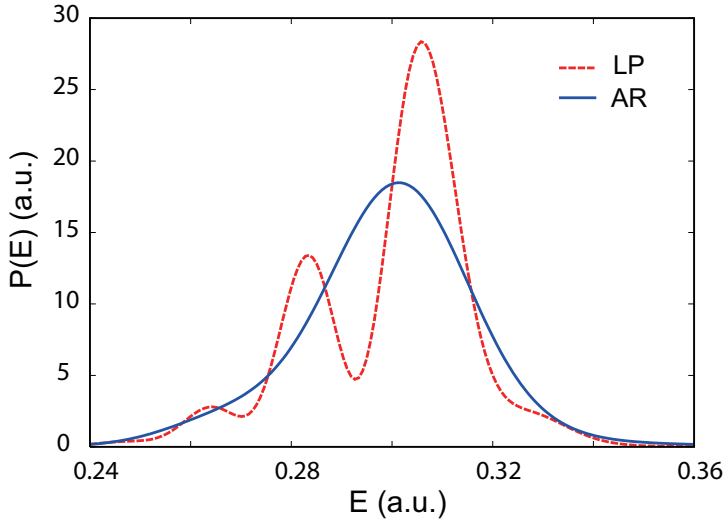

Figure 5.9: The first peak of the ATI spectrum for linear polarization (LP) along the z axis, and the case where the polarization axis adiabatically rotates from the z to x axis (AR). In the case of the AR, the photoelectron wave packet produced in the rising and falling part of the pulse propagate along the z and x direction. Hence the interference fringes is suppressed.

batic version of the HFFT [38] by including the polarization and the angular degrees of freedom. The present analysis thus generalizes that of the 1D [39] straightforwardly to the 3D case. We consider a circularly polarized pulse, $\varepsilon = 1$. It is convenient to rotate the coordinate axes with respect to what has been implied in the above discussion in such a way that the polarization plane coincides with the xy plane, thus the laser pulse propagates along the z axis.

Let us consider a monochromatic laser field, *i.e.*, temporarily omit the envelope factor $f(t)$ in Eqs. (5.16). The classical trajectory in this case is given by $\boldsymbol{\alpha}(t) = (\alpha\cos\omega t, \alpha\sin\omega t, 0)$, where $\alpha = F_0/\omega^2$ is the excursion amplitude of a free electron in the laser field. The KH potential can be expanded into a Fourier series,

$$V(|\mathbf{r}+\boldsymbol{\alpha}(t)|) = \sum_{n=-\infty}^{\infty} V_n(r,\theta;\alpha)e^{in(\varphi-\omega t)}, \tag{5.20a}$$

$$V_0(r,\theta;\alpha) = \frac{1}{T}\int_0^T V(\sqrt{r^2+2\alpha\sin\theta\cos\omega t+\alpha^2})dt, \tag{5.20b}$$

where θ and φ are the polar angles defining the direction of $\mathbf{r}$. In the zeroth order of the HFFT [38], the system is described by the stationary 'dressed' Hamiltonian

$$H_{\mathrm{HFFT}}(\alpha) = -\frac{1}{2}\frac{\partial^2}{\partial r^2} + \frac{\hat{l}^2}{2r^2} + V_0(r,\theta;\alpha), \tag{5.21}$$

where $\hat{l}^2$ is the square of the angular momentum operator. It can be seen that $V_0(r,\theta;0) = V(r)$, hence $H_{\mathrm{HFFT}}(\alpha)$ reduces to the unperturbed atomic Hamiltonian in the absence of the field. Let $\psi_0(r,\theta;\alpha)$ and $E_0(\alpha)$ denote the eigenfunction and eigenvalue, respectively, of the initial bound dressed state, which coincides with the ground state of the unperturbed atom for $\alpha = 0$. The partial wave expansion of the dressed ground state is

$$\psi_0(r,\theta;\alpha) = \sum_{l=0,2,\ldots} \phi_l(r;\alpha)\tilde{P}_l(\cos\theta), \tag{5.22}$$

where $\tilde{P}_l(\cos\theta)$ is the normalized Legendre polynomial, and the summation runs only over even l since the dressed potential $V_0(r,\theta;\alpha)$ is even function of $\cos\theta$. Our calculations show that even for the largest excursion amplitude considered here, $\alpha = 4$, the dressed binding potential $V_0(r,\theta;\alpha)$ approximately preserves spherical symmetry to a good approximation, *i.e*, it is sufficient to take only $l = 0$ and 2 in Eq. (5.22). The stationary Schrödinger equation for the dressed bound state reads,

$$\left[-\frac{1}{2}\frac{\partial^2}{\partial r^2} + \frac{\hat{l}^2}{2r^2} + U_{ll}(r;\alpha) - E\right]\phi_l(r;\alpha) + \sum_{l'\neq l} U_{ll'}(r;\alpha)\phi_l(r;\alpha) = 0, \tag{5.23}$$

where

$$U_{ll'}(r;\alpha) = \int_0^\pi \tilde{P}_l(\cos\theta)V_0(r,\theta;\alpha)\tilde{P}_{l'}(\cos\theta)\sin\theta d\theta. \tag{5.24}$$

The behavior of the eigenvalue $E_0(\alpha)$ is shown in Fig. 5.10a. The initial state remains bound in the interval of α shown in the figure, but the binding energy monotonically decreases as α grows, since the potential $V_0(r,\theta;\alpha)$ becomes shallower. Let $\psi(\mathbf{r},\mathbf{k};\alpha)$ be the scattering dressed state corresponding to the momentum $\mathbf{k} = (k,\Omega)$ and energy $k^2/2$, normalized to a unit amplitude of the incoming plane wave. Then, in the first order of the HFFT [38, 73], the partial width of the initial state associated with the absorption of one photon is given by

$$\Gamma(\alpha) = \frac{k(\alpha)}{(2\pi)^2}\int |A(k(\alpha),\Omega;\alpha)|^2\, d\Omega, \tag{5.25}$$

where $A(k,\Omega;\alpha)$ is the transition amplitude,

$$A(k,\Omega;\alpha) = \int \psi^*(\mathbf{r},\mathbf{k};\alpha)\, V_1(r,\theta;\alpha)e^{i\varphi}\,\psi_0(r,\theta;\alpha)\, d\mathbf{r}, \tag{5.26}$$

$k(\alpha)$ is the momentum of the photoelectron,

$$k(\alpha) = \sqrt{2(E_0(\alpha)+\omega)}, \tag{5.27}$$

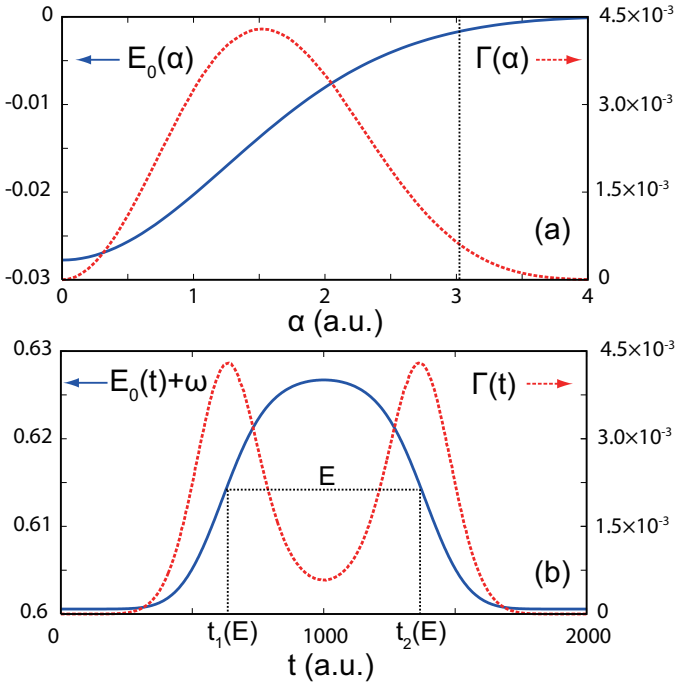

Figure 5.10: The energy and width of the initial atomic state "dressed" by the high-frequency laser field as functions of the amplitude α of classical trajectory and time t related to each other by Eq. (5.8) with $F_0/\omega^2 \approx 3$.

and $\psi(\mathbf{r}, \mathbf{k}; \alpha)$ is the scattering state of momenta k

$$\psi(\mathbf{r}, \mathbf{k}; \alpha) = 4\pi \sum_{lm} i^l \varphi_l(r, k(\alpha)) Y_{lm}(\theta, \phi) Y^*_{lm}(\hat{\mathbf{k}}). \tag{5.28}$$

Here $\varphi_l(r, k; \alpha)$ is the Siegert pseudostate expansion of the scattering state of angular momentum l, Eq. (3.42). We construct this term by retaining only the spherical term of the dressed potential $V_0(r, \theta; \alpha)$ in the Hamiltonian, Eq. (5.21). One can easily recognize in these formulas the first-order perturbation theory expressed by Eq. (5.26) for the dressed interaction potential $V_1(r, \theta; \alpha) e^{i(\varphi - \omega t)}$ in the basis of the dressed states. This is the applicability of the first order perturbation theory in the KH frame which we meant. In Eq. (5.26), it can be easily understood that only terms with $m = 1$ contribute to the integral in Eq. (5.26) according to the orthogonal relationship of the spherical harmonics $Y_{lm}(\theta, \varphi)$. The one-photon decay channel $V_1(r, \theta; \alpha)$ can be expanded into the normalized Legendre polynomial $\tilde{P}^n_l(\cos\theta)$,

$$V_1(r, \theta; \alpha) = \sum_{l=1,3,5,\ldots} v_{nl}(r; \alpha) P^n_l(\cos\theta), \tag{5.29}$$

where the summation runs over l in steps of 2, since the left-hand side in Eq. (5.20a) is an even function of $\cos\theta$. Our calculations show that in the expansion, (5.29), for $V_1(r,\theta;\alpha)$ the term with $l = 1$ dominates in the interval of α under consideration. This explains the results of the exact calculations discussed in Sec. 5.3: the dominant contribution to the first ATI peak comes from the partial wave with $l = 1$, see Fig. 5.4, the contribution from $l = 3$ is smaller by an order of magnitude. Hence to calculate $\Gamma(\alpha)$ it is sufficient to retain only the term with $(l, m) = (1, 1)$ in the expansion (5.28). The width $\Gamma(\alpha)$ calculated for $\omega = \pi/5$ is shown in Fig. 5.10a. It first grows with α, but then decays after α passes the critical value $\alpha_c \approx 1.5$. Such a behavior of $\Gamma(\alpha)$, which is a signature of stabilization, is a key for understanding the ionization dynamics. To close this discussion, we note that the dominance of the $l = 0$ and $l = 1$ components in the dressed binding $V_0(r,\theta;\alpha)$ and interaction $V_1(r,\theta;\alpha)$ potentials, respectively, means that the angular dependence of the transition amplitudes in the perturbation theory in terms of the HFFT is similar to that in the standard perturbation theory in the laboratory frame. However, the absolute values may be qualitatively different because of the effect of the dressing on the initial and final states and the transition operator, as can be seen from the very fact of non-monotonic behavior of $\Gamma(\alpha)$. The remaining part of the analysis parallels that in the 1D case. To provide a clear illustration of our point, let us consider a laser pulse with the parameters $F_0 = 1.2$, $\omega = \pi/5$, and $T = 2000$. The length of the pulse is increased in comparison to the previous cases, to have a pronounced interference substructure. The frequency is doubled, to keep a good contrast by reducing the decay rate. The field amplitude is increased accordingly to satisfy $\alpha > \alpha_c$. A part of the photoelectron spectrum near the first ATI peak ($E_0 + \omega \approx 0.601$) is extracted for this pulse as shown in Fig. 5.11. This pulse is not monochromatic with respect to ω. However, its envelope varies slowly, the pulse contains $n_{\rm oc} = 200$ optical cycles. So, the adiabatic approximation Eq. (5.8) employed in the 1D case can be also applied in this case. Repeating the train of thought from Eq. (5.8) to Eq. (5.13), we obtain the dressed ground state $E_0(t)$ and one-photon ionization rate $\Gamma(t)$ as functions of time as shown in Fig. 5.10b. The dressed ground state $E_0(t)$ is bell-shaped, while the one-photon ionization rate $\Gamma(t)$ has the clearly separated pair of humps. Hence, the adiabatic version of the HFFT confirms that the photoelectron wave

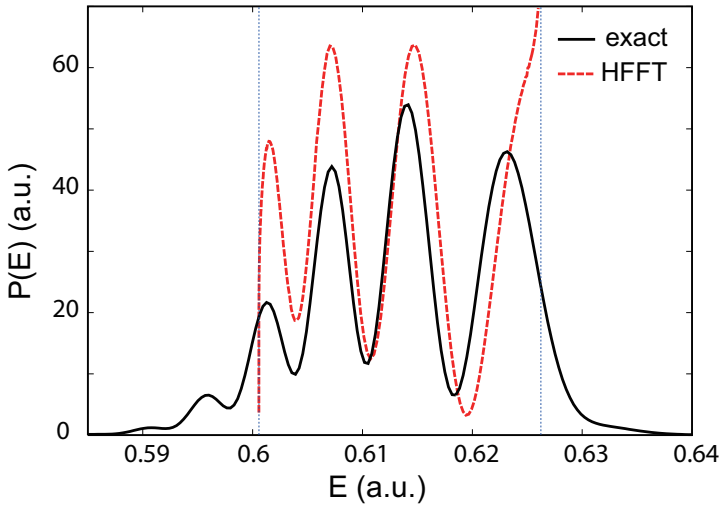

Figure 5.11: The first ATI peak for a circularly polarized laser pulse with $F_0 = 1.2$, $\omega = \pi/5$, and $T = 2000$. The solid and broken line in the figure represents the results by the TDSE and HFFT. This approximate theory yields the spectrum only in a limited energy interval from $\min[E_0(t) + \omega]$ to $\max[E_0(t) + \omega]$ shown in the figure by vertical dotted lines. Equation (5.12) diverges at the upper boundary of this interval because of the factor $dt(E)/dE$ in Eq. (5.11).

packets of the same energy are produced in the rising and falling part of the pulse. The oscillating substructure is nicely reproduced in terms of the interference between them as shown in red in Fig. 5.11. But the amplitude is somewhat overestimated, especially in the lower part of the spectrum. However, in spite of these limitations, it is clear that the theory correctly accounts for the mechanism responsible for the appearance of the interference substructure. This analysis confirms our qualitative interpretation of the dynamics. We point out that the interference fringes have been seen in X-ray range in a different context when the laser field is strong enough to drive Rabi oscillations between a bound and autoionizing state, see [36].

We close this chapter with an account of some experimental difficulties to observe the interference fringes discussed here. First, in experiments, ensemble of atoms subject to inhomogeneous intensity due to the spatial distribution of the laser intensity. Thus, it is expected that the volume integral of experimental results washes out the interference fringes. Second, our interference fringes discussed here requires the conditions Eq. (5.14). Thus it may be considered that X-ray free-electron laser (XFEL) is feasible to examine the interference fringes. However, XFELs currently available are produced using Self

Amplification of Spontaneous Emission (SASE) method, these are chaotic lights so that each pulse consists of a train of uncorrelated spikes. Thus it is speculated that the interference fringes are washed out when contributions of each spikes are added up.

Instead of XFELs, we propose to employ the Rydberg state of rare gas atom. Since ionization potential of Rydberg atoms are generally small, the high-frequency condition Eq. (5.14a) can be satisfied with wavelength in the visible range. Thus, the laser intensity for satisfying condition Eq. (5.14b) is expected to be relaxed. See Appendix A for more details.

Chapter 6

The slow electron peak

6.1 Introduction

In the previous chapter, we studied the oscillating substructures in the ATI peaks. However, in Fig. 5.4, one more prominent feature can be seen; the low energy peak near the origin, *i.e.* the bright disk at the center in Fig. 5.5. Let us call it the *slow electron peak* (SEP) on account of its small kinetic energy. This might appear counterintuitive since the photon energy is much larger than the binding energy of the electron. The origin of the SEP cannot be explained by the well-known ionization mechanisms *i.e.* multiphoton and tunneling processes. For instance the multiphoton ionization followed by the emission of the same number of photons might be considered. However, the contribution from this process should be negligibly small because the electron flies away immediately with large kinetic energy from the interaction region after the photon absorption so that interaction between core and electron vanishes. The tunneling ionization has nothing to do in the high-frequency regime. One may also consider that SEP results from the channel closing. But this is excluded since the ponderomotive energy for the ground state is expected to be almost the same as that for the threshold. Therefore we need to seek an alternative mechanism to account for the SEP. In the HFFT analysis of the previous chapter, we accounted for the adiabatic approximation including the slow time-dependence of the pulse envelope. Then the dressed Hamiltonian deforms slowly in time via the amplitude of the classical trajectory. As one follows the time variation, the slow deformation of the dressed potential promotes the dressed ground state to the dressed continuum through nonadiabatic transitions. Recently, Tolstikhin developed a theory for nonadiabatic transitions to the continuum in the case where the

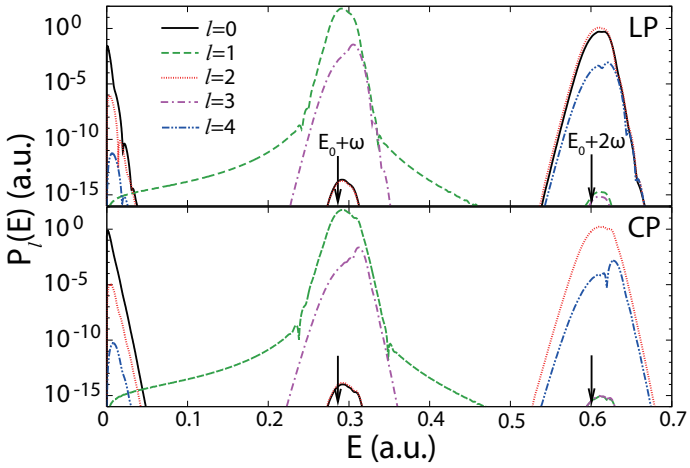

Figure 6.1: Partial-wave photoelectron spectrum of the 3D one-electron model of H^- for linearly (LP, $\varepsilon = 0$) and circularly (CP, $\varepsilon = 1$) polarized laser pulse with $F_0 = 0.3$, $\omega = \pi/10$, and $T = 2400$.

Hamiltonian of the system is a function of the "slow" time variable [24]. Employing this theory, in this chapter, we clarify the origin of the SEP and propose that the SEP is another pathway of ionization when the high-frequency intense laser pulse is applied to an atom.

In this Chapter, we employ the same model as in the 3D calculations in the previous chapter. The atomic potential is modeled by the Gaussian potential Eq. (5.15), and the profiles for the laser pulse are given in Eqs. (5.16) and Eq. (5.17). In what follows, we consider the photoelectron spectrum again concentrating on the SEP.

6.2 Photoelectron spectrum

The partial-wave photoelectron spectra are shown in Fig. 6.1 for the linearly (LP) and circularly (CP) polarized laser pulse . The laser parameters are $F_0 = 0.3$, $\omega = \pi/10$ and $T = 2400$ with $\varepsilon = 0$ and 1 for the LP and CP in Eqs. (5.16), respectively. The SEP can be found for both LP and CP cases. Therefore these results show that the SEP does not depend on the polarization of the laser pulse. Our calculations show that the SEP appears under the following conditions,

$$\omega \gg |E_0|, \quad \omega T \gg 1, \quad |E_0|T \gg 1. \tag{6.1}$$

The first one justifies the HFFT, and the second one allows us to adopt the adiabatic picture into the HFFT. The last condition provides us with the adiabatic approximation for transitions to the continuum. These conditions are different from those in Eq. (5.14) for the interference fringes in that the stabilization is not required and the longer pulse is feasible.

The SEP of our interest is brought about by relatively slow rise and fall of an experimentally feasible pulse satisfying Eq. (6.1). A pulse of contrasting character can also lead to generation of slow electron as a sudden projection onto the continuum [90]. Førre [89] points this out using a pulse with square-shaped envelope such that $|E_0|T = 0$. We set this issue aside here because the SEP we are considering is due to a much slower variation subject to the treatment in the next section.

6.3 Adiabatic version of the time-dependent Schrödinger equation

A natural framework for treating the regime defined by the first condition in (6.1) is the high-frequency Floquet theory [38]. For a monochromatic laser field, the KH potential can be expanded into a Fourier series,

$$V(|\mathbf{r} + \boldsymbol{\alpha}(t)|) = \sum_{n=-\infty}^{\infty} V_0(\mathbf{r};\alpha)e^{-in\omega t}. \tag{6.2}$$

In the leading order of the HFFT, we obtain

$$H_{\mathrm{HFFT}}(\alpha) = -\frac{1}{2}\Delta + V_0(\mathbf{r};\alpha), \tag{6.3}$$

where $V_0(\mathbf{r};\alpha)$ is the $n = 0$ term in Eq. (6.2). Our laser pulse is not monochromatic but the envelope contains $n_{\mathrm{oc}} = 120$ cycles. The second condition in Eq. (6.1) being well satisfied, we work with the adiabatic version of the HFFT as employed in Chapter 5. We implement the adiabatic approximation by substituting $\alpha_0 \to \alpha(t) = \alpha_0 f(t/T)$. As discussed in the introduction, multiphoton decay channels $V_n(\mathbf{r};\alpha)(n = 1, 2, \ldots)$ cannot account for the emergence of the SEP. Another path way of ionization is nonadiabatic transitions caused by deformation of the dressed potential $V_0(\mathbf{r};\alpha)$. Although the first two conditions of Eq. (6.1) suggest us that the dressed potential $V_0(\mathbf{r};\alpha)$ varies its shape adiabatically, the *finiteness of the pulse length* causes the nonadiabatic transitions. Neglecting all multiphoton processes, we thus arrive at the equation

$$i\,\frac{\partial\psi_0(\mathbf{r},t)}{\partial t} = \left[-\frac{1}{2}\Delta + V_0(\mathbf{r};\alpha(t))\right]\psi_0(\mathbf{r},t). \tag{6.4}$$

In contrast to Eq. (4.54), the Hamiltonian in Eq. (6.4) depends on time only via a slow time dependence of the envelope of the pulse; rapid oscillations of $\boldsymbol{\alpha}(t)$ at the laser frequency are averaged out by switching to the dressed potential. We shall call Eq. (6.4) the time-averaged TDSE. Equation (6.4) does not account for multiphoton processes, but we expect that it correctly describes the physics associated with the SEP. To confirm this, we compare spectra obtained by solving Eqs. (4.54) and (6.4). The mathematical step in going from Eq. (4.54) to Eq. (6.4) is justifiable by the first two conditions in (6.1), so these conditions must be examined. We consider the pulses of the same length $T = 2400$ as in Fig. 6.1. The spectra obtained from the full TDSE (4.54) depend on the field amplitude F and frequency ω separately, while those obtained from the time-averaged TDSE (6.4) depend only on their combination given by α_0. We solve Eqs. (4.54) for pulses with $F = n^2 F_0$ and $\omega = n\omega_0$, so the value of α_0 is kept fixed, where $F_0 = 0.3$ and $\omega_0 = \pi/10$, as in Fig. 6.1. As n grows, the frequency of the pulse grows, the spectra obtained from Eq. (4.54) are expected to converge to the one from Eq. (6.4). This is indeed the case, see Fig. 6.2. This holds for any polarization of the pulse. We thus conclude that the physical origin of the SEP can be sought on the basis of Eq. (6.4).

6.4 Adiabatic approximation for the transitions to the continuum

The third condition in (6.1) facilitates the analysis of Eq. (6.4). Under this condition, transitions caused by variations of the dressed potential can be treated in the adiabatic approximation. We are interested in transitions to the continuum. While nonadiabatic transitions between discrete states have been a subject of intensive studies [84], much less is known about nonadiabatic transitions between a discrete and continuum states. The problem was raised and solved for a certain situation in an early paper by Solov'ev [85], see also his review article [86]. More recently, the theory was rederived on completely different grounds [24], which confirmed the results of [85], but also provided a way to implement them in practical calculations. We shall use the formulation of [24]. A key object in this formulation is the Siegert state (SS) for the Hamiltonian in Eq. (6.4), the one which coincides with the initial bound state of the unperturbed atom for $\alpha(t) = 0$. We discuss the adiabatic approximation only for circular polarization

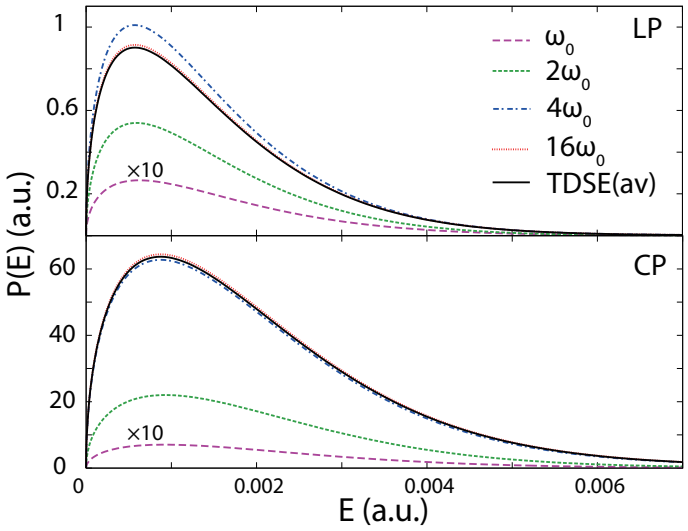

Figure 6.2: Broken curves: the full TDSE results, Eq. (4.49), for the slow electron peak produced by pulses with $F = n^2 F_0$, $\omega = n\omega_0$, and $T = 2400$, where $\omega_0 = \pi/10$, $F_0 = 0.3$, and the integer n varies from 1 to 16. The value of $\alpha_0 = 3.04$ for these pulses is kept fixed and equal to that in Fig. 6.1. Solid curves: the results obtained by solving the time-averaged TDSE (6.4). The total spectra for linear (LP) and circular (CP) polarizations are shown.

since this case permits us to calculate the dressed potential analytically for the present model. This potential is axially symmetric about the normal to the polarization plane. To construct the SS, we expand the wave function into partial waves with outgoing-wave boundary conditions imposed as in [30]. The details are given in Appendix H. Let $k_0(t)$ and $E_0(t) = k_0^2(t)/2$ denote the momentum and energy eigenvalues for the SS. We adopt $t = -T/2$ and $T/2$ as the starting and ending moment of the pulse. Then it holds $\alpha(\pm T/2) = 0$, hence $k_0(\pm T/2) = i\sqrt{-2E_0(\pm T/2)}$. As $\alpha(t)$ grows, the dressed potential $V_0(\mathbf{r}; \alpha(t))$ becomes shallower, and at some critical point $\alpha_c = \alpha(t_c)$ the bound state disappears, *i.e.*, $E_0(t_c) = 0$. The critical amplitude α_c depends on the number of partial waves incorporated into the eigenvalue equation. We obtain $\alpha_c = 4.16, 4.46$ and 4.48 for the total angular momenta $l = 0, 2$ and 4, respectively. Hence, the value of α_c rapidly converges as the number of partial waves increases. Thus we adopt $\alpha_c = 4.48$ for the present model. For the pulse parameters being employed to obtain the results shown in Figs. 6.1 and 6.2, $\max \alpha(t) = \alpha_0 = 3.04$. So the SS remains bound all during the application of the pulse, see Fig. 5.10a, and we stay on the real axis of time, which

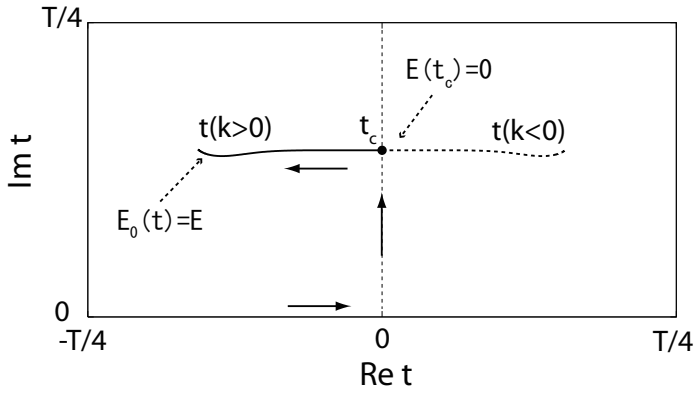

Figure 6.3: An example of the trajectory traced by the solution $t(k)$ to Eq. (6.5) in the complex t plane. The SS is promoted to the continuum at the critical point $t_c = t(0)$.

corresponds to the under barrier case in the classification of [24]. Its energy $E_0(t) < 0$ goes up while its momentum $k_0(t)$ goes down along the imaginary axis in the complex k plane on the rising part of the pulse $-T/2 < t < 0$, and reaches its maximum at $t = 0$. This evolution is repeated in the reverse order on the falling part of the pulse $0 < t < T/2$. In the adiabatic regime, transitions can efficiently occur only when the energies of the initial and final states coincide; transitions associated with a change in the energy of the system are suppressed. Thus the moment of ionization is defined by [24]

$$k_0(t) = k \quad \rightarrow \quad t = t(k), \tag{6.5}$$

where $E = k^2/2$ is the energy of the ionized electron. The procedure for constructing the line $t = t(k)$ is given in Appendix I. In the under barrier case, this equation does not have a solution on the real t axis. A solution can be found in the complex plane if, reaching the maximum of $E_0(t)$ at $t = 0$, one turns to the left and goes along the imaginary axis into the upper half of the complex t plane as shown by the solid arrows in Fig. 6.3. The value of $\alpha(t)$ is real and continues to grow along this path. The SS remains bound up to the point $t_c = t(0)$, where $k_0(t_c) = 0$. This signifies the entrance into the continuum. The solution $t(k)$ to Eq. (6.5) traces a trajectory in the complex t plane passing through t_c. Only a part of this trajectory corresponding to the positive values of k is needed to calculate the photoelectron spectrum in the adiabatic approximation

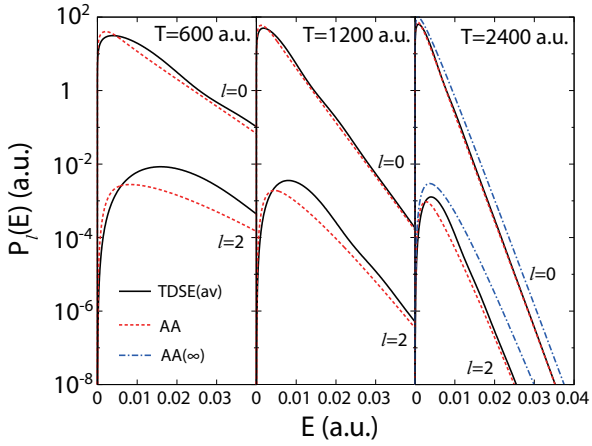

Figure 6.4: The partial-wave components of the slow electron peak produced by pulses with $\alpha_0 = 3.04$, as in Figs. 6.1 and 6.2. Solid curves: the exact results obtained from the time-averaged TDSE (6.4). Dashed curves: the adiabatic approximation, Eq. (6.6). Dash-dotted curves: the limiting form of the adiabatic approximation for $T \to \infty$, Eq. (6.8).

[24]. The partial wave spectrum is given by [24]

$$P_l(E) \approx e^{-2\mathrm{Im}S(t(k))} \left| \frac{dt(k)}{dk} \right| \left| \frac{\phi_0^{(l)}(a; t(k))}{ka\ h_l^{(1)}(ka)} \right|^2 , \tag{6.6}$$

where

$$S(t) = Et - \int_0^t E_0(t)dt. \tag{6.7}$$

See Appendix J for its derivation. Here $h_l^{(1)}(z)$ is the spherical Hankel function of the first kind. The radial functions $\phi_0^{(l)}(r; t)$ correspond to the partial-wave expansion of the SS eigenfunction. The radius a at which the outgoing-wave boundary condition is applied appears in Eq. (6.6), but the results become independent of its value as a exceeds the range of the dressed potential [24]. In Fig. 6.4, we compare the partial-wave photoelectron spectra obtained by solving Eq. (6.4) with those defined by Eq. (6.6) for three pulses of different lengths, *i.e.* $T = 600$, 1200, and 2400 for the same value of α_0 as in Figs. 6.1 and 6.2. The full width at half maximum for the present pulse envelope $f(\tau)$ is $T/3$, so the third condition in (6.1) can be specified more accurately as $|E_0|T/3 \gg 2\pi$. One can see that $T = 600$ is only the onset of the adiabatic regime. As T grows, the agreement between the exact spectra obtained from Eq. (6.4) and the adiabatic approximation (6.6) clearly improves. This argument suggests that Eq. (6.6) describes

the SEP reliably in the adiabatic regime. An advantage of having this approximation is that now we can extract the dependence of the SEP on the electron energy E and pulse length T analytically. In the ultimate adiabatic limit of $T \to \infty$, the width of the SEP tends to zero, so all the characteristics of the SS needed to implement Eq. (6.6) can be drawn by their values at $t = t_c$. We thus obtain

$$P_l(E) \approx A_l T k^{2l+1} e^{-BT-2|\tau_c TE}, \tag{6.8}$$

where the coefficients A_l, B, and $\tau_c = t_c/T$ depend on the atomic potential $V(r)$ and pulse envelope $f(\tau)$, but do not depend on E or T. They are given by

$$A_l = \frac{1}{k}\left|\frac{\phi_0^{(l)}(a;t_c)}{ka\ h_l^{(1)}(ka)}\right|^2, \tag{6.9}$$

$$B = -\frac{2}{T}\mathrm{Im}\int_0^{t_c} E_0(t)dt, \tag{6.10}$$

The spectra obtained from Eq. (6.8) for the longest pulse with $T = 2400$ are also shown in Fig. 6.4. Equation (6.8) is less accurate than Eq. (6.6), but is certainly correct qualitatively. One consequence of Eq. (6.8) is that the SEP has a very simple and typical energy dependence for the adiabatic regime [24, 87]. Another consequence is that the width of the SEP and the total yield of slow electrons scale with T as T^{-1} and $T^{-1/2}e^{-BT}$, respectively. The critical moment t_c appears in Eq. (6.8) and hence is an observable characteristic. The main dependence on the field amplitude is hidden in the value of t_c and is not that simple to extract.

In summary, we discussed the appearance of a *slow electron peak* in photoelectron spectra produced by a high-frequency laser pulse. The SEP is a robust feature and exists for any polarization of the laser field. It results from promotion of the atomic electron to the continuum via a *nonadiabatic transition* [24, 85] caused by slow deformation of the dressed potential that follows a variation of the envelope of the laser pulse. This ionization mechanism should reveal itself in all spectra produced by high-frequency pulses of finite length. The mechanism of the SEP is very similar to the "promotion mechanism" in the hidden crossing theory [91, 92, 93, 94]. Being a function of the pulse envelope, the *slow electron peak* could serve as a measure of the pulse length or intensity. The adiabatic version of the high-frequency Floquet theory [38], proposed in [39, 40] to explain the interference substructure of ATI peaks and applied in the present work to

explain the slow electron peak, seems to provide a useful framework for analyzing the photoionization dynamics in the high-frequency regime.

Chapter 7

Conclusions

In this thesis, we explored the photoelectron spectra of the one electron system in the stabilization regime. In so doing, we developed the powerful numerical methods. Our approach begins with the Siegert state (SS) expansion of a wave packet in the Kramers-Henneberger (KH) frame to accurately calculate the photoelectron spectrum in the stabilization regime. In the KH frame, the laser field is combined into the atomic potential via the classical trajectories of the free electron in the laser field. Then the effect of the laser field is represented by the quiver motion of the atomic potential along the classical trajectories. Thus the laser field is correctly taken into the time-dependent Schrödinger equation for the box size large enough to cover this oscillation. There are two advantages for the SSs as basis functions for the wave packet. First, unphysical reflection from the boundary of the box can be removed since the SS satisfies the outgoing wave boundary conditions. Second, the continuum state with arbitrary energy can be expanded by SSs exactly, allowing to obtain the photoelectron spectrum of a desired resolution. In consequence, our numerical scheme produces highly accurate photoelectron spectra.

We came to reveal the following noteworthy features in the photoelectron spectrum of the one-electron atomic system in the stabilization regime. In the 1D calculations, oscillating substructures in the above-threshold ionization (ATI) peaks were found for the intense high-frequency laser pulse. We developed the adiabatic version of the high-frequency Floquet theory (HFFT) to take into account the slowly varying envelope of the laser pulse. The HFFT analysis showed conclusively that this oscillating substructure is due to the interference of photoelectron wave packets produced in the rising and falling part of the pulse, and the stabilization plays a key role. The dimen-

sionality often plays a significant role so that what appears in 1D is not generated to occur in 3D. Carrying the 3D calculations, we confirmed the same type of oscillating substructures. Their dependency on the laser parameters were correctly explained by the interference picture developed in the 1D case, applying also a gedanken experiment based on the polarization of the pulse. The oscillating substructures were again reconstructed appropriately by the adiabatic HFFT attributing them to the interference of a pair of wave packets as in 1D.

In the photoelectron spectrum, we also found the emergence of the slow electron peak (SEP). The generation of the SEP might contradict intuition since the photon energy is much higher than the binding energy of the electron. It was shown that the origin of the SEP cannot be explained by the well-known ionization mechanisms: multiphoton and tunneling processes. The SEP is generated by the non-adiabatic transition to the continuum in the situation where the dressed potential is slowly varying in time. These features manifest themselves as general and robust structures in the photoelectron spectrum of the one-electron system.

Finally, we point out possibilities of experimental observations of our physical effects discussed in Chapters 5 and 6. In these Chapters, the employed laser parameters fall in X-ray range. Thus, it may be considered that our physical effect can be observed using X-ray free-electron lasers (XFELs). However, it seems to be difficult to observe our physical effects using XFELs due to the facts in the following. First, XFELs are produced using Self-Amplified Spontaneous Emission (SASE) method. SASE XFELs are chaotic lights so that each pulse consists of a train of uncorrelated spikes. Thus it can be speculated that the interference fringes can be washed out after adding up the contributions from each spike. Second, it may not be possible to observe our physical effects with the laser parameters being pursued currently in XFEL projects in the world. The only XFELs currently available exist at the Linac Coherent Light Source (LCLS) in US. In the LCLS, the photon energy, peak intensity, and duration of spikes in realistic AMO experiments in future are expected to be 800 to 2000 eV, $\approx 10^{18}$ W/cm^2, and a few fs long, respectively [95]. Using the photon energy $\hbar\omega = 800$ eV, peak laser intensity $I = 10^{18}$ W/cm^2, and pulse duration $T = 48$ fs for the parameters of the linearly polarized laser pulse, we calculated the photoelectron spectrum of one-electron

model of hydrogen negative ion Eq. (5.15) within the dipole approximation. However, both the yield of the first peak and slow electron are negligible since the total ionization probability is much less than 1%. The maximum excursion amplitude α of the classical trajectory is about 0.006 so that the situation is highly perturbative; the frequency is too high for α being comparable with the size of the system. Although we employed the laser parameters in X-ray range in this thesis, as pointed out in Chapter 1 and Appendix A, we propose employing a suitable Rydberg state of noble gas atoms of high angular momentum to open up experimental possibilities for verifying our physical effects with realistic laser parameters [6, 7, 8, 9, 10]. In such a system, the conditions Eq. (1.1) and Eq. (1.2) can be satisfied using the laser sources available in current experiments, and thus our physical effects in the stabilization regime should be accessible.

Bibliography

[1] M. Pont and M. Gavrila, Phys. Rev. Lett. **65**, 2362 (1990).

[2] Q. Su and J. H. Eberly, Phys. Rev. A **43**, 2474 (1991).

[3] K. C. Kulander, K. J. Schafer, and J. L. Krause, Phys. Rev. Lett. **66**, 2601 (1991).

[4] J. H. Eberly and K. C. Kulander, Science **262**, 1229 (1993)

[5] A. M. Popov, O. V. Tikhonova, and E. A. Volkova, J. Phys. B **36**, R125 (2003).

[6] R. J. Vos and M. Gavrila, Phys. Rev. Lett. **68**, 170 (1992).

[7] M. Pont and R. Shakeshaft, Phys. Rev. A **44**, 4410(R) (1991).

[8] M. P. de Boer, J. H. Hoogenraad, R. B. Vrigin, L. D. Noordram, and H. G. Muller, Phys. Rev. Lett. **71**, 3263 (1993).

[9] M. P. de Boer, J. H. Hoogenraad, R. B. Vrigin, R.C. Constantinescu, L. D. Noordram, and H. G. Muller, Phys. Rev. A **50**, 4085 (1994).

[10] N. J. van Druten, R.C. Constantinescu, J. M. Schins, H. Nieuwenhuize, and H. G. Muller, Phys. Rev. A **55**, 62 (1997).

[11] B. Piruax and R. M. Potvliege, Phys. Rev. A **57**, 5009 (1998).

[12] M. Boca, H. G. Muller, and M. Gavrila, J. Phys. B **37**, 147 (2004).

[13] M. Gavrila, J. Phys. B **35**, R147 (2002).

[14] K. C. Kulander, Phys. Rev. A , 35 (445).1987

[15] H. G. Muller, Laser Phys. **9**, 138 (1999)

[16] T. Morishita, Z. Chen, S. Watanabe, and C. D. Lin, Phys. Rev. A **75**, 023407 (2007).

[17] J. A. Pèrez-Hernàndez and L. Plaja, Phys. Rev. A **76**, 023829 (2007).

[18] V. C. Reed and K. Burnett, Phys. Rev. A , 43 (6217).1991

[19] H. A. Kramers, *Collected Scientific papers* (North-Holland, Amsterdam, 1956), p. 272.

[20] W. C. Henneberger, Phys. Rev. Lett. **21**, 838 (1968).

[21] O. I. Tolstikhin, Phys. Rev. A **73**, 062705 (2006).

[22] O. I. Tolstikhin, Phys. Rev. A **74**, 042719 (2006).

[23] O. I. Tolstikhin, Phys. Rev. A **77**, 032712 (2008).

[24] O. I. Tolstikhin, Phys. Rev. A **77**, 032711 (2008).

[25] A. J. F. Siegert, Phys. Rev. A **56**, 750 (1939).

[26] O. I. Tolstikhin, V. N. Ostrovsky, and H. Nakamura, Phys. Rev. Lett. **79**, 2026 (1997).

[27] O. I. Tolstikhin, V. N. Ostrovsky, and H. Nakamura, Phys. Rev. A **58**, 2077 (1998).

[28] G. V. Sitnikov and O. I. Tolstikhin, Phys. Rev. A **67**, 032714 (2003).

[29] K. Toyota, T. Morishita, and S. Watanabe, Phys. Rev. A **72**, 062718 (2005).

[30] P. A. Batishchev and O. I. Tolstikhin, Phys. Rev. A **75**, 062704 (2007).

[31] O. I. Tolstikhin, I. Yu. Tolstikhina, and C. Namba, Phys. Rev. A **60**, 4673 (1999).

[32] K. Toyota and S. Watanabe, Phys. Rev. A **68**, 062504 (2003).

[33] G. V. Sitnikov and O. I. Tolstikhin, Phys. Rev. A **71**, 022708 (2005).

[34] S. Yoshida, S. Watanabe, C. O. Reinhold, and J. Burgdörfer, Phys. Rev. A **60**, 1113 (1999).

[35] S. Tanabe, S. Watanabe, N. Sato, M. Matsuzawa, S. Yoshida, C. O. Reinhold, and J. Burgdörfer, Phys. Rev. A **63**, 052721 (2001).

[36] R. Santra, J. M. Shainline, and C. H. Greene, Phys. Rev. A **71**, 032703 (2005).

[37] G. García-Calderón, J. L. Mateos, and M. Moshinsky, Phys. Rev. Lett. **74**, 337 (1995).

[38] M. Gavrila and J. Z. Kaminski, Phys. Rev. Lett. **52**, 613 (1984).

[39] K. Toyota, O. I. Tolstikhin, T. Morishita, and S. Watanabe, Phys. Rev. A **76**, 043418 (2007).

[40] K. Toyota, O. I. Tolstikhin, T. Morishita, and S. Watanabe, Phys. Rev. A **78**, 033432 (2008).

[41] N. Rohringer and R. Santra, Phys. Rev. A **77**, 053404 (2008).

[42] K. Rzążwski, J. Zakrzewski, M. Lewenstein, and J. W. Haus, Phys. Rev. A **31**, 2995 (1985).

[43] M. Lewenstein, J. Zakrzewski, and K. Rzążwski, J. Opt. Soc. Am. B**3**, 22 (1986).

[44] E. J. Robinson, J. Phys. B **19**, L657 (1986).

[45] K. Toyota, O. I. Tolstikhin, T. Morishita, and S. Watanabe, Phys. Rev. Lett. **103**, 153003 (2009).

[46] M. Ferray, A. L'Huillier, X. Fi, L. A. Lompre, G. Mainfray, and C. Manus, J. Phys. B **21**, L31 (1988).

[47] P. B. Corkum, Phys. Rev. Lett. **71**, 1994 (1993).

[48] M. Lewenstein, Ph. Balcou, M. Yu. Ivanov, A. L'Huillier, and P. B. Corkum Phys. Rev. A **49**, 2117 (1994).

[49] H. Mashiko, A. Suda, and K. Midorikawa, Opt. Lett.**29**, 1927 (2004).

[50] P. Arpin, T. Popmintchev, N .L. Wagner, A. L. Lytle, O. Cohen, H. C. Kapteyn, and M. M. Murnane, Phys. Rev. Lett. **103**, 143901 (2009).

[51] C. Vozzi, F. Calegari, F. Frassetto, L. Poletto, G. Sansone, P. Villoresi, M. Nisoli, S. De Silvestri, and S. Stagira, Phys. Rev. A **79**, 033842 (2009).

[52] Y. Fu, H. Xiong, H. Xu, J.yao, Y. Yu, B. Zeng, W. Chu, X.Liu, J. Chen, Y. Cheng, and Z. Xu, Phys. Rev. A **79**, 013802 (2009).

[53] J. M. Madey, J. Appl. Phys. **42**, 1906, (1971).

[54] N. Rohringer and R. Santra, Phys. Rev. A **76**, 033416 (2007).

[55] R. Santra, N. V. Kryzhevoi, and L. S. Cederbaum, Phys. Rev. Lett. **103**, 013002 (2009).

[56] H. R. Varma, M. F. Ciappina, N. ROhringer, and R. Santra, Phys. Rev. A **80**, 053424 (2009).

[57] Y. Nabekawa, H. Hasegawa, E. J. Takahashi, and K Midorikawa, Phys. Rev. Lett. **94**, 043001 (2005).

[58] T. Okino, K. Yamanouchi, T. Shimizu, K. Furusawa, H. Hasegawa, Y. Nabekawa, and K. Midorikawa Chem. Phys. Lett. **432**, 68 (2006).

[59] T. Sato, T. Okino, K. Yamanouchi, A. Yagishita, F. Kannari, K. Yamakawa, K. Midorikawa, H. Nakano, M. Yabashi, M. Nagasono, and T. Ishikawa, Appl. Phys. Lett. **92**, 154104 (2008).

[60] Y. H. Jiang, A. Rudenko, M. Kurka, K. U. K̈hnel, Th. Ergler, L. Foucar, M. Schöffler, T. Havermeier, M. Smolarski, K. Cole, R. Dörner, S. Düsterer, R. Treusch, M. Gensch, C. D. Schröter, R. Moshammer, and J. Ullrich, Phys. Rev. Lett. **102**, 123002 (2009).

[61] A. A. Sorokin, M. Wellhöfer, S. V. Bobashe, K. Tiedtke, and M. Richter, Phys. Rev. A **75**, 051502(R) (2007).

[62] M. Martins, M. Wellhöfer, A. A. Sorokin, M. Richter, K. Tiedtke, and W. Wurth, Phys. Rev. A **80**, 023411 (2009).

[63] A. Rudenko, L. Foucar, M. Kurka, Th. Ergler, K.U. Kühnel, Y. H. Jiang, A. Voitkiv, B. Najjari, A. Kheifets, S. Lüdemann, T. Havermeier, M. Smolarski, S. Schössler, K. Cole, M. Schöffler, R. Dörner, S. Düsterer, W. Li, B. Keitel, R. Treusch, M. Gensch, C. D. Schröter, R. Moshammer, and J. Ullrich, Phys. Rev. Lett. **101**, 073003 (2008).

[64] M. Richter, M. Ya. Amusia, S. V. Bobashev, T. Feigl, P. N. Juranić, M. Martins, A. A. Sorokin, and K. Tiedtke, Phys. Rev. Lett. **102**, 163002 (2009).

[65] A. A. Sorokin, S. V. Bobashev, T. Feigl, K. Tiedtke, H. Wabnitz, and M. Richter, Phys. Rev. Lett. **99**, 213002 (2007).

[66] C. Bostedt, H. Thomas, M. Hoener, E. Eremina, T. Fennel, K.-H. Meiwes-Broer, H. Wabnitz, M. Kuhlmann, E. Plönjes, K. Tiedtke, R. Treusch, J. Fledhaus, A. R. B. de Castro, and T. Möller, Phys. Rev. Lett. **100**, 133401 (2008).

[67] M. Pont, N. R. Walet, M. Gavlira, and C. W. McCurdy, Phys. Rev. Lett. **61**, 939 (1988).

[68] R. M. Potvliege and P. H. G. Smith, Phys. Rev. A **48**, 46 (1993)..

[69] B. I. Schneider, Phys. Rev. A **24**, 1 (1981).

[70] J. C. Light, I. P. Hamilton, and J. V. Lill, J.Chem. Phys. **82**, 1400 (1985).

[71] J. I. Gersten and M. H. Mittleman, J. Phys. B **9**, 2561 (1976).

[72] R. Bhatt, B. Piraux and K. Burnett, Phys. Rev. A **37**, 98 (1988).

[73] M. Marinescu, and M. Gavrila, Phys. Rev. A **53**, 2513 (1996).

[74] G. Yao and S. I. Chu, Phys. Rev. A **45**, 6735 (1992).

[75] L. You, J. Mostowski, and J. Cooper, Phys. Rev. A **45**, 3203 (1992).

[76] D. Barash, A. E. Orel, and R. Baer, Phys. Rev. A **61**, 013402 (1999).

[77] E. Grosswald, *Bessel Polynomials Lecture Notes in Mathematics*, Vol. 698 Springer-Verlag, New York, 1978.

[78] W. H. Press, S. A. Teukosky, W. T. Vetterling, and B. P. Flannery, *Numerical Recipes in FORTRAN* (Cambidge University Press, Cambridge , 1992).

[79] J. R. Hellums and W. R. Frensley, Phys. Rev. A **49**, 2904 (1994).

[80] A. Arnold, VLSI Des. **6**, 313 (1998).

[81] M. Ehrhardt, and A. Arnold, Riv. Mar. Univ. Prama, 6/4, 57 (2001).

[82] A. Arnold, Transp. Theory Stat. Phys., 30/4-6, 561 (2001).

[83] P. Agostini, F. Fabre, G. Mainfray, G. Petite, and N. K. Rahman, Phys. Rev. Lett. **42**, 1127 (1979).

[84] H. Nakamura, *Nonadiabatic transition: Concepts, Basic Theories, and Applications* (World Scientific, Singapore, 2002).

[85] E. A. Solov'ev. Zh. Eksp. Teor. Fiz. **70**, 872 (1976) [Sov. Phys. JETP **43**, 453 (1976)].

[86] E. A. Solov'ev, J. Phys. B **38**, r153 (2005).

[87] Yu. N. Demkov and V. N. Ostrovski, *Zero-range Potentials and Their Applications in Atomic Physics* (Plenum Press, New York, 1988)

[88] *Handbook of Mathematical Functions*, edited by M. Abramowitz and I. A. Stegun (Dover, New York, 1972).

[89] M. Førre, S. Selstø, J. P. Hansen, and L. B. Madsen, Phys. Rev. Lett. **95**, 043601 (2005).

[90] After the publication of [45], Prof. Madsen at University of Aarhus drew our attention to [89]. In this paper, the emergence of the SEP by a high-frequency intense laser pulse was reported. Prof. Tolstikhin pointed out in the communication that this is due to the sudden change of the unperturbed atomic (dressed) potential into the dressed (unperturbed atomic) potential in the rising (falling) edge of the square envelope pulse.

[91] E. A. Solov'ev, Sov. Phys. JETP **54**, 5 (1981)

[92] S. Y. Ovchinnikov and E. A. Solov'ev, Sov. Phys. JETP **63**, 3 (1986)

[93] S. Y. Ovchinnikov and E. A. Solov'ev, Sov. Phys. JETP **64**, 2 (1986)

[94] S. Y. Ovchinnikov, Phys. Rev. A **42**, 3865 (1990).

[95] Private communications with Prof. Robin Santra at Argonne National Laboratory in US.

Appendix A

Experiments of the stabilization

Here we summarize the experimental results in [8, 9, 10]. In these papers, they employed a Rydberg state of the Ne atom, namely $(2p)^5 5g$ (m=4). They pointed out some advantages for the use of the Rydberg atom. First, the ionization potential for the Rydberg state being very small, it becomes relatively easy to satisfy the high-frequency condition Eq. (1.1), using lower frequency photon available in experiments. Second, the high angular momentum prevents the Rydberg electron to penetrate into the vicinity of the atomic core so that the binding energy is rather small. The photoionization cross section is thus expected to be small due to the weak interaction between the Rydberg electron and the parent core. Hence, the laser amplitude for α to exceed the critical value α_c is also expected to be small. Finally, the life time is of the order of hundreds of femto seconds. Then the required duration of a laser pulse is experimentally achievable, making it possible to prevent the electron from completely depleted before the laser pulse reaches its peak intensity. For instance, in [68], the life time of the 5g state of the H atom subject to the laser pulse of photon wavelength 620 nm was estimated as a function of the laser intensity, and its shortest value of the life time was shown to be 571 fs at the intensity 5.5×10^{13} W/cm^2.

Let us show in Fig. A.1A the experimental scheme employed in [10]. The Rydberg state of Ne $(2p)^5 5g$ with magnetic quantum number $m = 4$ was prepared by five-photon absorption by a circularly polarized UV laser pulse of $\lambda = 286$ nm. During the time interval of $\tau_d = 20$ ps before the second pulse, the external magnetic field of 0.9T is applied to make the angular momentum vector of the 5g state precessing around the magnetic field axis , *i.e.* the Lamor precession. This precession is exploited for aligning the $5g$ state with $m = 4$ along the polarization vecor of the main pulse. Next, the

second linearly polarized red laser pulse of $\lambda = 620$ nm (2.0 eV) and pulse duration $\tau = 90$ fs was irradiated to observe the yield of the ionized electrons as a function of the laser intensity. The photon energy 2.0 eV is much larger than the ionization potential $I_{\rm p} = 0.544$ eV for the 5g electron; the pulse duration 90 fs is much shorter than the minimum life time mentioned above. On account of the selection rule $\Delta m = 0$ for absorption of the linearly polarized light, 5g state with $m = 4$ does not couple to the lower-lying state. In [10], they observed that the yield of the photoelectron decreased for the intensity larger than 60 TW/cm^2, thus it strongly deviates from the golden rule as in Fig. A.1B. They applied yet another laser pulse of a weak intensity but of a long duration and examined the population of the Rydberg states that survived the second red laser pulse. This yield saturated for the intensity above $I \approx 60$ TW/cm^2. This is interpreted that the 5g state remained undepleted, that is ionization was ineffective. They concluded that this was a signature of the stabilization.

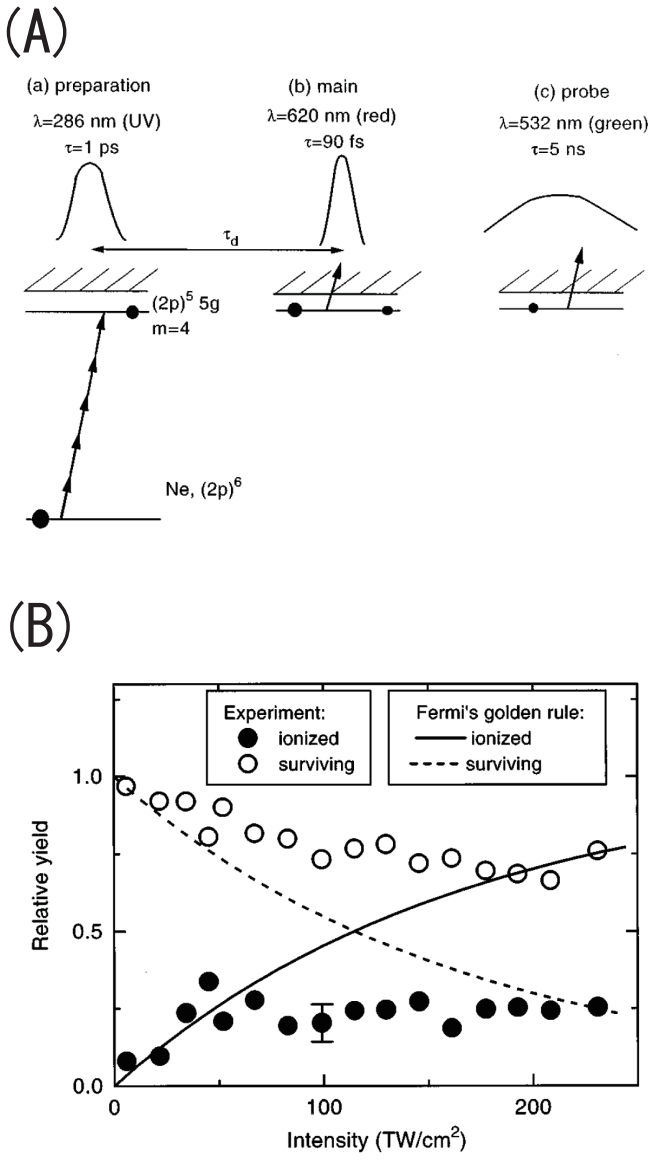

Figure A.1: Figures from van Druten *et al.* [10]. (A) Schematic diagram of the experiment. (a) The first preparation pulse pump the ground state of the Ne atom $(2p)^6$ to the Rydberg state $(2p)^5 5g$ (m=5) where m denotes the magnetic quantum number. (b) The main pulse is irradiated to photoionize the electron. On account of the small ionization potential $I_p = 0.544$ eV of the 5g electron, the laser pulse of the wavelength 620 nm, corresponding to the photon energy 2 eV, is enough to satisfy the high-frequency condition. (c) The survived population after the main pulse is measured by the probe pulse. (B) Experimental results. The black and represents the photoelectron yield by the main pulse as a function of the intensity of the main pulse; The white circle represents the surviving population of the 5g state as function of the intensity of the main pulse, measured by the probe pulse. The solid and broken line denote the photoelectron yield and the surviving population obtained from the Fermi's Golden rule. One can see that the experimental results show the strong deviations from the Fermi's Golden rule.

Appendix B

Brief summary of the historical development of the Siegert state

The development of the SS has a long history. In 1939, Siegert pointed out that the cross section in nuclear reactions becomes singular when the wave function satisfies the outgoing wave boundary condition [25]. This led Siegert to define the resonance state as the solution of the Schrödinger equation

$$\left[-\frac{1}{2}\frac{d^2}{dr^2} + V(r)\right]\phi(r) = 0, \tag{B.1}$$

with the boundary conditions

$$\phi(0) = 0, \left(\frac{d}{dr} - ik\right)\phi(r)\Big|_{r=r_0} = 0, \tag{B.2}$$

where the atomic potential $V(r)$ is assumed to vanish for $r > r_0$. The outgoing wave boundary condition destroys the hermiticity of the Hamiltonian, the eigenenergy becomes generally complex valued,

$$E = \frac{1}{2}k_n^2 = E_{\rm res} - i\Gamma/2. \tag{B.3}$$

In [25], Siegert showed that $E_{\rm res}$ and Γ emerge as the resonance energy and width in the cross section; they are the characteristic parameters for identifying a resonance. The resonant state belongs to the set of the outgoing states with a small imaginary part, *i.e.* $|E_{\rm res}| \gg \Gamma$. Therefore, the SS provides us with a powerful framework for the scattering theory, but to the contrary it remained to be regarded as a mere formal object for a long time due to the lack of an appropriate numerical scheme for generating the SSs systematically. The Siegert eigenvalue problem Eq. (B.1) subject to Eq. (B.2) is quadratic with respect to k. Therefore, eigenvalues used to be calculated individually using iterative procedures [69]. Additionally, SSs have unusual orthogonal and completeness relations. These prevented the development of the theory from reaching practical level.

However, Tolstikhin made a major breakthrough in 1997 by introducing the *Siegert pseudostate* (SPS) [26]. His is the finite basis representation of the SS for a cut-off potential. He reconstructed the theory of the SS in terms of SPS, and showed that the theory of the SPS coincide with that of the SS in the limit of $N \to \infty$ and $r_0 \to \infty$, where N is the number of basis functions [27]. And he showed that the quadratic eigenvalue problem can be recast into a linear one by doubling the dimension of the original Hilbert space. Hence, a set of SPSs can be obtained by diagonalizing a single matrix, making it suitable for practical calculations.

The theory of the SPS is further being developed. Sitnikov and Tolstikhin [28] developed the two-channel case for s-wave , Toyota *et al.* supplemented the perturbation theory of the SPS for one- and two-threshold cases [29] for s-wave, and Batischev and Tolstikhin extended the 1D one-channel case to 3D one-channel case that is for non-zero values of an angular momentum [30]. Recently, the theory is being developed to utilize the SPS as basis functions for a wave packet in order to solve the time-dependent Schrödinger equation. The idea is that unphysical reflection from the boundary can be removed by explicitly imposing the boundary condition Eq. (B.2). This is firstly pioneered by Yoshida *et al.* [34], and Tanabe *et al.* [35]. Later, Santra *et al.* developed a rigorous theory for the stationary Hamiltonian, and Tolstikhin further developed it for the time-dependant Hamiltonian [21, 22, 23, 24]. These developments have stimulated numerous applications in atomic physics for both time-independent and time-dependent frame works [31, 32, 33, 34, 35, 36, 37, 21, 22, 24, 23, 39, 40, 45].

Appendix C

Siegert boundary condition for non-zero values of the angular momentum

Here we discuss the outgoing wave boundary conditions for the case of non-zero values of the angular momentum. Since the centrifugal potential does not vanish beyond the finite cut-off radius, some modifications are needed for the outgoing wave boundary condition. In the outer region $r > a$, where the atomic potential vanishes, the Hankel function of the first and second kind, $h^{(1)}(kr)$ and $h^{(2)}(kr)$, respectively, are the independent solutions for the atomic Hamiltonian Eq. (4.59a). They are defined by

$$h_l^{(1)}(kr) = j_l(kr) + in_l(kr), \tag{C.1a}$$

$$h_l^{(2)}(kr) = j_l(kr) - in_l(kr), \tag{C.1b}$$

where $j_l(kr)$ and $n_l(kr)$ are the spherical Bessel function and spherical Neumann function, respectively. Their asymptotic behavior is represented by

$$h_l^{(1)}(kr)\Big|_{r\to\infty} = \frac{(-i)^{l+1}}{kr} e^{ikr}, \tag{C.2a}$$

$$h_l^{(2)}(kr)\Big|_{r\to\infty} = \frac{i^{l+1}}{kr} e^{-ikr}. \tag{C.2b}$$

So, let us define a new function $e_l(kr)$

$$e_l(kr) = i^{l+1} kr\ h_l^{(1)}(kr), \tag{C.3a}$$

$$e_l(kr)|_{r\to\infty} = e^{ikr}. \tag{C.3b}$$

So, we connect the internal wave function with the above external function $e_l(kr)$ at $r = a$. We need a derivative of this function to construct the outgoing wave boundary condition. To this end, let us consider the Bessel polynomial $y_l(kr)$ of order l [88],

$$y_l(kr) = \sum_{m=0}^{l} \frac{(l+m)!}{m!(l-m)!} \frac{(kr)^m}{2^m}. \tag{C.4}$$

Then the reverse Bessel polynomial is given by

$$\theta_l(kr) = (kr)^l y_l\left(\frac{1}{kr}\right) = \sum_{m=0}^{l} \frac{(2l-m)!}{m!(l-m)!}\frac{(kr)^m}{2^{l-m}}. \tag{C.5}$$

The coefficients of z^n in the reverse Bessel polynomial appears in the reverse order of the Bessel polynomial. For instance,

$$y_2(z) = 1 + 3z + 3z^2, \tag{C.6a}$$

$$\theta_2(z) = 3 + 3z + z^2. \tag{C.6b}$$

The series representation of the spherical Hankel function of first kind $h_l^{(1)}(z)$ is given by [88],

$$h_l^{(1)}(z) = i^{-n-1}z^{-1}e^{iz}\sum_{k=0}^{n}\frac{(n+k)!}{k!\Gamma(n-k+1)}(-2iz)^{-k}, \tag{C.7}$$

where $\Gamma(z)$ is the Gamma function. Using Eq. (C.7), one finds

$$h_l^{(1)}(kr) = -ie^{ikr}(kr)^{-l-1}\theta_l(-ikr). \tag{C.8}$$

Using Eq. (C.8), equation (C.3a) can be recast into

$$e_l(kr) = \frac{\theta_l(-ikr)}{(-ikr)^l}e^{ikr}. \tag{C.9}$$

Let z_{lp} $(z = 1, \ldots, l)$ be the zeros of the $\theta_l(-ikr)$. Then

$$\theta_l(-ikr) = \prod_{p=1}^{l}(-ikr - z_{lp}). \tag{C.10}$$

Using this formula, the derivative of $e_l(kr)$ is

$$\left(\frac{d}{dr} - ik + \frac{1}{r}\sum_{p=1}^{l}\frac{z_{lp}}{ikr + z_{lp}}\right)e_l(kr) = 0. \tag{C.11}$$

This is the outgoing wave boundary condition in the 3D case.

Appendix D

Siegert state expansion of the scattering state and the Green's function

D.1 One-dimensional case

D.1.1 Siegert state expansion of the scattering state

The scattering state can also be expanded by the SSs. Let $\phi^{\rm in}_{\pm}(x,k)$, $0<k<\infty$, be the solutions for Eq. (3.5) satisfying the boundary conditions,

$$\varphi^{\rm in}_{-}(x,k)=\begin{cases} e^{ikx}-r_{-}(k)e^{-ikx}, & x<x_{-}, \\ t(k)e^{ikx}, & x>x_{+}, \end{cases} \tag{D.1a}$$

$$\varphi^{\rm in}_{+}(x,k)=\begin{cases} t(k)e^{-ikx}, & x\le x_{-}, \\ e^{-ikx}-r_{+}(k)e^{ikx}, & x\ge x_{+}, \end{cases} \tag{D.1b}$$

where $r_{\pm}(k)$ and $t(k)$ are the reflection and transmission amplitudes; for symmetric atomic potentials, $r_{+}(k)=r_{-}(k)$. The wave packet formed by the superposition of $\varphi^{\rm in}_{\pm}(x,k)$ for a narrow interval of k represents the *in* state, which it approaches the interaction region $x_{-}<x<x_{+}$ in the remote past from the left and right, respectively. To define the photoelectron spectra, we need *out* states $\varphi^{\rm out}_{\pm}$; the wave packet formed by them recede from the interaction region in remote future to the left and right, respectively. These two sets are related by the unitary transformation,

$$\begin{pmatrix} \varphi^{\rm out}_{-}(x,k) \\ \varphi^{\rm out}_{+}(x,k) \end{pmatrix} = \begin{pmatrix} -r^{*}_{-}(k) & t^{*}(k) \\ t^{*}(k) & -r^{*}_{+}(k) \end{pmatrix} \begin{pmatrix} \varphi^{\rm in}_{-}(x,k) \\ \varphi^{\rm in}_{+}(x,k) \end{pmatrix}, \tag{D.2}$$

It is easily shown that

$$\varphi^{\rm out}_{\pm}(x,k)=\varphi^{\rm in^{*}}_{\pm}(x,k). \tag{D.3}$$

Using the *in* states, the Green's function is given by

$$G(x,x';k) = A\varphi_-^{\rm in}(x_>,k)\varphi_+^{\rm in}(x_<,k), \tag{D.4}$$

where $x_<$ ($x_>$) is the smaller (larger) of x and x', and A is a constant. This obviously satisfies the boundary conditions Eqs. (4.12). The constant A can be determined so that this function satisfies Eq. (4.11). Substituting this expression into Eq. (4.11), setting $x' = x_+$, and integrate over $[x_+ - 0, x_+ + 0]$,

$$\left(\frac{dG}{dx}\right)_{x_+ + 0} - \left(\frac{dG}{dx}\right)_{x_+ - 0} = 2, \tag{D.5}$$

Thus we obtain

$$A = -\frac{i}{kt(k)}. \tag{D.6}$$

Hence, using the Siegert state expansion of the Green's function, Eq. (D.12), we obtain the scattering states

$$\varphi_-^{\rm in}(x,k) = ike^{+ikx_-}\sum_n \frac{\phi_n(x)\phi_n(x_-)}{k_n(k-k_n)},\ x \geq x_-, \tag{D.7a}$$

$$\varphi_+^{\rm in}(x,k) = ike^{-ikx_+}\sum_n \frac{\phi_n(x)\phi_n(x_+)}{k_n(k-k_n)},\ x \leq x_+. \tag{D.7b}$$

D.1.2 Siegert state expansion of the Green's function

The equation and boundary condition for the Green's function are given by Eq. (4.11) and Eqs. (4.12). Let us expand the Green's function using the Siegert states (SSs)

$$G(x,x';k) = \sum_n \alpha_n \phi_n(x)\phi_n(x'). \tag{D.8}$$

Substituting this into Eqs. (4.12),

$$\left(\frac{d}{dx} \pm ik\right) G(x,x';k)\Big|_{x=x_\mp} = \mp i\sum_n \alpha_n(k_n - k)\phi_n(x_\mp)\phi_n(x') = 0. \tag{D.9}$$

From the sum rule for the SSs Eq. (3.22a), one finds

$$\alpha_n = \frac{1}{k_n(k-k_n)}. \tag{D.10}$$

Then using Eq. (3.22b), it can be shown that

$$\begin{aligned}(E-H)G(x,x';k) &= \sum_n (E-E_n)\frac{\phi_n(x)\phi_n(x')}{k_n(k-k_n)} \\ &= \frac{1}{2}\sum_n \left(1+\frac{k}{k_n}\right)\phi_n(x)\phi_n(x') \\ &= \delta(x-x').\end{aligned} \tag{D.11}$$

Thus we obtain

$$G(x,x';k)=\sum_n \frac{\phi_n(x)\phi_n(x')}{k_n(k-k_n)}. \tag{D.12}$$

D.2 Three-dimensional case

D.2.1 Siegert state expansion of the scattering state

Here we derive the SS expansion of the scattering state . The scattering states satisfy Eq. (3.31a) and the boundary conditions Eq. (3.31d) and

$$\varphi_l(r,k)|_{r\to\infty}=e^{-ikr}-(-1)^l S_l(k)e^{ikr}, \tag{D.13}$$

where $S_l(k)$ is the scattering matrix. Taking Eq. (4.51) into account, in outer region we have

$$\varphi_l(r,k)|_{r\geq a}=e_l(-kr)-(-1)^l S_l(k)e_l(kr), \tag{D.14}$$

where the function $e_l(kr)$ is is the scaled spherical Hankel function of first kind defined by Eq. (C.3a). The Green's function is related to this function,

$$G_l(r,r';k)=\frac{i}{k}\varphi_l(r_<)e_l(kr_>),\ r_>\geq R \tag{D.15}$$

where $r_<(r_>)$ is the smaller (larger) of r and r'. Setting $r'=a$, we find

$$\varphi_l(r,k)=-\frac{ikG_l(r,a;k)}{e_l(ka)},\ 0\leq r\leq R. \tag{D.16}$$

Substituting the spectral resolution of the Green's function Eq. (D.18), we obtain the SS expansion of the scattering state,

$$\varphi_l(r,k)=-ike^{-ika}\frac{(-ika)^l}{\theta_l(-ika)}\sum_{n=1}^{2N+l}\frac{\phi_{ln}(r)\phi_{ln}(a)}{k_{ln}(k_{ln}-k)},\ 0\leq r\leq R, \tag{D.17}$$

where $\theta_l(kr)$ is the reverse Bessel polynomial, see Appendix C.

D.2.2 Siegert state expansion of the Green's function

The spectral representation of the Green's function is given by

$$G_l(r,r';k)=\sum_{n=1}\frac{\phi_{ln}(r)\phi_{ln}(r')}{k_{ln}(k_{ln}-k)},\ (0\leq r,r'\leq R). \tag{D.18}$$

The detailed procedure for its derivation is the same as in Appendix D.1.2.

Appendix E

Some properties of the operator $\hat{\lambda}_t$

E.1 Proof of the identity $(\hat{\lambda}_t - ik)e^{-iEt} = 0$

From the definition of the operator $\hat{\lambda}_t$,

$$\hat{\lambda}_t \delta(t) = \int_{-\infty}^{\infty} ike^{-iEt} \frac{dE}{2\pi}, \tag{E.1}$$

and using the formula

$$\int_0^{\infty} e^{\pm ik^2 t/2} dk = \sqrt{\frac{\pi}{2}} \frac{e^{\pm i\pi/4}}{(t \pm i0)^{1/2}}, \tag{E.2}$$

we obtain

$$\hat{\lambda}_t \delta(t) = \frac{2e^{3i\pi/4}}{\sqrt{2\pi}} \frac{d}{dt} \left[\frac{\theta(t)}{t^{1/2}} \right]. \tag{E.3}$$

Using the identity,

$$f(t) = \int_{-\infty}^{\infty} \delta(t - t') f(t') dt', \tag{E.4}$$

we find

$$\hat{\lambda}_t f(t) = \frac{2e^{3i\pi/4}}{\sqrt{2\pi}} \frac{d}{dt} \int_{-\infty}^{t} \frac{f(t')}{(t - t')^{1/2}} dt'. \tag{E.5}$$

The equation (E.5) indicates that calculating the value of $\hat{\lambda}_t f(t)$ for a given time t requires all the past information of $f(t')$ form $t' = -\infty$ to $t' = t$ with the weight $1/\sqrt{t - t'}$. Thus the operator $\hat{\lambda}_t$ is *non-local* with respect to time. Substituting $f(t) = e^{-iEt}$, setting $s = \sqrt{t - t'}$, and using Eq. (E.2), one finds,

$$(\hat{\lambda}_t - ik)e^{-iEt} = 0. \tag{E.6}$$

E.2 The Green's function of the operator $\hat{\lambda}_t - ik$

To obtain the Green's function for the operator $\hat{\lambda}_t - ik$, we proceed the following steps. First, we proof

$$\hat{\lambda}_t \left[\frac{df(t)}{dt} \right] = \frac{d}{dt} \left[\hat{\lambda}_t f(t) \right], \tag{E.7}$$

where $f(t)$ is a smooth function of t. This is the commutativity between the operator $\hat{\lambda}_t$ and time derivative. Second, we calculate the action of the operator $\hat{\lambda}_t$ on $t^{-1/2}$,

$$\hat{\lambda}_t \left[\frac{e^{-3\pi i/4}\theta(t)}{\sqrt{2\pi t}} \right] = \delta(t), \tag{E.8}$$

where $\theta(t)$ is the step function. Finally, we calculate the action of the operator $\hat{\lambda}_t$ on the Faddeeva function $w(z)$ [88], namely,

$$\hat{\lambda}_t[\theta(t)w(\alpha\sqrt{t})] = \sqrt{2}e^{\pi i/4}\theta(t)\left[\frac{i}{\sqrt{\pi t}} - \alpha w(\alpha\sqrt{t}) \right]. \tag{E.9}$$

Using them, we construct the Green's function for the operator $\hat{\lambda}_t - ik$.

E.2.1 Commutativity between the operator $\hat{\lambda}_t$ and time-derivative

Equation (E.5) is equivalent to

$$f(t) = \frac{e^{-3\pi i/4}}{\sqrt{2\pi}} \int_{-\infty}^{t} \frac{\hat{\lambda}_{t'} f(t')}{(t-t')^{1/2}} dt'. \tag{E.10}$$

This can be proved easily. Multiplying the factor $1/\sqrt{t''-t}$ for both sides, and integrate over $[t', t'']$,

$$\begin{aligned}
\int_{t'}^{t''} \frac{f(t)}{\sqrt{t''-t}} dt &= \frac{e^{-3\pi i/4}}{\sqrt{2\pi}} \int_{t'}^{t''} \frac{dt}{\sqrt{t''-t}} \int_{-\infty}^{t} \frac{\hat{\lambda}_{t'} f(t')}{\sqrt{t-t'}} dt' \\
&= \frac{e^{-3\pi i/4}}{\sqrt{2\pi}} \int_{-\infty}^{t} \hat{\lambda}_{t'} f(t') dt' \int_{t'}^{t''} \frac{dt}{\sqrt{t''-t}\sqrt{t-t'}} \\
&= \frac{e^{-3\pi i/4} B(1/2,1/2)}{\sqrt{2\pi}} \int_{-\infty}^{t} \hat{\lambda}_t f(t') dt',
\end{aligned} \tag{E.11}$$

where $B(x,y)$ is the beta function. We obtain

$$\int_{-\infty}^{t} \hat{\lambda}_{t'} f(t') dt' = \frac{\sqrt{2\pi}e^{3\pi i/4}}{B(1/2,1/2)} \int_{t'}^{t''} \frac{f(t)}{\sqrt{t''-t}} dt. \tag{E.12}$$

Differentiate both hand side by t, taking limit $t' \to -\infty$ and using $B(1/2,1/2) = \pi$, we obtain Eq. (E.5).

Integrating by parts Eq. (E.5), we obtain another form of this equation,

$$\hat{\lambda}_t f(t) = \frac{2e^{3\pi i/4}}{\sqrt{2\pi}} \int_{-\infty}^{t} \frac{df(t')}{dt'} \frac{dt'}{(t-t')^{1/2}}. \tag{E.13}$$

Here it is assumed that the function satisfies $\lim_{t\to-0} f(t)|_{t<0} = 0$. Substituting $\frac{df(t)}{dt}$ into Eq. (E.5), differentiate Eq. (E.13) by t, and compare them, we find

$$\hat{\lambda}_t \left[\frac{df(t)}{dt} \right] = \frac{d}{dt} \left[\hat{\lambda}_t f(t) \right]. \tag{E.14}$$

So $\hat{\lambda}_t$ commutes with the time derivative.

E.2.2 The action of the operator $\hat{\lambda}_t$ on the function $t^{-1/2}$

Acting $\hat{\lambda}_t$ from the left side of Eq. (E.3), and using the property Eq. (E.14), and integrating with respect to t, we obtain

$$\hat{\lambda}_t \left[\frac{e^{-3\pi i/4}\theta(t)}{\sqrt{2\pi t}} \right] = \delta(t). \tag{E.15}$$

E.3 The action of the operator $\hat{\lambda}_t$ on the Faddeva function $w(z)$

The Faddeva function $w(z)$ is defined by

$$\frac{dw(z)}{dz} = -2zw(z) + \frac{2i}{\sqrt{\pi}}, \; w(0) = 1. \tag{E.16}$$

Substituting $w(z) = C(z)e^{-z^2}$, one finds the solution,

$$w(z) = e^{-z^2}\mathrm{erfc}(-iz), \tag{E.17}$$

where $\mathrm{erfc}(z)$ is the complementary error function defined by

$$\mathrm{erfc}(z) = 1 + \frac{2i}{\sqrt{\pi}} \int_0^z e^{t^2} dt. \tag{E.18}$$

Using the formula (See Appendix F),

$$\int_0^t \frac{w(\alpha\sqrt{t'})}{(t-t')^{1/2}} dt' = \frac{i\sqrt{\pi}}{\alpha} \left[1 - w(\alpha\sqrt{t}) \right], \tag{E.19}$$

we find

$$\begin{aligned}
\hat{\lambda}_t[\theta(t)w(\alpha\sqrt{t})] &= \frac{2e^{3\pi i/4}}{\sqrt{2\pi}} \frac{d}{dt} \int_{-\infty}^t \frac{\theta(t')w(\alpha\sqrt{t'})}{(t-t')^{1/2}} dt' \\
&= \frac{2e^{3\pi i/4}}{\sqrt{2\pi}} \frac{d}{dt} \int_0^t \frac{w(\alpha\sqrt{t'})}{(t-t')^{1/2}} dt' \\
&= \sqrt{2}e^{3\pi i/4} \frac{d}{dt} \frac{i}{\alpha} [1 - w(\alpha\sqrt{t})] \\
&= -\sqrt{2}e^{3\pi i/4} \frac{i}{\alpha} \frac{dw(\alpha\sqrt{t})}{dt} \\
&= \sqrt{2}e^{\pi i/4}\theta(t) \left[\frac{i}{\sqrt{\pi t}} - \alpha w(\alpha\sqrt{t}) \right]
\end{aligned} \tag{E.20}$$

E.3.1 The Green's function

Using Eq. (E.15) and Eq. (E.20), we find the Green's function for the operator $\hat{\lambda}_t - ik$ is given by

$$g(t;k) = \theta(t)\left[\frac{e^{-3\pi i/4}}{\sqrt{2\pi t}} - \frac{k}{2}w(-e^{-\pi i/4}k\sqrt{t/2})\right]. \tag{E.21}$$

Appendix F

Proof of the identity Eq. (E.19)

Let us rewtite the definition Eq. (E.16) of the Faddeva function $w(z)$,

$$\frac{dw(\alpha\sqrt{t'})}{dt'} = -\alpha^2 w(\alpha\sqrt{t'}) + \frac{i\alpha}{\sqrt{\pi t'}}. \tag{F.1}$$

Multipling $1/\sqrt{t-t'}$ to the above equation, and integrating by t' over $[0,t]$, one obtains

$$\int_0^t \frac{w(\alpha\sqrt{t'})dt'}{\sqrt{t-t'}} = -\frac{1}{\alpha^2}\int_0^t \frac{dw(\alpha\sqrt{t'})}{dt'}\frac{dt'}{\sqrt{t-t'}} + \frac{i}{\sqrt{\pi}\alpha}\int_0^t \frac{dt'}{\sqrt{t'(t-t')}}. \tag{F.2}$$

The second term of Eq. (F.2) can be evaluated as

$$\begin{aligned}
\frac{i}{\sqrt{\pi}\alpha}\int_0^t \frac{dt'}{\sqrt{t'(t-t')}} &= \frac{i}{\sqrt{\pi}\alpha}\int_0^1 \frac{ds}{\sqrt{s(1-s)}}, \\
&= \frac{i}{\sqrt{\pi}\alpha}B(1/2,1/2), \\
&= i\frac{\sqrt{\pi}}{\alpha},
\end{aligned} \tag{F.3}$$

where $B(x,y)$ is the Beta function. The Faddeva function can be expanded into a series [88],

$$w(\alpha\sqrt{t}) = \sum_{n=0}^{\infty}\frac{(i\alpha\sqrt{t})^n}{\Gamma(n/2+1)}, \tag{F.4}$$

where $\Gamma(z)$ is the Gamma function. Using this, the time derivative is given by

$$\frac{dw(\alpha\sqrt{t})}{dt'} = \sum_{n=1}^{\infty}\frac{(i\alpha)^n}{\Gamma(n/2)}t^{n/2-1}. \tag{F.5}$$

Using this,

$$\begin{aligned}
\int_0^t \frac{dw(\alpha\sqrt{t'})}{dt'}\frac{dt'}{\sqrt{t-t'}} &= \sum_{n=1}^{\infty}\frac{(i\alpha)^n}{\Gamma(n/2)}\int_0^t \frac{(t')^{n/2-1}dt'}{\sqrt{t-t'}}, \\
&= \sum_{n=1}^{\infty}\frac{(i\alpha)^n}{\Gamma(n/2)}t^{n/2-1/2}\int_0^1 s^{n/2-1}(1-s)^{-1/2}ds, \\
&= \sum_{n=1}^{\infty}\frac{(i\alpha)^n}{\Gamma(n/2)}t^{n/2-1/2}B(n/2,1/2).
\end{aligned} \tag{F.6}$$

The Beta function $B(n/2, 1/2)$ is given by [88]

$$B(n/2, 1/2) = \frac{\Gamma(n/2)\Gamma(1/2)}{\Gamma(n/2+1/2)}. \tag{F.7}$$

Using this and $\Gamma(1/2) = \sqrt{\pi}$, Eq. (F.6) becomes

$$\int_0^t \frac{dw(\alpha\sqrt{t'})}{dt'} \frac{dt'}{\sqrt{t-t'}} = \sqrt{\pi} \sum_{n=1}^{\infty} \frac{(i\alpha)^n}{\Gamma(n/2+1/2)} t^{n/2-1/2}. \tag{F.8}$$

Let us define $m = n - 1$, then

$$\begin{aligned} \sqrt{\pi} \sum_{n=1}^{\infty} \frac{(i\alpha)^n}{\Gamma(n/2+1/2)} t^{n/2-1/2} &= \sqrt{\pi} i\alpha \sum_{m=0}^{\infty} \frac{(i\alpha)^m}{\Gamma(m/2+1)} t^{m/2}, \\ &= \sqrt{\pi} i \ \alpha \ w(\alpha\sqrt{t}). \end{aligned} \tag{F.9}$$

Using Eq. (F.6) and (F.9), the intergral Eq. (F.2) becomes

$$\int_0^t \frac{w(\alpha\sqrt{t'})dt'}{\sqrt{t-t'}} = \frac{i\sqrt{\pi}}{\alpha} \left[1 - w(\alpha\sqrt{t})\right]. \tag{F.10}$$

Appendix G

Fourier transform of the classical trajectory

The Newton equation for the free-electron in the laser field is,

$$\frac{d^2x}{dt^2} = -F_0 \sin^2 \frac{\pi t}{T} \cos \omega t, \tag{G.1}$$

where the initial conditions are

$$\left.\frac{dx}{dt}\right|_{t=0} = 0, \ x(0) = 0. \tag{G.2}$$

The solution of above equation is

$$x(t) = \begin{cases} -\frac{F_0}{2}\left[\frac{1-\cos\omega t}{\omega^2} - \frac{1-\cos(\omega+\omega_0)t}{2(\omega+\omega_0)^2} - \frac{1-\cos(\omega-\omega_0)t}{2(\omega-\omega_0)^2}\right] & (0 < t < T), \\ 0 & (\text{other}). \end{cases} \tag{G.3}$$

For $a = n\frac{2\pi}{T}$ $(n = 1, 2, \ldots)$, we have

$$\int_0^T (1 - \cos at) e^{iEt} dt = -2e^{\frac{iEt}{2}} \sin \frac{ET}{2} \frac{a^2}{E^2 - a^2}. \tag{G.4}$$

Using this, the Fourier transform of $x(t)$ is given by

$$\begin{aligned} x(E) &= \int_{-\infty}^{\infty} x(t) e^{iEt} dt \\ &= \int_0^T x(t) e^{iEt} dt \\ &= -F_0 e^{\frac{iEt}{2}} \sin \frac{ET}{2} \frac{\omega_0^2(E^2 + 3\omega^2 - \omega_0^2)}{E(E^2 - \omega^2)\left[(E+\omega)^2 - \omega_0^2\right]\left[(E-\omega)^2 - \omega_0^2\right]} \end{aligned} \tag{G.5}$$

Appendix H

Partial wave expansion of the Siegert states for non-symmetric potential

The Siegert state eigenvalue problem for the non-symmetric atomic potential in the 3D case reads,

$$\left[-\frac{1}{2}\frac{\partial^2}{\partial r^2}+\frac{\hat{\mathbf{l}}^2}{2r^2}+V_0(r,\theta;\alpha)-E(\alpha)\right]\phi(r,\theta;\alpha)=0, \tag{H.1a}$$

$$\phi(r,\theta;\alpha)=\sum_l \phi_l(r;\alpha)\tilde{P}_l(\cos\theta), \tag{H.1b}$$

$$\phi_l(0;\alpha)=0, \quad \phi_l(r;\alpha)|_{r\geq a}\propto e_l(k(\alpha)r), \tag{H.1c}$$

$$E(\alpha)=k(\alpha)^2/2. \tag{H.1d}$$

The νth solution for the above eigenvalue problem will be denoted by

$$k_\nu(\alpha), \quad E_\nu(\alpha), \quad \phi_\nu(r,\theta;\alpha), \quad \text{and} \quad \phi_l^\nu(r;\alpha). \tag{H.2}$$

Let

$$V_0^{(ll')}(r;\alpha)=\int_0^\pi \tilde{P}_l(\cos\theta)V_0(r,\theta;\alpha)\tilde{P}_{l'}(\cos\theta)\,\sin\theta\,d\theta, \tag{H.3a}$$

$$\tag{H.3b}$$

then

$$H_l(r;\alpha)=-\frac{1}{2}\frac{d^2}{dr^2}+\frac{l(l+1)}{2r^2}+V_0^{(ll)}(r;\alpha). \tag{H.3c}$$

The hermitized Hamiltonian $\tilde{H}_l$ is defined by

$$\tilde{H}_l(r;\alpha)=H_l(r;\alpha)+\frac{1}{2}\mathcal{D}(r;a), \tag{H.3d}$$

Let us introduce some notations,

$$\tilde{\phi}_l(r;\alpha) = ik(\alpha)\phi_l(r;\alpha), \tag{H.4a}$$

$$\phi_{lp}(\alpha) = -\frac{z_{lp}\phi_l(a;\alpha)}{ik(\alpha)a + z_{lp}} \quad p = 1,\dots,l. \tag{H.4b}$$

Using them, let us define the new vector of dimension $2+l$,

$$\boldsymbol{\phi}_l(r;\alpha) = \begin{pmatrix} \phi_l(r;\alpha) \\ \tilde{\phi}_l(r;\alpha) \\ \phi_{l1}(\alpha) \\ \dots \\ \phi_{ll}(\alpha) \end{pmatrix}. \tag{H.4c}$$

Let us introduce the new square matrices $\mathbf{\Lambda}_l(r;\alpha)$ of the dimension $(2+l)\times(2+l)$ and

$$\mathbf{\Lambda}_l(r;\alpha) = \begin{pmatrix} 0 & 1 & 0 & 0 & \dots & 0 \\ -2\tilde{H}_l(r;\alpha) & \mathcal{F}(r;a) & \mathcal{F}(r;a)/a & \mathcal{F}(r;a)/a & \dots & \mathcal{F}(r;a)/a \\ -z_{l1}\mathcal{F}^T(r;a)/a & 0 & -z_{l1}/a & 0 & \dots & 0 \\ -z_{l2}\mathcal{F}^T(r;a)/a & 0 & 0 & -z_{l2}/a & \dots & 0 \\ \dots & \dots & \dots & \dots & \dots & \dots \\ -z_{ll}\mathcal{F}^T(r;a)/a & 0 & 0 & 0 & \dots & -z_{ll}/a \end{pmatrix}, \tag{H.5}$$

and $\mathbf{V}_0^{ll'}$ of the dimension $(2+l)\times(2+l')$,

$$\mathbf{V}_0^{(ll')} = \begin{pmatrix} 0 & 0 & \dots & 0 \\ V_0^{(ll')}(r;\alpha) & 0 & \dots & 0 \\ 0 & 0 & \dots & 0 \\ \dots & \dots & \dots & \dots \\ 0 & 0 & \dots & 0 \end{pmatrix}. \tag{H.6}$$

Then the SS eigenvalue problem can be presented in the form

$$\left[\mathbf{\Lambda}_l(r;\alpha) - ik(\alpha)\right]\boldsymbol{\phi}_l(r;\alpha) - 2\sum_{l'\neq l}\mathbf{V}_0^{(ll')}(r;\alpha)\boldsymbol{\phi}_{l'}(r;\alpha) = 0. \tag{H.7}$$

Normalization is implemented in the following manner,

$$\int_0^{\pi} \sin\theta d\theta \int_0^{\infty} \phi^2(r,\theta;\alpha)\, dr = \sum_l \int_0^{\infty} \phi_l^2(r;\alpha)\, dr$$

$$= \sum_l \left(\int_0^a \phi_l^2(r;\alpha)\, dr + \int_a^{\infty} \phi_l^2(r;\alpha)\, dr \right)$$

$$= \sum_l \left(\int_0^a \phi_l^2(r;\alpha)\, dr + i\, \frac{\phi_l^2(a;\alpha)}{2k(\alpha)} \left[1 + \sum_{p=1}^{l} \frac{z_{lp}}{(ik(\alpha)a + z_{lp})^2} \right] \right) = 1. \qquad \text{(H.8)}$$

Appendix I

Line $t(k)$

The time t can be converted into α via the pulse envelope Eq. (5.17). Instead of Eq. (6.5), we consider the equation

$$k_0(\alpha) = k. \tag{I.1}$$

For a certain fixed value of k, we obtain the corresponding value of α. Note that $\alpha = \alpha_c$ for $k = 0$, hence we obtain $t = t_c$. Suppose Eq. (I.1) was solved. Then let us consider the same equation with a small shift Δk form k, namely

$$k_0(\alpha + \Delta\alpha) = k + \Delta k. \tag{I.2}$$

We seek the value of $\Delta\alpha$ for this equation to hold. To this end, let us consider the Siegert eigenvalue problem Eq. (H.7) for $\alpha + \Delta\alpha$. Using Eq. (I.2), we obtain

$$\left[\mathbf{\Lambda}_l(r;\alpha+\Delta\alpha) - i(k+\Delta k)\right]\boldsymbol{\phi}_l(r;\alpha+\Delta\alpha) - 2\sum_{l'\neq l}\mathbf{V}_0^{(ll')}(r;\alpha+\Delta\alpha)\boldsymbol{\phi}_{l'}(r;\alpha+\Delta\alpha) = 0. \tag{I.3}$$

We assume that Δk is sufficiently small, then $\Delta\alpha$ is also very small. Then we approximate $V_0^{(ll')}(r;\alpha)$ by

$$V_0^{(ll')}(r,\theta;\alpha+\Delta\alpha) \approx V_0^{(ll')}(r,\theta;\alpha) + \frac{dV_0^{(ll')}(r,\theta;\alpha)}{d\alpha}\Delta\alpha. \tag{I.4}$$

Therefore we obtain the following eigenvalue problem with respect to $\Delta\alpha$,

$$\begin{aligned} &\left[\mathbf{\Lambda}_l(r;\alpha) - i(k+\Delta k)\right]\boldsymbol{\phi}_l(r;\alpha+\Delta\alpha) - 2\sum_{l'\neq l}\mathbf{V_0}^{(ll')}(r;\alpha)\boldsymbol{\phi}_{l'}(r;\alpha+\Delta\alpha) \\ = \;& 2\Delta\alpha\sum_{l'}\mathbf{W_0}^{(ll')}(r;\alpha)\boldsymbol{\phi}_{l'}(r;\alpha+\Delta\alpha) \end{aligned} \tag{I.5}$$

where the matrix $\mathbf{W}$ of dimension $(2+l)\times(2+l')$ is given by

$$\mathbf{W_0}^{(ll')}(r;\alpha) = \begin{pmatrix} 0 & 0 & \dots & 0 \\ \frac{dV_0^{(ll')}}{d\alpha} & 0 & \dots & 0 \\ 0 & 0 & \dots & 0 \\ \dots & \dots & \dots & \dots \\ 0 & 0 & \dots & 0 \end{pmatrix}. \tag{I.6}$$

After solving Eq. (I.5), we pick up the one closest to 0. Then we replace α by $\alpha+\Delta\alpha$. The mapping between α and t is given by

$$\alpha = \alpha(t) = \alpha_0\left[1-\Delta\cos^2\frac{\pi}{T}\left(t+\frac{T}{2}\right)\right]\sin^2\frac{\pi}{T}\left(t+\frac{T}{2}\right), \tag{I.7}$$

$$\Delta = \frac{n_{\rm oc}^2-4}{n_{\rm oc}^2-1}. \tag{I.8}$$

Here the origin of time is shifted by $T/2$. After some algebra, we obtain

$$t = -i\frac{T}{\pi}\log\left[ic+\sqrt{1-c^2}\right]-\frac{T}{2}, \tag{I.9a}$$

$$c = \sqrt{\frac{q-1}{2q}+\sqrt{\left(\frac{q-1}{2q}\right)^2+\frac{1}{q}\frac{\alpha}{\alpha_0}}}, \tag{I.9b}$$

$$q = \frac{n_{\rm oc}^2-4}{n_{\rm oc}^2-1}. \tag{I.9c}$$

To construct the spectrum of the slow electron Eq. (J.13), we need to find the moment t when the electron is ionized with the positive momentum k. To this end, in finding t, the most appropriate branch is chosen to lie in the second quadrant of the complex t plane.

Appendix J

Spectrum of the slow electron

The exact spectrum is

$$P(E) = \sum_l P_l(E) = \frac{k}{2\pi} \sum_l \left| \frac{1}{ka\ h_l^{(1)}(ka)} \int_{-\infty}^{\infty} \left(\int_0^{\pi} \tilde{P}_l(\cos\theta) \psi(a,\theta,t) \sin\theta d\theta \right) e^{iEt} dt \right|^2 . \tag{J.1}$$

In the adiabatic approximation,

$$\psi(r,\theta,t) = \sum_l a_l(t)\phi_l(r,\theta,t) \approx a_0(t)\phi_0(r,\theta,t), \tag{J.2a}$$

$$a_0(t) \approx \exp\left[-i \int_0^t E(t')dt' \right] \tag{J.2b}$$

Using this and

$$\phi_0(r,\theta,t) = \sum_l \phi_0^{(l)}(a,t)\tilde{P}_l(\cos\theta), \tag{J.3}$$

then Eq. (J.1) becomes

$$P(E) = \frac{k}{2\pi} \sum_l \left| \frac{1}{ka\ h_l^{(1)}(ka)} \int_{-\infty}^{\infty} \phi_0^{(l)}(a;t) e^{iS(t)} dt \right|^2 , \tag{J.4}$$

where $S(t)$ is the action defined by

$$S(t) = Et - \int_0^t E(t')dt'. \tag{J.5}$$

We evaluate Eq. (J.4) using the steepest descent method,

$$\frac{dS}{dt} = E - E(t) = 0 \rightarrow k(t) = k \rightarrow t(k) = k. \tag{J.6}$$

We approximate the function $S(t)$ by

$$S(t) \approx Et(k) - \int_0^{t(k)} E(t')dt' - \frac{1}{2} \left(\frac{dE(t)}{dt} \right)_{t(k)} t^2. \tag{J.7}$$

Substituting this into Eq. (J.4)

$$P(E) = \frac{k}{2\pi} \exp\left[-2\mathrm{Im}S(t(k))\right] \sum_l \left| \frac{\phi_0^{(l)}(a;t)}{kah_l^{(1)}(ka)} \right|^2 \left| \int_{-\infty}^{\infty} \exp\left[-\frac{1}{2} ik\dot{k}(t)t^2 \right] dt \right|^2 \tag{J.8}$$

The integral in the above equation can be evaluated as follows. Changing the variable,

$$t = \frac{\sqrt{2}}{\sqrt{k\dot{k}(t)}} t', \tag{J.9}$$

then

$$\left| \int_{-\infty}^{\infty} \exp\left[-\frac{1}{2} ik\dot{k}(t)t^2 \right] dt \right|^2 = \frac{2}{k|\dot{k}(t)|} \left| \int_{-\frac{\sqrt{2}}{\sqrt{k\dot{k}(t)}}\infty}^{+\frac{\sqrt{2}}{\sqrt{k\dot{k}(t)}}\infty} \exp[-it'^2] dt' \right|^2 \tag{J.10}$$

From the residue theorem,

$$\int_{-\infty}^{\infty} - \int_{-\frac{\sqrt{2}}{\sqrt{k\dot{k}(t)}}\infty}^{+\frac{\sqrt{2}}{\sqrt{k\dot{k}(t)}}\infty} = 0. \tag{J.11}$$

Using the formula for the Fresnel integral [88]

$$\int_{-\frac{\sqrt{2}}{\sqrt{k\dot{k}(t)}}\infty}^{+\frac{\sqrt{2}}{\sqrt{k\dot{k}(t)}}\infty} = \int_{-\infty}^{\infty} = \sqrt{\frac{\pi}{2}} - i\sqrt{\frac{\pi}{2}}. \tag{J.12}$$

Then Eq. (J.8) becomes

$$P(E) = \frac{\exp\left[-2\mathrm{Im}S(t)\right]}{|\dot{k}(t)|} \sum_l \left| \frac{\phi_0^{(l)}(a;t)}{kah_l^{(1)}(ka)} \right|^2 \Bigg|_{t=t(k)}. \tag{J.13}$$

Publications

1. "Two-channel Siegert pseudostate approach to a three-body Coulomb problem: S-wave resonances of Ps^-(N=2,3)",
   Koudai Toyota and Shinichi Watanabe,
   Phys. Rev. A **68**, 062504 (2003).

2. "Siegert pseudostate perturbation theory: One- and two-threshold cases",
   Koudai Toyota, Toru Morishita and Shinichi Watanabe,
   Phys. Rev. A **72**, 062718 (2005).

3. "Siegert-state expansion in the Kramers-Henneberger frame: Interference substructure of above-threshold ionization peaks in the stabilization regime",
   Koudai Toyota, Oleg. I. Tolstikhin, Toru Morishita and Shinichi Watanabe,
   Phys. Rev. A **76**, 043418 (2007).

4. "Interference substructure of above-threshold ionization peaks in the stabilization regime",
   Koudai Toyota, Oleg. I. Tolstikhin, Toru Morishita and Shinichi Watanabe,
   Phys. Rev. A **78**, 033432 (2008).

5. "Photoelectron interference fringes by super intense x-ray laser pulses",
   Koudai Toyota, Oleg. I. Tolstikhin, Toru Morishita, and Shinichi Watanabe,
   J. Phys.: Conf. Ser. **185**, 012050 (2009).

6. "Slow electrons generated by intense high frequency laser pulses",
   Koudai Toyota, Oleg. I. Tolstikhin, Toru Morishita and Shinichi Watanabe,
   Phys. Rev. Lett. **103**, 153003 (2009).

Fellowships

The University of Electro-Communications UEC
The 21st century COE Program
Innovation in Coherent Optical Science

Research assistant of the 21st century COE program,

"Innovation in Coherent Optical Science" at University of Electro-Communications,

April 2006 - March 2010

JSPS 日本学術振興会

Research fellow of the Japan Society for the Promotion of Science (JSPS),

DC2, Mathematical and physical sciences,

April 2007 - March 2009

Financial supports

The University of Electro-Communications UEC
The 21st century COE Program
Innovation in Coherent Optical Science

Grant-in-Aid for young researchers from the 21st century COE program,
"Innovation in Coherent Optical Science" at University of Electro-Communications,

JSPS 日本学術振興会

1. Grant-in-Aid for JSPS fellows,
2. JSPS Bilateral joint program between U.S. and Japan.

Other

Selected as a member of Japanese representatives for the first HOPE meeting.
http://www.hopemeetings.jp/eng/index.html